CHALMERS

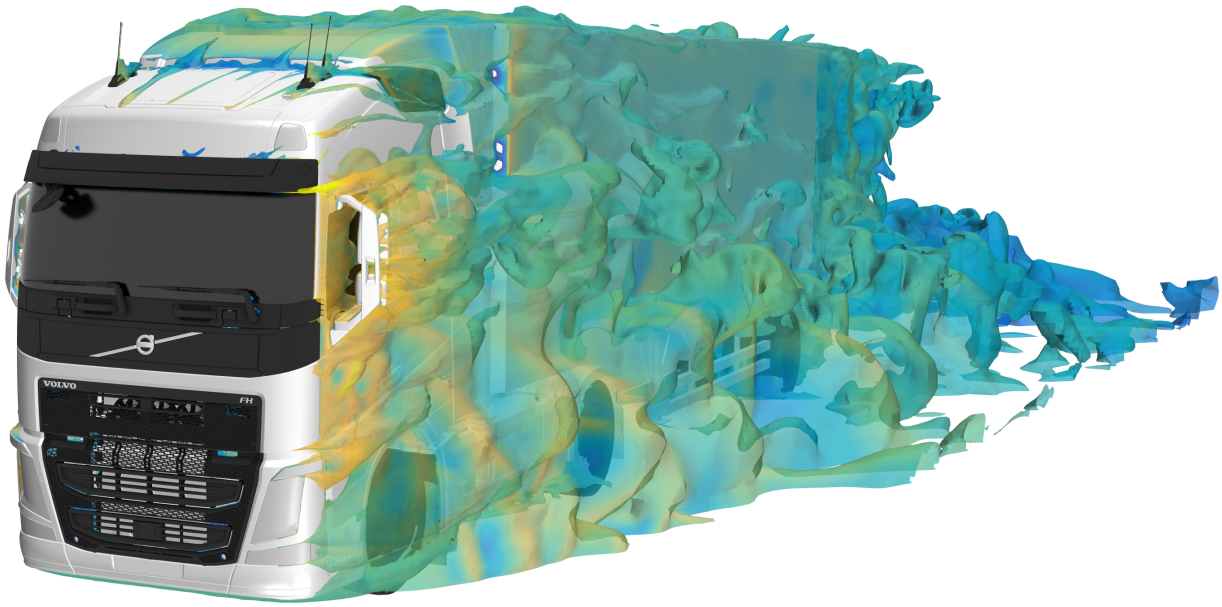

Examination of robustness and accuracy of CFD simulations for external aerodynamics of commercial vehicles

Master's thesis in Applied Mechanics

ERIK JOSEFSSON

Department of Mechanics and Maritime Sciences
CHALMERS UNIVERSITY OF TECHNOLOGY
Göteborg, Sweden 2019

MASTER'S THESIS IN APPLIED MECHANICS

Examination of robustness and accuracy of CFD simulations for external aerodynamics of commercial vehicles

ERIK JOSEFSSON

Department of Mechanics and Maritime Sciences
Division of Vehicle Engineering and Autonomous Systems
CHALMERS UNIVERSITY OF TECHNOLOGY

Göteborg, Sweden 2019

Examination of robustness and accuracy of CFD simulations for external aerodynamics of commercial vehicles
ERIK JOSEFSSON

Master's thesis 2019:12
Department of Mechanics and Maritime Sciences
Division of Vehicle Engineering and Autonomous Systems
Chalmers University of Technology
SE-412 96 Göteborg
Sweden
Telephone: +46 (0)31-772 1000

Cover:
Unsteady isosurfaces of total pressure colored by the velocity magnitude.

Chalmers Reproservice
Göteborg, Sweden 2019

Examination of robustness and accuracy of CFD simulations for external aerodynamics of commercial vehicles
Master's thesis in Applied Mechanics
ERIK JOSEFSSON
Department of Mechanics and Maritime Sciences
Division of Vehicle Engineering and Autonomous Systems
Chalmers University of Technology

Abstract

Commercial vehicles account for approximately 25% of the CO_2 emissions from road vehicles in the EU. In order reduce the emissions levels new emission limits have been proposed. Since the aerodynamic drag is one of the dominating resisting forces acting on a truck at highway speed there is a need to improve the aerodynamic design of trucks. Given the limitations of experimental techniques, such as the large blockage created by trucks in available wind tunnels, numerical methods are often used for analyzing the flow field. However, in order to use numerical methods in the aerodynamic design process it is important to understand the accuracy and limitations of the method.

This thesis investigates different methods for improving the correlation between numerical and experimental data. This is done by focusing on three different aspects. Firstly, different turbulence models are investigated. As a starting point a simplified truck model is used and a large number of different turbulence models are investigated. From this study a number of turbulence models will be identified, which are further evaluated using a fully detailed truck and compared to wind tunnel tests. It was found that the accuracy of the drag prediction is heavily dependent on the yaw angle, regardless which turbulence model is used, where a better correlation is achieved for larger yaw angles. Additionally it was found that the turbulence model greatly influences major flow structures such as the length and recirculation pattern of the trailer base wake. Finally, the benefits of using an IDDES compared to a RANS method will be highlighted. Comparing the yaw weighted average error of the drag prediction the IDDES methods resulted in approximately half the error of the RANS methods.

Secondly, the modelling of the wind tunnel environment is investigated. The sensitivity of the predicted drag coefficient to the converging nozzle geometry, non-uniformity in the velocity distribution and test section turbulence levels are evaluated. It was found that the changes to the converging nozzle or turbulence levels did not alter the predicted drag significantly. Non-uniformity in the velocity field is investigated by adding a swirling component. There it was found that the swirling component acted similarly to an equivalent change of the yaw angle.

A mesh study is performed in order to investigate and improve the level of mesh independence. By identifying regions with large gradients per cell a number of refinements are created and evaluated. The predicted drag was sensitive to refinements in areas such as the trailer base wake as well as in the tractor-trailer gap. However, no significant differences in drag prediction were obtained for refinements to regions such as the underbody and the rear-view mirrors.

Keywords: Commercial vehicles, Aerodynamics, CFD, Turbulence modelling, Wind tunnel correlation

Preface

This thesis, accounting for 60 ECTS, was performed at Volvo Group Truck Technology (GTT) in Göteborg, Sweden and examined by the department of Mechanics and Maritime Sciences at Chalmers University of Technology. The work was performed at the Cab Analysis groups at Volvo GTT during the autumn of 2018 and spring of 2019.

I would like to thank Anton Lundberg (Simulation & Analysis Engineer Aerodynamics) for supervising the project and always being available for questions and discussions, providing a lot of valuable guidance. Furthermore a big thanks to Anders Tenstam (Senior Research Engineer) for sharing his expertise and supporting the project. I would also like to express my gratitude to Mattias Hejdesten (Feature Specialist Aerodynamics & Soiling) for organizing and making the thesis possible. Finally I would like to acknowledge my examiner Prof. Simone Sebben for her support and feedback during the project.

As a final remark I would like to thank all my colleagues, in particular the aerodynamics and CFD group, at Volvo for welcoming me and making my time enjoyable.

Erik Josefsson, Göteborg, 2019

Nomenclature

Abbreviations

CFD	Computational Fluid Dynamics
DDES	Delayed Detached Eddy Simulation
DES	Detached Eddy Simulation
DNS	Direct Numerical Simulation
DSL	Durbin Scale Limiter
EU	European Union
FVM	Finite Volume Method
GTT	(Volvo) Group Truck Technology
IDDES	Improved Delayed Detached Eddy Simulation
LES	Large Eddy Simulation
NRC	National Research Council Canada
OEM	Original Equipment Manufacturer
RANS	Reynolds Averaged Navier-Stokes
RSM	Reynolds Stress Models
SA	Spalart–Allmaras
SST	Shear Stress Transport
WMLES	Wall Modelled Large Eddy Simulation

Definitions

1 drag count	$\Delta C_D = 0.001$

Symbols

δ_{ij}	Kronecker delta	$[-]$
$\hat{\Phi}$	Magnitude of Φ gradient per cell	$[\Phi]$
ν, μ	Viscosity, kinematic and dynamic	$[\mathrm{m^2/s}]$, $[\mathrm{Ns/m^2}]$
ν_t, μ_t	Eddy viscosity, kinematic and dynamic	$[\mathrm{m^2/s}]$, $[\mathrm{Ns/m^2}]$
ω	Specific dissipation rate	$[1/\mathrm{s}]$
$\overline{\Phi}$	Time averaged quantity	$[\Phi]$
Φ_∞	Freestream value of quantity	$[\Phi]$
ρ	Air density	$[\mathrm{kg/m^3}]$
Re	Reynolds number	$[-]$
$\tilde{\Phi}$	Volume averaged quantity	$[\Phi]$
ε	Turbulent dissipation	$[\mathrm{m^2/s^3}]$
A	Vehicle frontal area	$[\mathrm{m^2}]$
a_1	Shear stress limiter of the SST k-ω model	$[-]$
C_D	Drag coefficient	$[-]$
C_p	Pressure coefficient	$[-]$
$C_{D,local}$	Local drag coefficient	$[-]$

$C_{p,tot}$	Total pressure coefficient	$[-]$
k	Turbulent kinetic energy	$[\mathrm{m}^2/\mathrm{s}^2]$
k_{mod}	Modelled turbulent kinetic energy	$[\mathrm{m}^2/\mathrm{s}^2]$
k_{res}	Resolved turbulent kinetic energy	$[\mathrm{m}^2/\mathrm{s}^2]$
v_i	Velocity component in i-direction	$[\mathrm{m/s}]$
y^+	Non-dimensional wall distance	$[-]$

Contents

List of Figures

Chapter 5

Appendix A

List of Tables

1 Introduction

This chapter aims to give an introduction to the thesis. To begin with the importance of aerodynamics of commercial vehicles will be discussed. Later the role of CFD in aerodynamic development will be covered. Finally the purpose, limitations and outline of this thesis will be presented.

1.1 Background

Around 20% of the CO_2 emissions in the European Union (EU) comes from road vehicles. Furthermore, the transport sector is the only major sector within the EU where the emissions are still rising. [1] Commercial vehicles produce approximately 25% of the CO_2 emissions from road vehicles. In order to reduce these emissions the EU has proposed new emission limits. Compared to the emission levels of 2019 a two-step reduction of 15% and 30% is proposed to 2025 and 2030, respectively. [2] These regulations will affect the Original Equipment Manufacturers (OEMs) in a number of different ways. Firstly, the fuel consumption of OEMs internal combustion engine vehicles must be reduced. Secondly, the regulations might accelerate the need for electric vehicles which, in order to achieve longer range, also benefit from lower energy consumption. One effective and relatively low cost way of reducing the energy consumption is to reduce the aerodynamic drag.

1.1.1 The effects of aerodynamics

Aerodynamics is the study of a body in a fluid stream. The aerodynamic properties of the body will affect the forces acting on the body. When considering a vehicle this will affect the total force needed to propel the vehicle, which be written as

$$F = F_A + F_G + F_R + F_D = (1+\varepsilon)\, m\frac{dv}{dt} + mg\sin\alpha + f_R mg\cos\alpha + \frac{C_D \rho A v^2}{2}. \tag{1.1}$$

Here the force has been split into four different forces. The first of these, F_A, is the force needed to accelerate the vehicle. In this expression the mass has been corrected by a factor $1+\varepsilon$ in order to account for inertia of rotating parts. Furthermore there is a gravitational force, F_G, needed to overcome road inclination. The rolling resistance is denoted F_R and is dependent upon the coefficient of friction, f_R. Finally there is the aerodynamic drag force, F_D, which depends on the drag coefficient C_D, air density ρ, vehicle frontal area A and velocity v. Given the total force needed to propel the vehicle the required power can be calculated as $P = Fv$. [3] Assuming zero acceleration ($dv/dt = 0$) and that the road has no inclination ($\alpha = 0$) the total power required to propel the vehicle only consists of rolling resistance and drag, which can easily be compared as in figure 1.1. Here it was assumed that the vehicle mass was $m = 30\,\mathrm{t}$, the rolling resistance $f_r = 0.005$, the drag coefficient $C_D = 0.75$ and the frontal area $A = 10.1\,\mathrm{m}^2$. It can be seen that, for this case, the drag force is dominant for velocities above $65\,\mathrm{km/h}$. This highlights the impact drag has on the total energy consumption and the importance of aerodynamics, especially at high speeds.

1.1.2 Aerodynamic development

There are a number of different ways to test the aerodynamic performance of a vehicle. These include both methods for physical testing, such as on-track or wind tunnel testing, as well as numerical methods, CFD. On-track testing can be considered the most realistic test case, since an actual vehicle is driven in on-road conditions. However, the test engineers have little to no control over the flow conditions, such as flow angles and fluctuations. Moreover, the measurement equipment most likely needs to be carried by the vehicle. Hence factors such as size constraints and vibrations might limit the accuracy of the instruments. Measuring aerodynamic coefficients such as drag can be done by, for example, constant speed tests were the power transmitted to the driven wheels are measured. These measurements are complicated by the fact that some of this power will be used to overcome the rolling resistance of the tires, which needs to be modelled in order to calculate the drag. [4]

Wind tunnel measurements allow for more accurate and repeatable testing, since the test object is stationary and the incoming flow is determined by the wind tunnel. Some of the issues regarding wind tunnel testing are the effects of blockage, how to simulate a moving road and how to mount the vehicle. The last two factors also affect whether rotating wheels can be used or not. Since the cost of both building and operating a wind tunnel

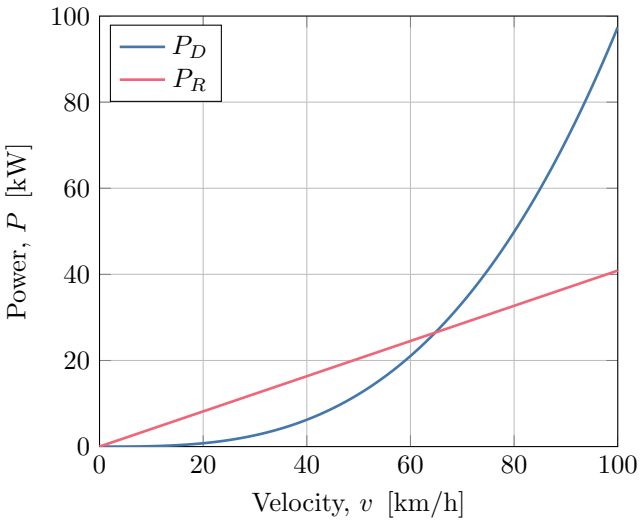

Figure 1.1: Power needed to overcome rolling resistance and drag calculated from equation (1.1).

increases with its size, issues such as high blockage are further complicated when performing full scale tests of commercial vehicles. [4]

In addition to the experimental methods the aerodynamic properties of a vehicle can be investigated using numerical methods. These allow for investigations without a physical prototype being manufactured, potentially decreasing the time and cost of evaluating different geometries. Additionally, numerical methods solves for the complete flow field, allowing the flow to be analyzed in aspects that is not possible using experimental methods. However, there are a number of aspects, such as the computational mesh and the turbulence modelling, that affects the accuracy of the simulations. Hence numerical methods can provide great insights into the flow around a vehicle in a relative short time span. However it is important to understand how the numerical method correlates to physical testing in order to recognize the limitations of the method.

1.2 Purpose

The purpose of this thesis is to investigate modifications to the process used for external aerodynamics at Volvo GTT, with focus on both the robustness and the accuracy. This will be done by investigating the following areas:

Turbulence modelling
A number of different turbulence models will be evaluated in order to understand how it relates to the accuracy of the simulations. This will be done with the aim of developing a more accurate steady-state method, as well as investigating the DES method.

Wind tunnel modelling
The CFD is correlated to wind tunnel test by including the wind tunnel geometry in the simulations. In order to better model the conditions in the wind tunnel boundary conditions such as flow uniformity and turbulent intensity are investigated. Additionally, improvements to the wind tunnel geometry has been investigated.

Mesh study
In order to achieve better accuracy and consistency a mesh study has been performed. Using the standard mesh strategy at Volvo as a baseline, areas of improvement will be identified and different refinements will be evaluated.

1.3 Limitations

The thesis will account for 60 ECTS, therefore limiting the time frame to 40 weeks. All the work has to be performed, evaluated and presented within this time.

The thesis focuses on one truck (internally referenced to as FH-1823), since it has been thoroughly tested in the wind tunnel. However, in the early stages a simplified truck model, demanding less computational power, will be used as a first evaluation. Concepts proving successful with the simplified model will be evaluated for the detailed geometry.

Furthermore the mesh study will focus on achieving mesh independence rather than improving the correlation to the wind tunnel.

1.4 Thesis outline

This thesis is divided into six chapters and one appendix. Since the thesis covers multiple aspects of CFD simulations the different areas have been divided into separate chapters, where additional background and details about the methodology is presented successively for each chapter rather than all at once. To aid the reader the different chapters are described below.

Chapter 1 (Introduction) presents some background about vehicle aerodynamics and highlights how aerodynamics impacts the energy consumption of a commercial vehicle. Additionally some background is given on the different methods used by aerodynamicists, explaining some benefits and drawbacks of CFD. Finally the purpose of the thesis is stated.

Chapter 2 (Theory) gives a brief introduction to the governing equations followed by a more detailed description of the different turbulence models that are used in this thesis. Additionally some aspects of wall modelling as well as wind tunnel effects are discussed.

Chapter 3 (Turbulence modelling - simplified truck) presents the investigation of different turbulence models using a simplified truck geometry.

Chapter 4 (Turbulence modelling - detailed truck) presents and analyses the results of different turbulence models for a detailed truck geometry.

Chapter 5 (Wind tunnel modelling) investigates a number of different aspects related to how the wind tunnel environment is modelled that might improve the correlation between experimental data and CFD.

Chapter 6 (Conclusions) gives a summary to the thesis and states the most important conclusions. Additionally some recommendations for future work is given.

Appendix A (Mesh study) investigates different mesh refinements and their influence on the drag prediction.

2 Theory

The numerical solutions of the flow fields are obtained by solving a set of governing equations. These can be solved using different degrees of modelling. In this chapter these equations and the models used in this thesis will be presented. The chapter will focus on the different turbulence models but will also discuss other aspects, such as wall modelling and wind tunnel effects.

2.1 Governing equations

The motion of a fluid is governed by the Navier-Stokes equations. For an incompressible flow of a Newtonian fluid with constant viscosity the Navier-Stokes equations reads

$$\begin{aligned} \frac{\partial v_i}{\partial x_i} &= 0 \\ \frac{\partial v_i}{\partial t} + \frac{\partial v_i v_j}{\partial x_j} &= -\frac{1}{\rho}\frac{\partial P}{\partial x_i} + \nu \frac{\partial^2 v_i}{\partial x_j \partial x_j}, \end{aligned} \tag{2.1}$$

where v_i is the velocity component in the i direction, x_i is the spatial coordinate direction, ρ is the density, P is the pressure and ν is the kinematic viscosity [5]. Except for some simplified cases, there are no analytical solutions to the Navier-Stokes equations. To solve the equations they are discretized using e.g. the Finite Volume Method (FVM) and solved numerically. [6] Solving the equations without further modifications are called Direct Numerical Simulation (DNS). Because of the need to capture the smallest turbulent length and time scales DNS requires a very fine grid. Moreover, the size of these scales decrease with an increased Reynolds number. Therefore DNS is not affordable for full scale vehicles. [5]

2.2 Turbulence modelling

Since DNS is not affordable for industrial applications the turbulence needs to be modelled. In this section different methods of turbulence modelling will be presented. Firstly some methods using the Reynolds Averaged Navier-Stokes (RANS) equations will be presented. Later some Large Eddy Simulation (LES) methods will be discussed.

2.2.1 RANS methods

A turbulent flow can be described by decomposing an instantaneous quantity, Φ, into a mean, $\overline{\Phi}$, and a fluctuating, Φ', part as $\Phi = \overline{\Phi} + \Phi'$. Inserted into equation (2.1) and time averaged the RANS equations reads

$$\begin{aligned} \frac{\partial \overline{v}_i}{\partial x_i} &= 0 \\ \frac{\partial \overline{v}_i}{\partial t} + \frac{\partial \overline{v}_i \overline{v}_j}{\partial x_j} &= -\frac{1}{\rho}\frac{\partial \overline{P}}{\partial x_i} + \frac{\partial}{\partial x_j}\left(\nu \frac{\partial \overline{v}_i}{\partial x_j} - \overline{v_i' v_j'}\right). \end{aligned} \tag{2.2}$$

RANS methods are often used for obtaining steady state solutions, therefore the first term, containing a time derivative, is often omitted. By examining the equations above it can be seen that there are a total of ten unknowns, the three velocities $\overline{v}_i$, the pressure $\overline{P}$ and the six turbulent stresses $\overline{v_i' v_j'}$. However, there are only four equations. Therefore the turbulent stresses need to be modelled in order to close the system of equations. [5]

The k-ε model

The k-ε model uses the Boussinesq assumption to model the turbulent stresses. The assumption introduces a turbulent viscosity, ν_t, which allows the diffusion term of equation (2.2) to be rewritten as

$$\frac{\partial}{\partial x_j}\left[\nu\left(\frac{\partial \overline{v}_i}{x_j} + \frac{\partial \overline{v}_j}{x_i}\right) - \overline{v_i' v_j'}\right] \quad \rightarrow \quad \frac{\partial}{\partial x_j}\left[(\nu + \nu_t)\left(\frac{\partial \overline{v}_i}{x_j} + \frac{\partial \overline{v}_j}{x_i}\right)\right]. \tag{2.3}$$

In the k-ε model the modelled equations for the turbulent kinetic energy, k, and the dissipation, ε, are solved.

$$\begin{aligned}
\frac{\partial k}{\partial t} + \overline{v}_j \frac{\partial k}{\partial x_j} &= \nu_t \left(\frac{\partial \overline{v}_i}{\partial x_j} + \frac{\partial \overline{v}_j}{\partial x_i} \right) \frac{\partial \overline{v}_i}{\partial x_j} + g_i \beta \frac{\nu_t}{\sigma_\theta} \frac{\partial \overline{\theta}}{\partial x_i} - \varepsilon + \frac{\partial}{\partial x_j} \left[\left(\nu + \frac{\nu_t}{\sigma_k} \right) \frac{\partial k}{\partial x_j} \right] \\
\frac{\partial \varepsilon}{\partial t} + \overline{v}_j \frac{\partial \varepsilon}{\partial x_j} &= \frac{\varepsilon}{k} C_{\varepsilon 1} \nu_t \left(\frac{\partial \overline{v}_i}{\partial x_j} + \frac{\partial \overline{v}_j}{\partial x_i} \right) \frac{\partial \overline{v}_i}{\partial x_j} + C_{\varepsilon 1} g_i \frac{\varepsilon}{k} \frac{\nu_t}{\sigma_\theta} \frac{\partial \overline{\theta}}{\partial x_i} - C_{\varepsilon 2} \frac{\varepsilon^2}{k} + \frac{\partial}{\partial x_j} \left[\left(\nu + \frac{\nu_t}{\sigma_\varepsilon} \right) \frac{\partial \varepsilon}{\partial x_j} \right]
\end{aligned} \tag{2.4}$$

The turbulent viscosity is calculated as

$$\nu_t = C_\mu \frac{k^2}{\varepsilon} \tag{2.5}$$

and the standard values for the constants are $C_\mu = 0.09$, $C_{\varepsilon 1} = 1.44$, $C_{\varepsilon 2} = 1.92$, $\sigma_k = 1$ and $\sigma_\varepsilon = 1.3$. [5]

The SST k-ω model

In the k-ω model, which also is based on the Boussinesq assumption, the transport equation for the specific dissipation, ω, is solved instead of the transport equation for ε. Compared to the k-ε model, the k-ω model better predicts adverse pressure gradient flows. However, one disadvantage is that the k-ω model is dependent on the freestream value of ω. To manage this, the k-ε and k-ω models can be combined into the Shear Stress transport (SST) k-ω model, which uses a k-ω model close to the wall and smoothly switches to a k-ε model further away from the wall. The equations solved are [5]

$$\begin{aligned}
\frac{\partial k}{\partial t} + \frac{\partial}{\partial x_j} \left(\overline{v}_j k \right) &= \frac{\partial}{\partial x_j} \left[\left(\nu + \frac{\nu_t}{\sigma_k} \right) \frac{\partial k}{\partial x_j} \right] + P^k - \beta^* k \omega \\
\frac{\partial \omega}{\partial t} + \frac{\partial}{\partial x_j} \left(\overline{v}_j \omega \right) &= \frac{\partial}{\partial x_j} \left[\left(\nu + \frac{\nu_t}{\sigma_\omega} \right) \frac{\partial \omega}{\partial x_j} \right] + \alpha \frac{P^k}{\nu_t} - \beta \omega^2 + 2 \left(1 - F_1 \right) \sigma_{\omega 2} \frac{1}{\omega} \frac{\partial k}{\partial x_i} \frac{\partial \omega}{\partial x_i} \\
F_1 &= \tanh \left(\xi^4 \right), \quad \xi = \min \left[\max \left(\frac{\sqrt{k}}{\beta^* \omega d}, \frac{500 \nu}{d^2 \omega} \right), \frac{4 \sigma_{\omega_{k-\varepsilon}} k}{C D_\omega d^2} \right] \\
C D_\omega &= \max \left(2 \sigma_{\omega_{k-\varepsilon}} \frac{1}{\omega} \frac{\partial k}{\partial x_i} \frac{\partial \omega}{\partial x_i}, 10^{-10} \right) \\
\nu_t &= \frac{a_1 k}{\max \left(a_1 \omega, |\overline{s}| F_2 \right)} \\
F_2 &= \tanh \left(\eta^2 \right), \quad \eta = \max \left(\frac{2 k^{1/2}}{\beta^* \omega d}, \frac{500 \nu}{d^2 \omega} \right)
\end{aligned} \tag{2.6}$$

The coefficients are blended between the k-ω and k-ε model using F_1 as

$$\Phi = F_1 \Phi_{k-\omega} + \left(1 - F_1 \right) \Phi_{k-\varepsilon} \tag{2.7}$$

and the default coefficients are

$$\begin{aligned}
\beta^* = 0.09, \quad a_1 = 0.31 \\
\alpha_{k-\omega} = 5/9, \quad \beta_{k-\omega} = 3/40, \quad \sigma_{k,k-\omega} = 0.85, \quad \sigma_{\omega,k-\omega} = 0.5 \\
\alpha_{k-\varepsilon} = 0.44, \quad \beta_{k-\varepsilon} = 0.0828, \quad \sigma_{k,k-\varepsilon} = 1, \quad \sigma_{\omega,k-\varepsilon} = 0.856.
\end{aligned} \tag{2.8}$$

The a_1 coefficient, known as the shear stress limiter, limits the turbulent shear stress in the inner part of the boundary layer. It has been shown that this coefficient can have significant impact on the forces predicted on an airfoil. [7] For external vehicle aerodynamics Siemens (vendors of Star-CCM+) recommends $a_1 = 1$ instead of the default $a_1 = 0.31$. [8]

The v2-f model

The $\overline{v^2} - f$ model is based on the k-ε model but, as an attempt to improve the modelling of wall effects, two additional equations are solved. The first additional equation describes the wall-normal stress, $\overline{v^2}$, and

the second equation models the anisotropic wall effects through the elliptic function f. The two additional equations reads

$$\begin{aligned} \frac{\partial \overline{v}_j \overline{v^2}}{\partial x_j} &= \frac{\partial}{\partial x_j}\left[(\nu+\nu_t)\frac{\partial \overline{v^2}}{\partial x_j}\right] + fk - \frac{\overline{v^2}}{k}\varepsilon \\ L^2\frac{\partial^2 f}{\partial x_j \partial x_j} - f &= \frac{C_1 - 1}{T}\left(\frac{\overline{v^2}}{k} - \frac{2}{3}\right) - C_2\frac{P_k}{\varepsilon}. \end{aligned} \tag{2.9}$$

The turbulent length and time scales, L and T, are defined as

$$L = C_L \max\left[\frac{k^{3/2}}{\varepsilon}, C_\eta\left(\frac{\nu^3}{\varepsilon}\right)^{1/4}\right], \quad T = \max\left[\frac{k}{\varepsilon}, C_T\left(\frac{\nu}{\varepsilon}\right)^{1/2}\right]. \tag{2.10}$$

The turbulent viscosity is then calculated as $\nu_t = C_\mu \overline{v^2} T$ and the coefficients are $C_\mu = 0.22$, $C_1 = 1.4$, $C_2 = 0.45$, $C_T = 6$, $C_L = 0.25$ and $C_\eta = 85$. [9]

Reynolds Stress Models

In Reynolds Stress Models (RSM) the Boussinesq assumption is not used. Instead transport equations for the turbulent stresses are derived from the Navier-Stokes equations.

$$\begin{aligned} \frac{\partial \overline{v_i' v_j'}}{\partial t} + \frac{\partial}{\partial x_k}\left(\overline{v}_k \overline{v_i' v_j'}\right) = &- \overline{v_j' v_k'}\frac{\partial \overline{v}_i}{\partial x_k} - \overline{v_i' v_k'}\frac{\partial \overline{v}_j}{\partial x_k} - \frac{\partial}{\partial x_k}\left(\overline{v_i' v_j' v_k'} + \frac{1}{\rho}\delta_{ij}\overline{v_i' p'} + \frac{1}{\rho}\delta_{ik}\overline{v_j' p'} - \nu\frac{\partial \overline{v_i' v_j'}}{\partial x_k}\right) \\ &+ \frac{1}{\rho}\overline{p'\left(\frac{\partial v_i'}{\partial x_j} + \frac{\partial v_j'}{\partial x_i}\right)} - 2\nu\overline{\frac{\partial v_i'}{\partial x_k}\frac{\partial v_j'}{\partial x_k}} \end{aligned} \tag{2.11}$$

Comparing the RSM model to eddy viscosity models the RSM model better replicates effects from for example curvature and acceleration, since the production terms do not need to be modelled. However it has shown to be less numerically stable as well as more expensive in terms of computational power. [10] Finally it should be noted that, despite the fact that the transport equations of the turbulent stresses are used, some terms will still be modelled since new unknown terms appear in the transport equations. For more details on the modelling, see [5].

The Spalart-Allmaras model

The Spalart-Allmaras model uses the Boussinesq assumption. It is a one equation model which solves the transport equation for the quantity $\tilde{\nu}$

$$\frac{\partial \tilde{\nu}}{\partial t} + v_j\frac{\partial \tilde{\nu}}{\partial x_j} = c_{b1}(1 - f_{t2})\tilde{S}\tilde{\nu} - \left(c_{w1}f_w - \frac{c_{b1}}{\kappa^2}f_{t2}\right)\left(\frac{\tilde{\nu}}{d}\right)^2 + \frac{1}{\sigma}\left\{\frac{\partial}{\partial x_j}\left[(\nu+\tilde{\nu})\frac{\partial \tilde{\nu}}{\partial x_j}\right]c_{b2}\frac{\partial \tilde{\nu}}{\partial x_i}\frac{\partial \tilde{\nu}}{\partial x_i}\right\}, \tag{2.12}$$

where

$$\begin{aligned} \nu_t = \tilde{\nu} f_{\nu 1}, \quad f_{\nu 1} = \frac{\chi^3}{\chi^3 + c_{\nu 1}^3}, \quad \chi = \frac{\tilde{\nu}}{\nu} \\ \tilde{S} = S + \frac{\tilde{\nu}}{\kappa^2 d^2}f_{\nu 2}, \quad f_{\nu 2} = 1 - \frac{\chi}{1+\chi f_{\nu 1}}, \quad f_w = g\left(\frac{1+c_{w3}^6}{g^6 + c_{w3}^6}\right)^{1/6} \\ g = r + c_{w2}\left(r^6 - r\right), \quad r = \min\left(\frac{\tilde{\nu}}{\tilde{S}\kappa^2 d^2}, 10\right) \\ f_{t2} = c_{t3}e^{-c_{t4}\chi^2}, \quad S = \sqrt{2\Omega_{ij}\Omega_{ij}}. \end{aligned} \tag{2.13}$$

In this expression d is the wall distance. [11]

When comparing the results obtained from different turbulence models it can be useful to compare the turbulent kinetic energy, k, predicted by the different models. As opposed to for example k-ε and k-ω models the Spalart-Allmaras model does not solve for k. Therefore the approximation

$$k = \frac{\nu_t\sqrt{2S_{ij}S_{ij}}}{\sqrt{C_\mu}} \tag{2.14}$$

is used, where $C_\mu = 0.09$ is the same coefficient as in the k-ε model. [12]

2.2.2 LES methods

Large Eddy Simulation (LES) resolves more of the turbulence than RANS methods by only modelling the smallest turbulent scales. Thereby the large, energy-containing, eddies are resolved. This is done by filtering the Navier-Stokes equations. The quantities are divided into a resolved, $\tilde{\Phi}$, and a modelled, Φ'', part as $\Phi = \tilde{\Phi} + \Phi''$. Inserting the expression into the Navier-Stokes equations and volume averaging results in

$$\begin{aligned} \frac{\partial \tilde{v}_i}{\partial x_i} &= 0 \\ \frac{\partial \tilde{v}_i}{\partial t} + \frac{\partial \tilde{v}_i \tilde{v}_j}{\partial x_j} &= -\frac{1}{\rho}\frac{\partial \tilde{P}}{\partial x_i} + \nu \frac{\partial^2 \tilde{v}_i}{\partial x_j \partial x_j} - \frac{\partial \tau_{ij}}{\partial x_j}. \end{aligned} \tag{2.15}$$

The subgrid stresses, τ_{ij}, are given by

$$\tau_{ij} = \widetilde{v_i v_j} - \tilde{v}_i \tilde{v}_j, \tag{2.16}$$

and needs to be modelled. It is worth noting that the solution is inherently unsteady. Although LES is computationally less expensive than DNS, fine grid requirements near the walls still makes it expensive for high Reynolds numbers. [5]

DES

As an attempt to still model the large turbulent scales, but decreasing the computational cost, LES and RANS can be combined into Detached Eddy Simulation (DES). The boundary layer is modelled using a RANS method while the large eddies, in for example the wake, are resolved with LES. Because of the LES method being unsteady, unsteady RANS is used, which means that the time derivative of equation (2.2) is not omitted. Using for example the SST k-ω model the dissipation term in the k-equation is modified as

$$\beta^* k\omega \rightarrow \beta^* k\omega F_{\text{DES}}, \quad F_{\text{DES}} = \max\left(\frac{L_t}{C_{\text{DES}}\Delta}, 1\right), \quad \Delta = \max\left(\Delta x_1, \Delta x_2, \Delta x_3\right), \quad L_t = \frac{k^{1/2}}{\beta^* \omega} \tag{2.17}$$

where $C_{\text{DES}} = 0.61$. It can be seen that the switch from SST k-ω to LES is dependent on the grid size, Δx_i. Using a mesh that is too fine in the boundary layer there is a risk that the switch to LES would occur to early, which would result in a poorly resolved LES treatment. [5]

DDES

To avoid switching to LES in the boundary layer F_{DES} in equation (2.17) can be modified as

$$F_{\text{DDES}} = \max\left(\frac{L_t}{C_{\text{DES}}\Delta}\left(1 - F_2\right), 1\right), \tag{2.18}$$

where F_2 is taken from the SST k-ω model, see equation (2.6). This approach is called Delayed DES (DDES).

IDDES

Improved Delayed Detached Eddy Simulation (IDDES) modifies the DDES formulation to allow for Wall Modelled Large Eddy Simulation (WMLES). Using the IDDES formulation more of the flow close to the wall can be solved using LES when the grid is sufficiently fine. The IDDES formulation can be used with different near-wall models. Using the SST k-ω model the IDDES model is obtained by replacing ω in the SST k-ω model with $\tilde{\omega}$, defined as

$$\tilde{\omega} = \frac{\sqrt{k}}{l_{\text{HYBRID}}\beta^*}. \tag{2.19}$$

The IDDES length scale is given by

$$l_{\text{HYBRID}} = \tilde{f}_d\left(1 + f_e\right) l_t + \left(1 - \tilde{f}_d\right) C_{\text{DES}} \Delta_{\text{IDDES}}, \tag{2.20}$$

where

$$
\begin{aligned}
l_t &= \frac{\sqrt{k}}{\beta^* \omega} \\
\tilde{f}_d &= \max\left\{\tanh\left[\left(C_{dt} r_{dt}\right)^3\right], f_B\right\} \\
r_{dt} &= \frac{\nu_t}{\kappa^2 d_\omega^2 \sqrt{\frac{\partial v_i}{\partial x_j}\frac{\partial v_i}{\partial x_j}}} \\
f_e &= \max\left[\left(f_{e1} - 1\right), 0\right] \psi f_{e2} \\
f_{e1} &= \begin{cases} 2e^{-11.09\alpha^2} & \alpha \geq 0 \\ 2e^{-9\alpha^2} & \alpha < 0 \end{cases} \\
f_{e2} &= 1 - \max\left\{\tanh\left[\left(C_t^2 r_{dt}\right)^3\right], \tanh\left(C_l^2 r_{dl}\right)^{10}\right\} \\
\alpha &= 0.25 - \frac{d}{\Delta} \\
r_{dl} &= \frac{\nu}{\kappa^2 d_\omega^2 \sqrt{\frac{\partial x_i}{\partial x_j}\frac{\partial x_i}{\partial x_j}}} \\
\Delta_{\text{IDDES}} &= \min\left[\max\left(0.15d, 0.15\Delta, \Delta_{\min}\right), \Delta\right].
\end{aligned}
\tag{2.21}
$$

ψ is introduced as low-Reynolds number correction function. [13]

Using the Spalart-Allmaras near-wall model the IDDES model is obtained by modifying the wall distance d, used in equation (2.12), as [13]

$$
\tilde{d} = \tilde{f}_d\left(1 + f_e\right) d + \left(1 - \tilde{f}_d\right) \psi C_{\text{DES}} \Delta_{\text{IDDES}}. \tag{2.22}
$$

2.2.3 Realizability

In order to avoid non-physical growth of the turbulent quantities realizability constraints can be imposed. Two-equation models, such as k-ε and k-ω, can overpredict the turbulent kinetic energy in stagnation point flows. This thesis will focus on implementing realizability through the Durbin scale limiter, which achieves the realizability by limiting the turbulent time scale. [14] For the standard k-ε model, where the turbulent time scale $T = k/\varepsilon$, this is implemented as

$$
\begin{aligned}
\nu_t &= C_\mu \frac{k^2}{\varepsilon} = C_\mu k T \\
T &= \max\left[\min\left(\frac{k}{\varepsilon}, \frac{C_T}{C_\mu S}\right), \sqrt{\frac{\nu}{\varepsilon}}\right] \\
S &= \left(S_{ij} S_{ij}\right)^{1/2},
\end{aligned}
\tag{2.23}
$$

where C_T is the Durbin scale limiter. The default value of the limiter is $C_T = 0.6$. For the SST k-ω model the Durbin scale limiter is implemented as

$$
\begin{aligned}
\nu_t &= kT \\
T &= \min\left[\frac{1}{\max\left(\omega, \frac{SF_2}{a_1}\right)}, \frac{C_T}{\sqrt{3}S}\right],
\end{aligned}
\tag{2.24}
$$

where F_2 is given by equation (2.6). [13]

2.3 Wall modelling

In order to achieve accurate results from CFD simulations special care has to be taken when modelling the region close to walls. Assuming a no-slip condition at the wall, a relative velocity difference between the

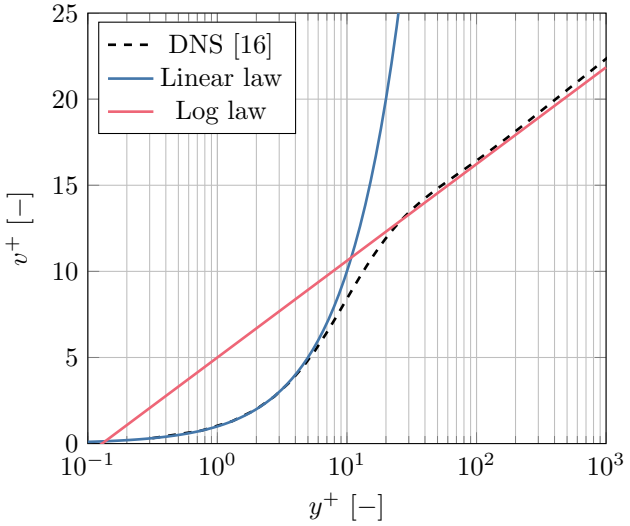

Figure 2.1: Flat plate boundary layer flow. DNS data from [16] compared to the linear and the logarithmic law.

freestream flow and the wall will create a boundary layer. The size of the boundary layer varies with the Reynolds number, Re, defined as

$$\mathrm{Re} = \frac{vl}{\nu}, \tag{2.25}$$

where l is a reference length. The boundary layer is often described in terms of the non-dimensional wall distance, y^+, and the non-dimensional near-wall velocity, v^+, defined as

$$y^+ = \frac{v_\tau y}{\nu}, \quad v^+ = \frac{v}{v_\tau}, \quad v_\tau = \sqrt{\frac{\tau_w}{\rho}}, \tag{2.26}$$

where v_τ is the friction velocity, based on the wall shear stress τ_w. [15]

In figure 2.1 the velocity profile of a boundary layer obtained from DNS simulations is shown. Three main regions can be identified; the viscous region ($y^+ \lesssim 5$), the buffer region ($5 \lesssim y^+ \lesssim 30$) and the log-law region ($30 \lesssim y^+$). In the viscous region the linear law, see equation (2.27), can be used. For $y^+ \gtrsim 30$ the logarithmic law, see equation (2.28), can be used. [15] This is shown in figure 2.1. Since the models does not include $5 \lesssim y^+ \lesssim 30$ the height of the first cell should be chosen such that the y^+ either is below this interval (low y^+ model) or above (high y^+ model). For a low y^+ model the transport equations are solved all the way to the wall. For a high y^+ model wall functions are used for the near-wall region. [13]

$$v^+ = y^+ \tag{2.27}$$

$$v^+ = \frac{\ln y^+}{\kappa} + B \tag{2.28}$$

2.4 Wind tunnel effects

When performing experiments or numerical simulation of a vehicle in a wind tunnel environment there are a number of differences compared to open road that should be kept in mind. Firstly, depending on the wind tunnel and the vehicle, it might not be possible to simulate a moving ground. For open road conditions and no ambient wind the relative velocity between the air and road is zero. However, without a moving ground system in the wind tunnel, there will be a velocity difference between the air and the stationary floor, creating a boundary layer. Furthermore the ground simulation combined with the mounting solution of the vehicle might not allow for rotating wheels. [4]

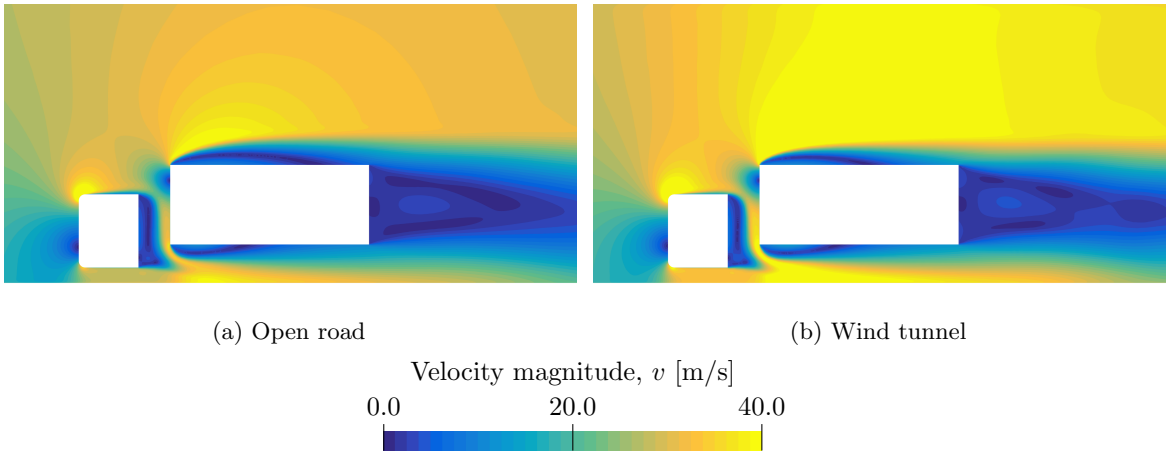

(a) Open road (b) Wind tunnel

Figure 2.2: Velocity magnitude from a 2D simulation of a simplified truck model in open road and wind tunnel conditions.

Additionally the boundaries of the wind tunnel will affect the results, causing a difference to the forces and flow fields obtained in open road conditions. One important effect is the solid blockage. For a closed wall test section the walls will not allow the streamlines to expand. Hence the blockage of the vehicle will force the streamwise velocity to increase in order to fulfill continuity, increasing the measured drag. [17] Furthermore the blockage can affect measurements of other quantities, such as velocities. For tests with large blockage measurements of the velocity using pitot tubes in the beginning of the test section will be affected by distortions in the flow field caused by the blockage. [4] The effect of a large solid blockage is illustrated in figure 2.2 where the velocity magnitude from 2D simulations of a simplified truck model is shown for open road and wind tunnel conditions. It can be seen that the blockage increases the velocity around the truck, most significantly on top of the trailer, and how that in turn alters the wake structures.

3 Turbulence modelling - simplified truck

In order to allow more simulations to be performed when investigating different turbulence models, a simplified truck geometry was initially used. This chapter will present the methodology and results from that study. Based on the results of the study some turbulence models were chosen for further analysis on a detailed truck geometry.

Openly available, often simplified, models of vehicles are commonly used in CFD research. Being standardized there is often extensive amounts of data available in the literature, both numerical and experimental. Two examples of commonly used models are the Ahmed body [18] and the DrivAer model [19]. Both models represents passenger cars, however there is a significant difference in the level of detail. The Ahmed body is block shaped with rounded front corners and a slanted rear. The DrivAer is a detailed model with available features such as mirrors, detailed underbody and engine bay. An example of where these models are used is in a comparison of turbulence models by Ashton et al. [20]. Similarly to this thesis, Ashton et al. first evaluates the models using a simplified geometry (the Ahmed body) and later a detailed model (DrivAer). Despite the Ahmed body being extremely well documented a more truck shaped simplified geometry will be used in this thesis. This is motivated by the fact that it is desired to replicate some truck specific flow features, such as the separation over a cab radius, the flow in the tractor-trailer gap and the massive separation downstream the trailer.

3.1 Method

In this section the methodology used for the investigations of the simplified truck geometry will be presented. In order to simplify the transition from the simplified to the detailed truck the simulation setup was based on the standard CFD process for external aerodynamics at Volvo, which at the start of the thesis was based around Star-CCM+ version 9.06.009.

3.1.1 Geometry

The simplified model consists of two boxes, representing the cab and the trailer, connected with two rods. The model exists in two main configurations, with or without rounded edges on the cab. The geometry is illustrated in figure 3.1 where the different dimensions are presented. For the configurations with the rounded edges a block is added to the front of the cab with square corners, therefore extending the cab $0.08b$. For the investigations in this thesis a value of $b = 2500\,\text{mm}$ was chosen in order to correspond to a full-scale truck. Investigations were made for two different cab-trailer gaps, $g/b = 0.17$ and 0.67. In figure 3.1a the coordinate η is illustrated. This coordinate extends around the cab and will later be used to investigate the surface pressure on the cab. The coordinate is located in the symmetry plane of the simplified truck and is normalized such that η varies between zero and unity.

The simplified truck has been studied previously. Allan [21] performed wind tunnel measurements with varying cab-trailer gap for both the rounded and square model. Furthermore, Östh and Krajnović [22] investigated both models using LES, obtaining drag values similar to the wind tunnel test. Both the experimental and the numerical studies were performed for a scale model with $b = 305\,\text{mm}$. Both of the investigations will be used to evaluate the performance of different turbulence models. Östh and Krajnović calculated C_D using b^2 as the frontal area. In this thesis the actual frontal area $1.2668b^2$, which for $b = 2500\,\text{mm}$ is $7.9175\,\text{m}^2$, has been used. Hence, the drag values from the LES study have been adjusted.

When performing simulations on the simplified truck the computational domain was chosen as in the LES case, which in turn was chosen to imitate the wind tunnel setup. The domain measured $32.7b \times 6.9b \times 5.6b$ (length×width×height) and the truck was placed a distance corresponding to $8b$ from the inlet. The inlet velocity was set to $90\,\text{km/h}$ and the outlet pressure to $0\,\text{Pa}$. Additionally, the ground, sides and top of the tunnel were set as no-slip walls, with the ground having a velocity in the x-direction with the same magnitude as the freestream.

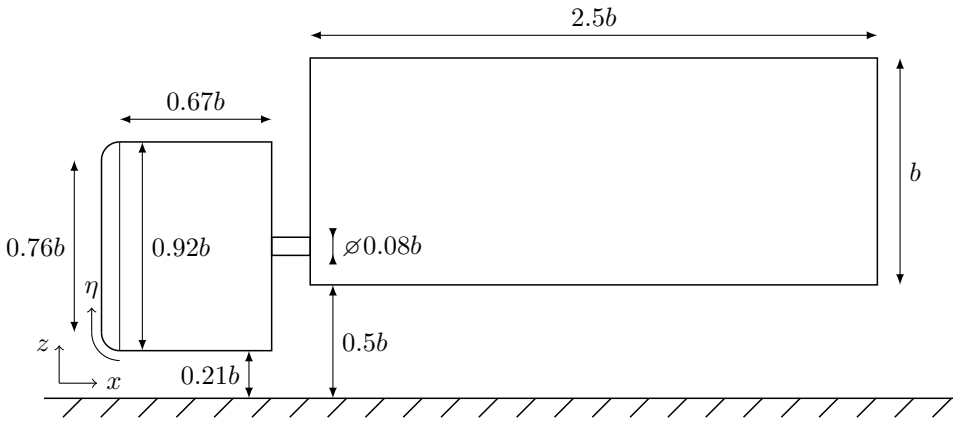

(a) Side view

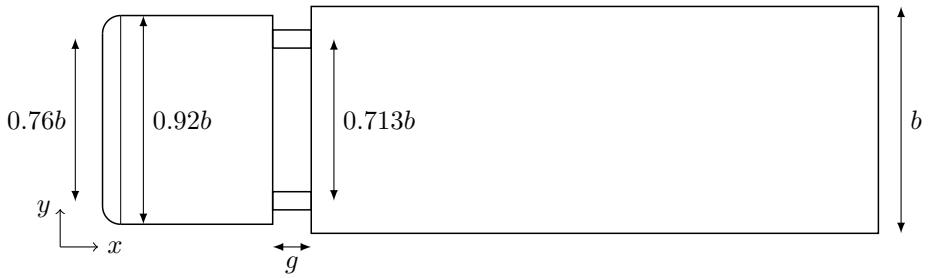

(b) Top view

Figure 3.1: Simplified truck with measurements.

3.1.2 Turbulence models

In total 13 different turbulence models, eleven RANS and two IDDES models, were evaluated. These are presented in table 3.1. A majority of the RANS models were different implementations of either k-ε or SST k-ω models. These variation were largely based on the recommended best practices given by Siemens (vendors of Star-CCM+). The best practice recommends using either the standard k-ε model with a Durbin scale limiter of 1.2 or the SST k-ω model, also with a Durbin scale limiter of 1.2, and the parameter $a_1 = 1$, see equation (2.6). [8] Note that the realizable k-ε model differs from the standard k-ε model with a Durbin scale limiter. Using the Durbin scale limiter the turbulent time scale is limited, whereas the realizable k-ε model alters the equation for the turbulent dissipation, ε, and calculates the constant C_μ as a function of the mean flow and turbulent properties. [13] In addition to these models some alternatives to the two-equations models were included. These were the $\overline{v^2}$-f model, the Reynolds Stress Model and the Spalart-Allmaras model. Finally two different IDDES models were included, with the difference being the model used in the near-wall region.

The simulations were run using a segregated solver and the RANS simulations were run for either 10000 iterations or until the drag coefficient, C_D, varied less than 0.5 counts over the last 1000 iterations. The unsteady simulations used a time step of 1 ms, 10 inner iterations and were run for 10 s. A steady-state standard k-ε simulation, run for 1000 iterations, was used as the initial solution.

3.1.3 Mesh

The simulations were performed using the same meshing approach as for the simulations of detailed trucks using the Volvo Trucks standardized CFD process. Hence the geometry was wrapped (even though the geometry was already valid for meshing), surface meshed and volume meshed. The volume mesh was refined in the wake and around the corners of the leading edge of the cab. Sections of the mesh in the planes $y = 0.0$ m and $z = 1.5$ m are shown in figure 3.2. In order to examine the mesh dependency ten simulations with varying mesh base size were performed for the model with square cab edges and small trailer gap. The base size was varied from 40 mm to 13 mm, resulting in meshes ranging from 7.7 to 156 million cells. These simulations were performed

Table 3.1: Turbulence models evaluated for the simplified truck.

Turbulence model	Implementation	Denotation
k-ε	Realizable	Real. k-ε
	Standard	Standard k-ε
	Standard with Durbin scale limiter of 1.2	DSL = 1.2 k-ε
	Standard with Durbin scale limiter of 0.6	DSL= 0.6 k-ε
SST k-ω	Standard	k-ω
	Durbin scale limiter of 1.2 and $a_1 = 1$	DSL = 1.2 $a_1 = 1$ k-ω
	Durbin scale limiter of 1.2	DSL = 1.2 k-ω
	$a_1 = 1$	$a_1 = 1$ k-ω
$\overline{v^2}$-f	Standard	$\overline{v^2}$-f
Reynolds Stress Models	Standard	RSM
Spalart-Allmaras	Standard	SA
IDDES	SST k-ω in near-wall region	SST IDDES
	Spalart-Allmaras in near-wall region	SA IDDES

using the realizable k-ε model. In figure 3.3 the C_D values are shown for different numbers of cells. It can be seen that most of the meshes contained around 20 to 50 million cells, with the notable exception of the 156 million cell mesh. When increasing the number of cells the C_D initially decreases, until reaching approximately 20 million cells. Between 20 and 40 million cells there are variations of approximately 3 drag counts and the error compared to the finest mesh are between 0.3% and 0.8%. Therefore the finest mesh in this group (marked in red in figure 3.3), consisting of 36 million cells, was considered converged.

3.1.4 Post-processing

The results presented in the section below, such as force coefficients and fields, have been averaged. For the RANS simulations the forces and fields were averaged over the last 1000 iterations. For the unsteady IDDES simulations the averaging was started after 2 s, hence collecting 8 s of averaged data. The fields will be presented using the symmetry plane $y = 0.0$ m and the plane $z = 1.5$ m, located at approximately half the height of the cab. The planes are illustrated in figure 3.4.

3.2 Results

The results of the different turbulence models will in this work focus on the drag prediction of the models. However, in order to better understand the predicted drag, quantities such as pressure and total pressure will also be investigated.

3.2.1 Overview of drag prediction

In this section an overview of the drag prediction of the different models will be given. This will firstly be done by investigating the absolute prediction of the drag coefficient. Afterwards, the prediction of configuration deltas will be investigated.

The resulting drag coefficients are presented in table 3.2 and figure 3.5, where they are compared to wind tunnel measurements and LES simulations. In figure 3.5a the drag coefficient is illustrated for the square and the round geometry with the small trailer gap. Firstly, it can be seen that the best agreement to wind tunnel data is obtained for the LES, where C_D is overpredicted by 0.3% and 3% for the square and round models, respectively. However, for the square model, the IDDES models performs similar to the LES. Both the SST IDDES and the SA IDDES models results in a 1% underprediction of C_D. The experimental agreement of the IDDES models are worse for the rounded cab. For the RANS models the best correlation for the square model is obtained with the standard k-ε model, followed by DSL = 1.2 k-ε, DSL = 1.2 $a_1 = 1$ k-ω and Spalart-Allmaras, which all performs equally. For the rounded cab the DSL = 1.2 k-ε and Spalart-Allmaras perform best, underestimating C_D by 1% and 2%, respectively. As a final remark for the C_D prediction of the small trailer gap it can be seen

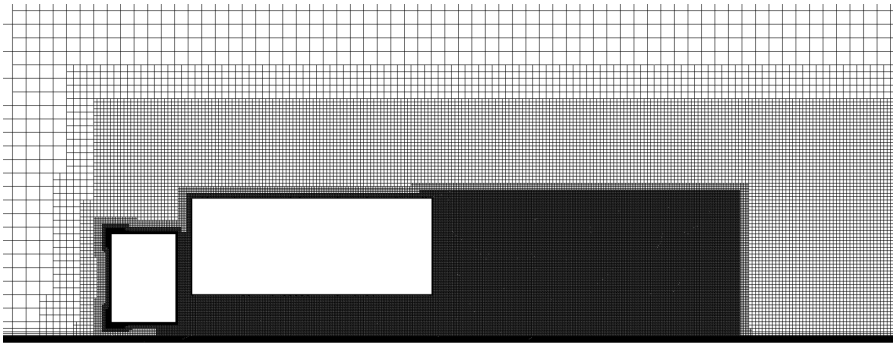

(a) $y = 0.0\,\mathrm{m}$

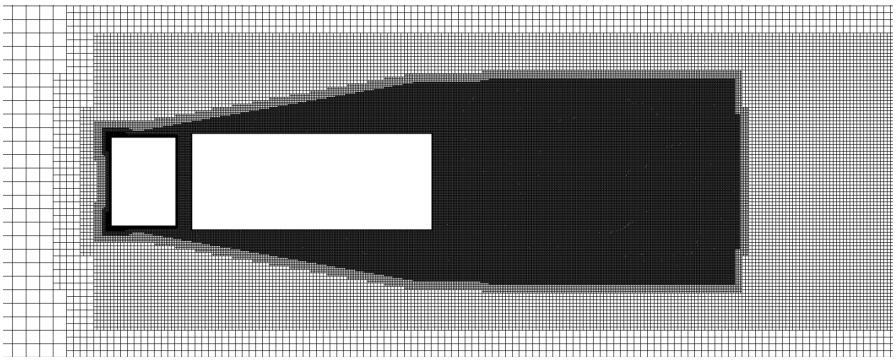

(b) $z = 1.5\,\mathrm{m}$

Figure 3.2: Mesh for simulations of the simplified truck with square corners and small cab-trailer gap.

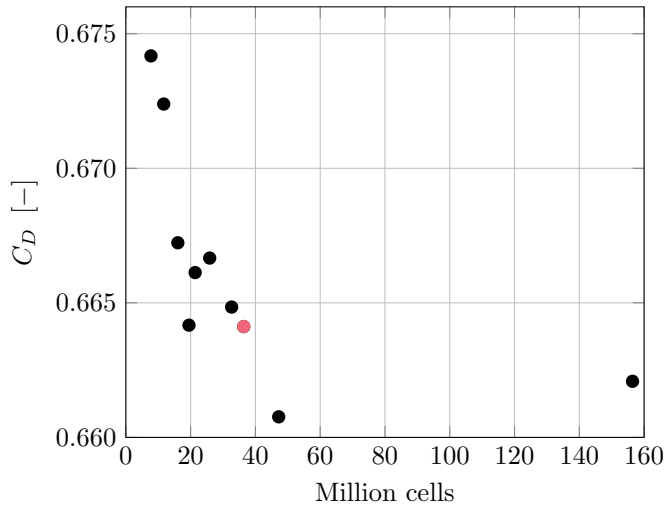

Figure 3.3: Mesh dependence of C_D for simplified truck with the final mesh marked in red.

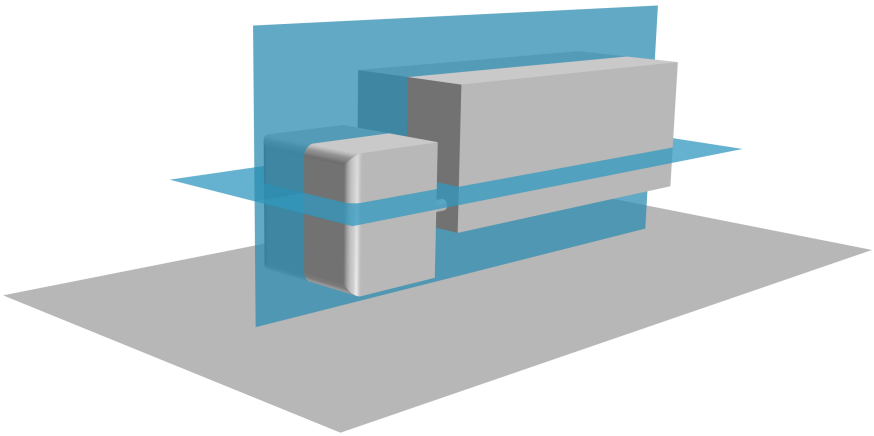

Figure 3.4: Planes $y = 0.0\,\text{m}$ and $z = 1.5\,\text{m}$ used to illustrate the results.

Table 3.2: Drag coefficient of the simplified truck for different turbulence models compared to wind tunnel data and LES simulations.

Turbulence model	Small gap		Large gap	
	Square	Rounded	Square	Rounded
Exp. [21]	0.805	0.608	0.860	1.010
LES [22]	0.808	0.626	0.916	0.887
Real. k-ε	0.664	0.696	0.645	0.957
DSL $= 1.2$ k-ε	0.712	0.600	0.707	1.079
Standard k-ε	0.787	0.681	0.798	0.865
DSL$= 0.6$ k-ε	0.633	0.582	0.605	1.034
k-ω	0.653	0.581	0.637	0.998
DSL $= 1.2$ $a_1 = 1$ k-ω	0.695	0.695	0.714	1.077
DSL $= 1.2$ k-ω	0.678	0.574	0.683	0.979
$a_1 = 1$ k-ω	0.659	0.562	0.635	0.988
$\overline{v^2}$-f	0.626	0.545	0.598	1.049
RSM	0.645	0.631	0.616	1.043
SA	0.705	0.597	0.732	0.968
SST IDDES	0.796	0.561	0.842	1.019
SA IDDES	0.797	0.568	0.853	1.025

that the DSL $= 1.2$ $a_1 = 1$ k-ω results in the same drag coefficient for both the square and rounded cab, which might prove problematic when predicting configuration differences.

In figure 3.5b the drag coefficients of the simplified truck with large trailer gap are presented and compared to experimental and LES data. Similarly to the results for the small trailer gap, there is a good agreement between the wind tunnel and the IDDES models. When comparing the IDDES, LES and wind tunnel data it can actually be seen that the IDDES better correlates to the wind tunnel than the LES. As for the IDDES simulations of the small trailer gap there is no major difference between the SST IDDES and the SA IDDES. Examining the results of the RANS models for the square cab the best agreement is obtained for the standard k-ε model, similarly to the small trailer gap. Just as for the small trailer gap the DSL $= 1.2$ k-ε, DSL $= 1.2$ $a_1 = 1$ k-ω and Spalart-Allmaras all perform similarly and, excluding the standard k-ε, gives the best correlation to the wind tunnel. The drag coefficient of the rounded cab was best predicted by the standard k-ω method. However, it is worth noting that many of the models achieved a good prediction for this geometry.

The predictions of ΔC_D between geometrical configurations are presented in figure 3.6. In figure 3.6a the prediction of ΔC_D between the square and the rounded front is shown for both the small and the large trailer gap. It can be seen that both IDDES models predicts a difference similar to the wind tunnel. In the case of the

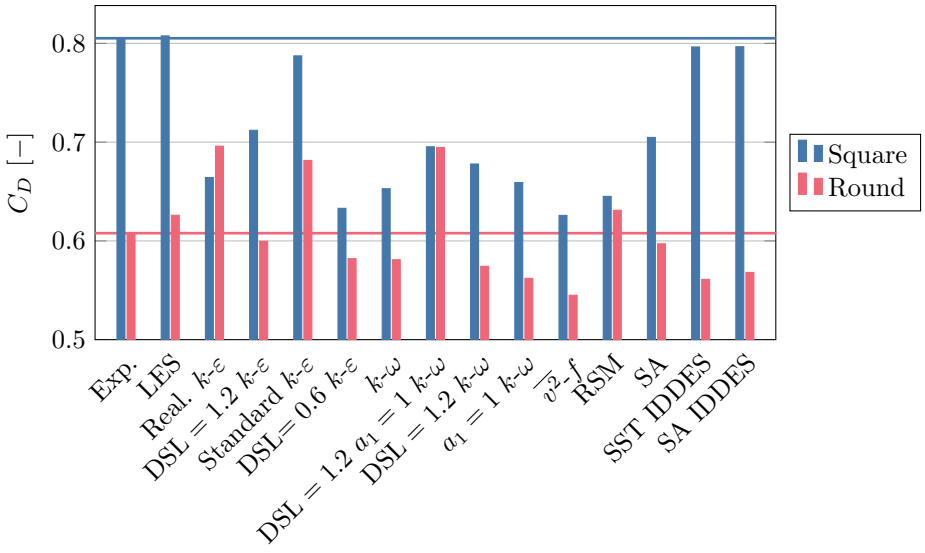

(a) Small gap, $g/b = 0.17$

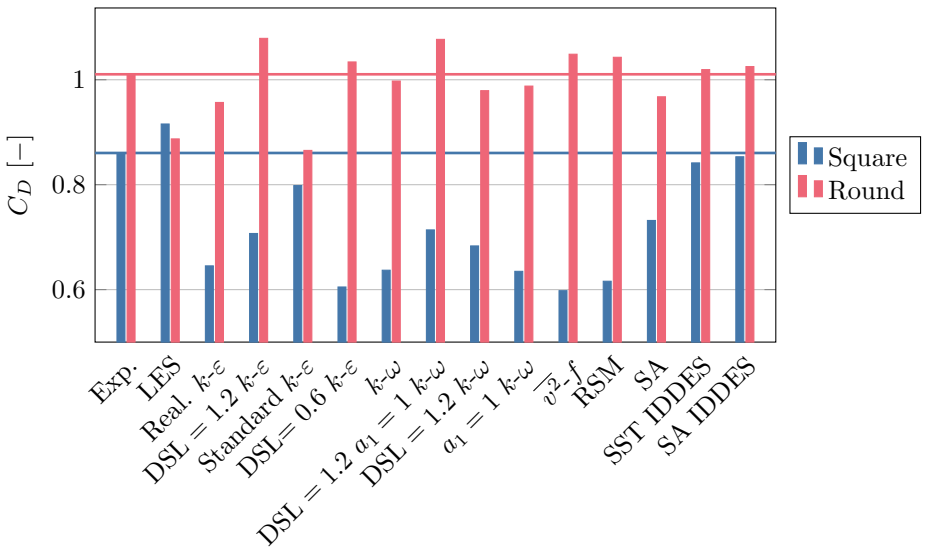

(b) Large gap, $g/b = 0.67$

Figure 3.5: Drag coefficient of the simplified truck for different turbulence models.

Table 3.3: Drag coefficient of the simplified truck for the IDDES models normalized to wind tunnel data, as well as the average error.

Turbulence model	Small gap		Large gap		Average error [%]
	Square	Rounded	Square	Rounded	
LES [22]	1.003	1.030	1.064	0.878	5.5
SST IDDES	0.989	0.923	0.978	1.009	3.0
SA IDDES	0.989	0.935	0.992	1.015	2.5

large trailer gap it can also be seen that the IDDES methods predict the difference significantly better than the LES. This can be explained by the fact that the LES failed to accurately predict the drag of the rounded cab with large trailer gap. For the RANS models the magnitude of ΔC_D is generally underpredicted for the small trailer gap and overpredicted for the large trailer gap. From the investigation of absolute drag prediction it was found that the RANS models, for the small trailer gap, generally underpredicted the drag. Furthermore the underprediction was larger for the square than for the round cab, explaining the underprediction of ΔC_D. For the large trailer gap the RANS models underpredicted the drag for the square cab. For the rounded cab the models both over- and underpredicted the drag, however the errors were generally smaller than the underpredictions for the square cab, resulting in the ΔC_D being overpredicted.

Figure 3.6b illustrates the prediction of ΔC_D between the small and the large trailer gap for both the square and the rounded cab. Similarly to the difference between the square and rounded cab both IDDES models accurately predict the difference, with the square model being the most accurate. Moreover, most RANS models fail to predict the difference between the two trailer gaps of the square model. The difference of the rounded model is better predicted, especially by the k-ω, Reynolds Stress and Spalart-Allmaras models.

3.2.2 IDDES models

Two IDDES models with different near-wall models were tested. Table 3.3 shows the drag predicted by the IDDES models normalized to wind tunnel data for the four different geometries. The table also presents the drag obtained by LES. Additionally the normalized error, averaged over the different geometries, is shown for each model. This error was calculated using the absolute values of the normalized error, i.e.

$$\frac{1}{N}\sum^{N}\left|1-\frac{C_{D,\mathrm{CFD}}}{C_{D,\mathrm{WT}}}\right|. \tag{3.1}$$

It can be seen that the LES gives the most accurate drag prediction for the models with small trailer gap. However, for the large trailer gap better correlation is obtained for the IDDES models, especially for the cab with rounded edges. Comparing the two IDDES models, slightly better results are obtained using the Spalart-Allmaras model in the near-wall region. In addition to resulting in a slightly better drag prediction the SA IDDES model is slightly less computationally expensive, requiring approximately 90% of the core hours used by the SST IDDES model.

In figure 3.7 the pressure coefficient, C_p, is shown along the centerline of the cab using the coordinate η (see figure 3.1a) for all four geometries. η is defined such that $\eta \lesssim 0.3$ at the cab front, $0.3 \lesssim \eta < 0.5$ at the top, $0.5 < \eta \lesssim 0.8$ at the rear and $\eta \gtrsim 0.8$ at the bottom. The dashed vertical dividers illustrate the edges. Comparing the results from the two IDDES models it can be seen that very similar results are obtained for all four geometries.

Investigating the pressures for the square cab with small trailer gap (figure 3.7a) there is a good agreement between IDDES and LES at the front surface of the cab. For the top surface both IDDES models predicts an almost constant pressure, which is not the case for the LES. At the rear surface the IDDES and LES differs for the upper half, but shows good agreement for the lower half. Along the bottom part similar pressures are obtained for the rear half. For the front half of the bottom surface the pressures differ between IDDES and LES, indicating a difference in the separation. For the model with rounded cab and small trailer gap (figure 3.7b) a good agreement can, once again, be seen for the front face. However it is noted that the IDDES models predict significantly lower pressures along the curved edges, indicating a larger acceleration around the corners,

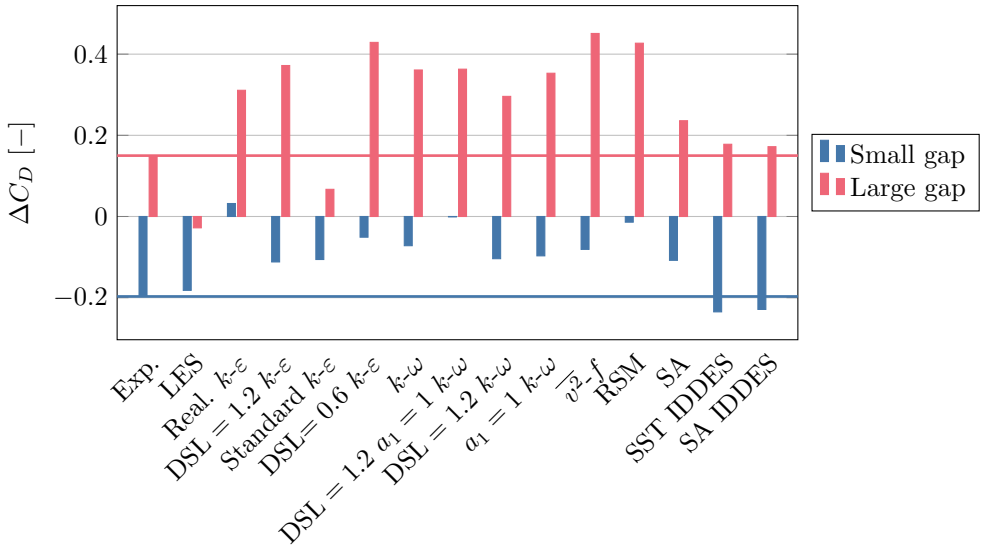

(a) Difference between square and rounded cab.

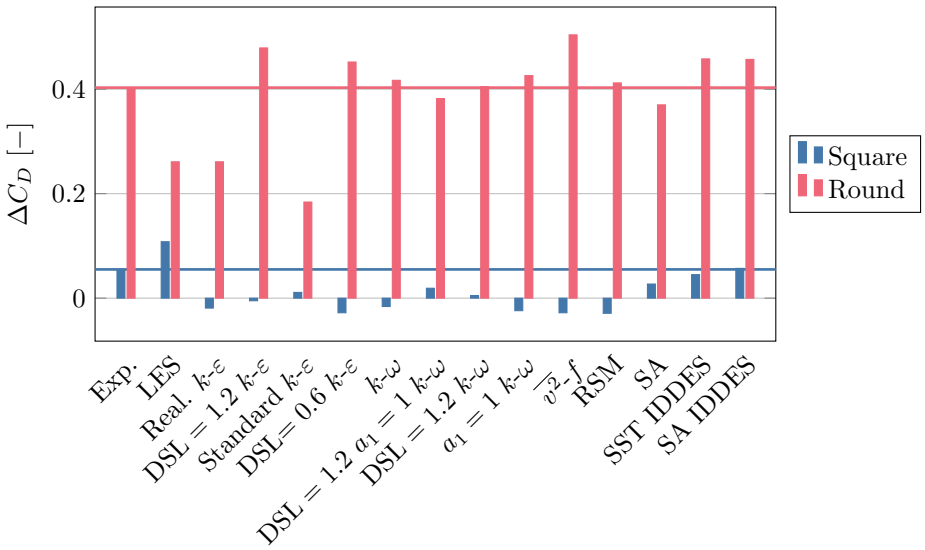

(b) Difference between small and large trailer gap.

Figure 3.6: Prediction of configuration differences in drag coefficient of the simplified truck for different turbulence models.

Table 3.4: Drag coefficient of the simplified truck for different k-ε models normalized to wind tunnel data, as well as the average error.

Turbulence model	Small gap		Large gap		Average error [%]
	Square	Rounded	Square	Rounded	
LES [22]	1.003	1.030	1.064	0.878	5.5
SA IDDES	0.989	0.935	0.992	1.015	2.5
Real. k-ε	0.825	1.145	0.750	0.947	15.6
DSL = 1.2 k-ε	0.884	0.987	0.822	1.068	9.4
Standard k-ε	0.978	1.121	0.928	0.856	9.0
DSL= 0.6 k-ε	0.786	0.958	0.703	1.023	14.4

which might result in significant differences in the separation. This difference remains until the rear half of the top surface, where pressures similar to the LES are obtained. At the rear surface the IDDES models predict a slightly larger pressure than the LES. For the bottom surface it can, once again, be seen that the IDDES predicts a lower pressure at the rounded corners.

For the geometries with large trailer gap it should be noted that the drag prediction of the IDDES models were more accurate than the predictions from LES. Therefore, it might be the case that the pressure curves obtained from IDDES are the most accurate. The square cab with the large trailer gap (figure 3.7c) shows similar results for IDDES and LES along large parts of the cab. The most significant differences can be seen at the front part of the bottom surface. The rounded cab with large trailer gap (figure 3.7d) is the geometry were the most significant differences in pressure between IDDES and LES can be seen. This corresponds to it being the geometry were there also is the largest difference in drag prediction between the models, with IDDES resulting in an underestimation of approximately 1%, compared to LES underestimating the drag by 12%, compared to wind tunnel data. Similar to the rounded cab with small trailer gap it can be seen that a lower pressure is predicted by the IDDES around the rounded edges, especially for the upper edge.

The pressure at the top surface of the cab indicates whether the flow separates or not. Comparing the pressures of the square cab with small and large trailer gap it can be seen that the pressure distribution around the cab is similar for both trailer gaps. However, for the rounded cab there are major differences in the pressure distribution for the two trailer gaps. These results suggest that the rounded cab is more influenced by an increased trailer gap than the square cab, which was confirmed when comparing the difference in drag between the models. When increasing the trailer gap C_D increases 55 counts for the square model and 402 counts for the round model. In figure 3.8 the total pressure coefficient, $C_{p,tot}$, predicted by the SA IDDES model is shown in the symmetry plane $y = 0.0\,\text{m}$ for the four different geometries. As suggested by the pressure distribution the separation above the cab is similar for both trailer gaps of the square cab (figure 3.8a and 3.8c). Similarly to the square cabs the rounded cab with small trailer gap results in a separated region above the cab. However, for the rounded cab the energy losses in this region are smaller than for the square cab. For the rounded cab with large trailer gap almost no separation is obtained above the cab, resulting in larger separation at the leading surface of the trailer.

3.2.3 k-ε models

In total four different k-ε models were investigated, with the difference being the realizability constraints. Table 3.4 shows the drag coefficient predicted by the different k-ε models, LES and SA IDDES normalized to wind tunnel data. The SA IDDES model is included since the IDDES models better predicted the drag for the trucks with the large trailer gap, compared to the LES. Additionally the averaged, normalized, error defined according to equation (3.1) is shown. It is noted that both the DSL = 1.2 and the standard k-ε models results in an error of approximately 9% and that the realizable and the DSL= 0.6 k-ε models gives an error of around 15%. Furthermore, all models except the standard k-ε predicts the rounded cab better than the square cab.

In figure 3.9 the pressure coefficient around the centerline of the cab for the different k-ε models is shown and compared to LES and SA IDDES. For the square cab with small trailer gap (figure 3.9a), where the LES results are believed to be the most accurate, the k-ε models predicts a larger stagnation pressure than the LES, similarly to SA IDDES. The largest overprediction is obtained for the standard k-ε model. At the top

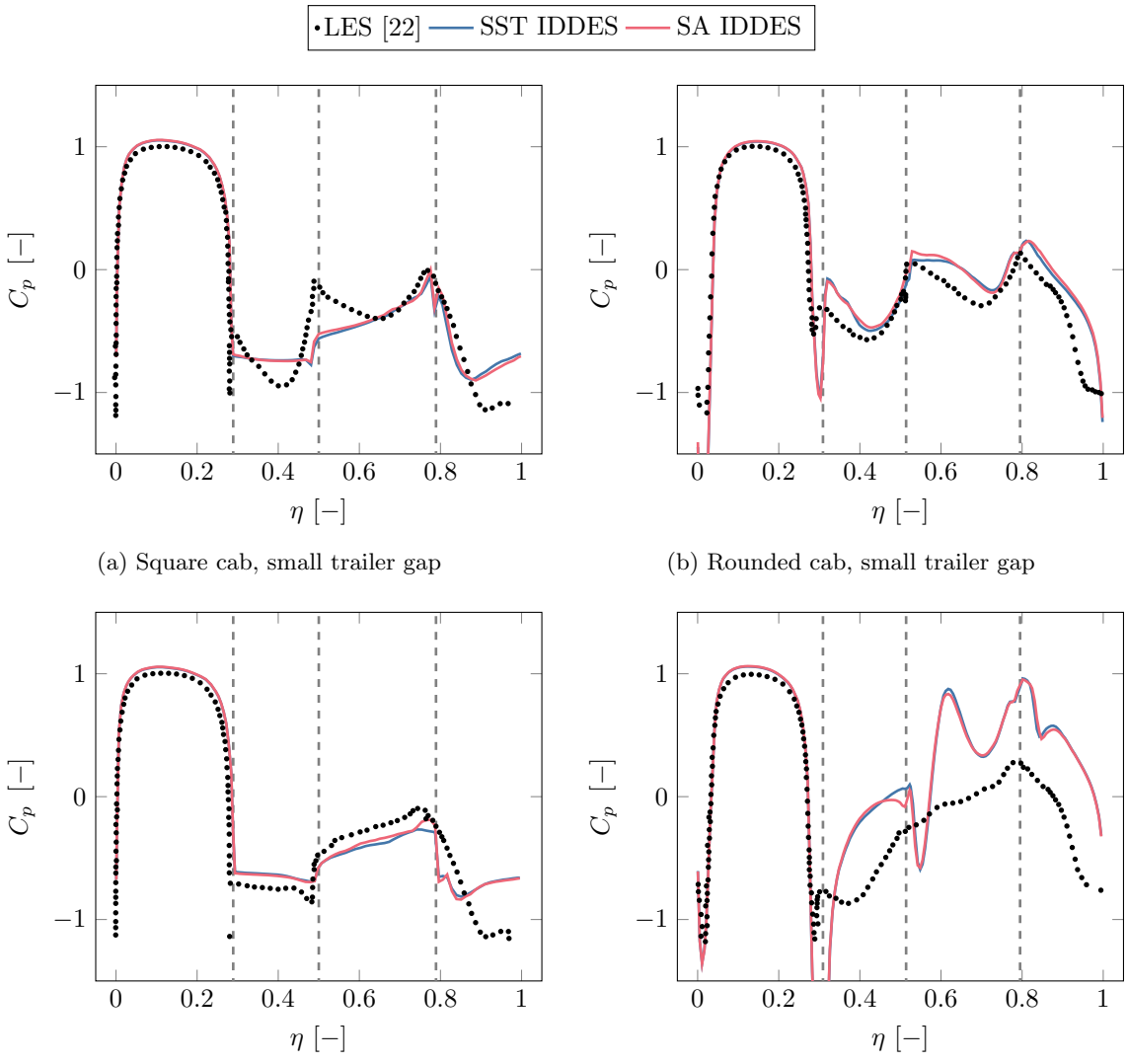

(a) Square cab, small trailer gap

(b) Rounded cab, small trailer gap

(c) Square cab, large trailer gap

(d) Rounded cab, large trailer gap

Figure 3.7: Pressure coefficient around the centerline of the cab of the simplified truck for different IDDES models compared to LES. η is defined as the normalized coordinate stretching clockwise around the centerline of the cab with the origin being the lower leading edge.

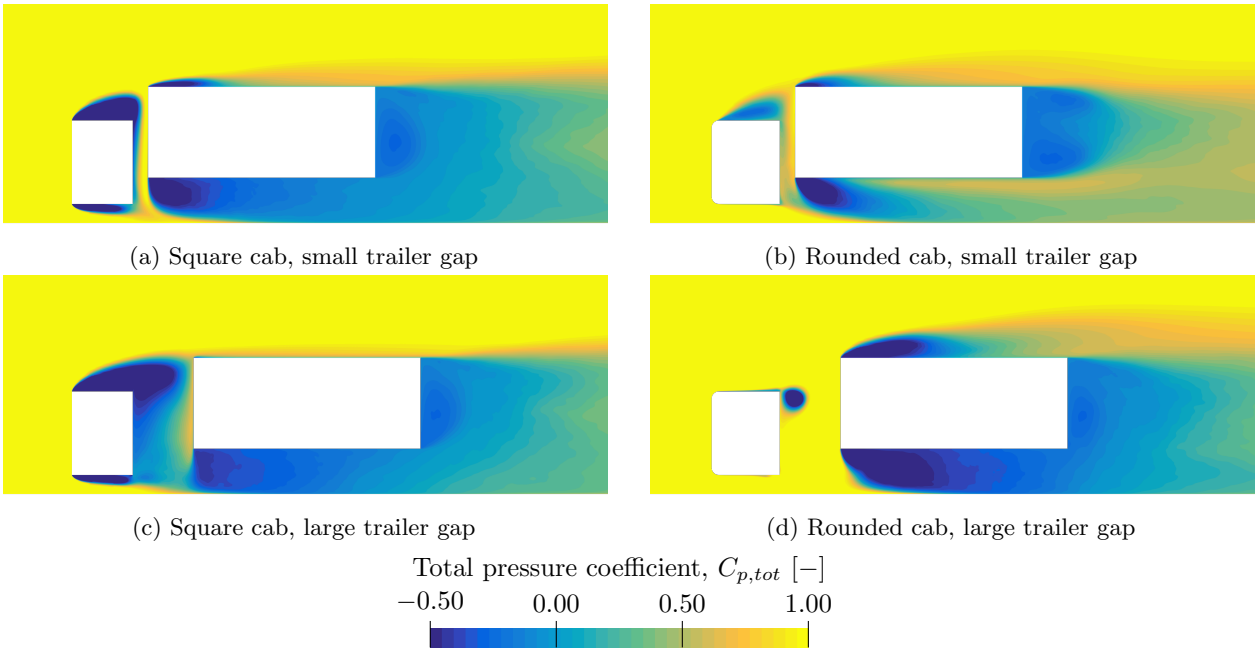

(a) Square cab, small trailer gap

(b) Rounded cab, small trailer gap

(c) Square cab, large trailer gap

(d) Rounded cab, large trailer gap

Figure 3.8: Total pressure coefficient in the plane $y = 0.0\,\text{m}$ for the different geometries using the SA IDDES model.

of the cab the k-ε models predicts a larger pressure than both LES and SA IDDES. However, close to the edge between the top and the rear all k-ε models predicts a peak similar to the LES. This feature is best captured by the DSL = 1.2 k-ε, which shows very good agreement with LES from the rear part of the top surface all along the rear of the cab. At the bottom surface all models except the standard k-ε shows similar behaviors, overpredicting the pressure at the front half of the bottom surface. The standard k-ε predicts the largest pressure of all models at the rear of the bottom surface, however at the front part it predicts the lowest pressure, indicating a difference in the separation compared to the other k-ε models.

In figure 3.9b the pressure is shown for the rounded cab with small trailer gap. Similarly to the square cab the stagnation pressure is overestimated. Furthermore, the pressure at the rounded edges are significantly lower for the k-ε models than for both LES and SA IDDES, indicating a larger acceleration around the corner. At the top surface significant differences are obtained, where the realizable and standard k-ε shows one behavior and the Durbin scale limiter models shows another. In figure 3.10 the total pressure coefficient predicted by the four k-ε models is shown in the symmetry plane $y = 0.0\,\text{m}$. A large difference in the separation above the cab can be noted, were the realizable and standard k-ε models predicts almost no separation and the two Durbin scale limiter models predicts large separation. Studying the drag coefficients it can be seen that the cases where the separation is predicted C_D is underestimated by 1.3% and 4.2%. In the two cases without separation drag is overestimated by 14.5% and 12.1%. For the cases with separation above the cab the separation bubble acts similar to a roof deflector, altering the pressure on the front surface of the trailer. For the cases without separation over the cab, the flow instead separates above and at the sides of the trailer. These differences in separation alters the flow in the cab-trailer gap which is seen in both the illustrations of pressure (figure 3.9b) and total pressure (figure 3.10), which in turns changes the recirculation region below the trailer. On the bottom of the cab similar pressure distributions are predicted by all k-ε models.

For the square cab with large trailer gap (figure 3.9c) all models predicts pressures similar to the SA IDDES model. Furthermore, the pressures of all k-ε models, except the standard k-ε, are similar around the cab. In the case of the rounded cab with large trailer gap (figure 3.9d) some differences can once again be seen at the top surface, indicating that the only model with separation above the cab is the DSL= 0.6 k-ε. At the rear and bottom sides all k-ε models, except the standard k-ε, predicts pressures similar to the SA IDDES.

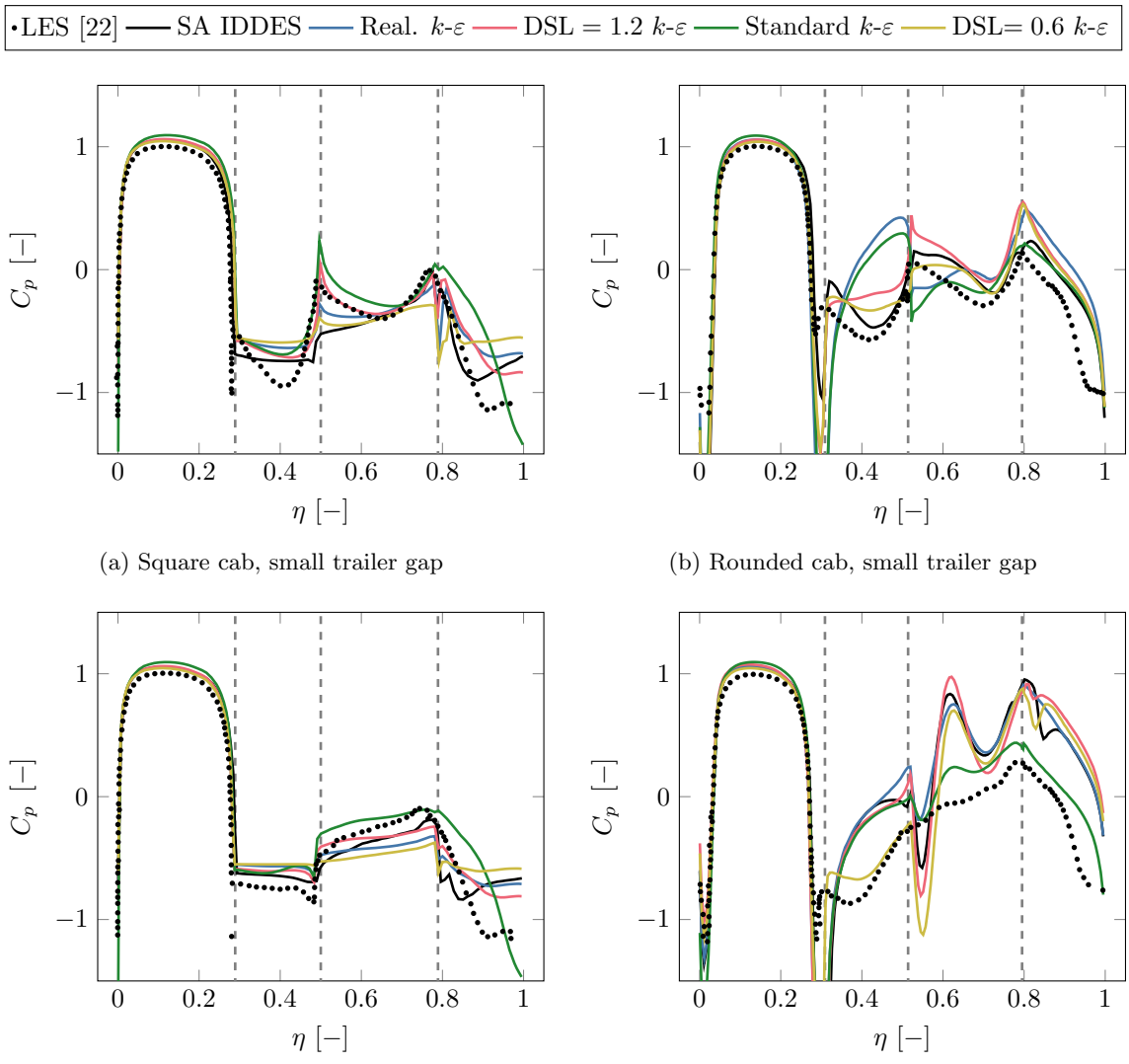

(a) Square cab, small trailer gap

(b) Rounded cab, small trailer gap

(c) Square cab, large trailer gap

(d) Rounded cab, large trailer gap

Figure 3.9: Pressure coefficient around the cab of the simplified truck with square edges and small cab-trailer gap for different k-ε models compared to LES and SA IDDES. η is defined as the normalized coordinate stretching clockwise around the centerline of the cab with the origin being the lower leading edge.

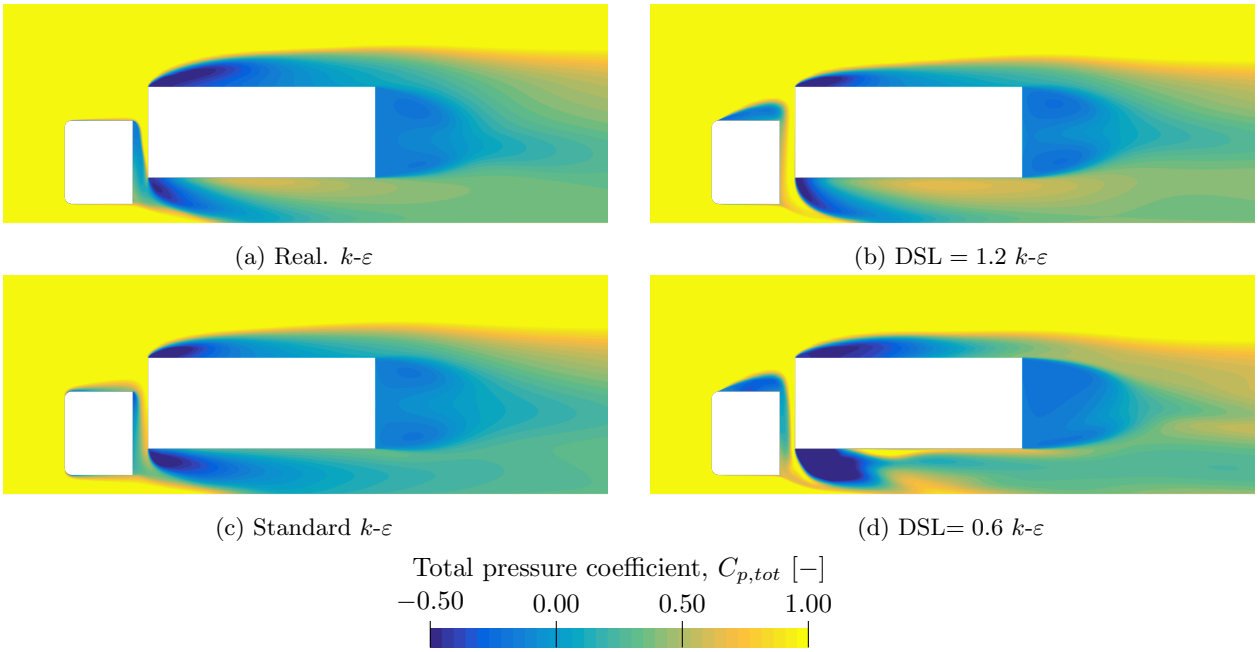

(a) Real. k-ε

(b) DSL = 1.2 k-ε

(c) Standard k-ε

(d) DSL= 0.6 k-ε

Figure 3.10: Total pressure coefficient in the plane $y = 0.0$ m for the rounded cab with small trailer gap using different k-ε models.

Table 3.5: Drag coefficient of the simplified truck for different k-ω models normalized to wind tunnel data, as well as the average error.

Turbulence model	Small gap		Large gap		Average error [%]
	Square	Rounded	Square	Rounded	
LES [22]	1.003	1.030	1.064	0.878	5.5
SA IDDES	0.989	0.935	0.992	1.015	2.5
k-ω	0.811	0.956	0.740	0.987	12.6
DSL = 1.2 $a_1 = 1$ k-ω	0.864	1.143	0.830	1.066	12.9
DSL = 1.2 k-ω	0.842	0.945	0.794	0.969	11.3
$a_1 = 1$ k-ω	0.819	0.925	0.738	0.978	13.5

3.2.4 k-ω models

For the SST k-ω models (hereafter simply denoted k-ω) four different models were evaluated. These were the four possible combinations using a Durbin scale limiter of either 0.6 or 1.2 and an a_1 coefficient of either 0.31 or 1.00. The combination DSL= 0.6 and $a_1 = 0.31$ is the default SST k-ω configuration, and hence denoted only k-ω. Table 3.5 shows the drag coefficient predicted by the different k-ω models, SA IDDES and LES, normalized to wind tunnel data. Additionally the normalized error, averaged over the different geometries, is shown for each model. Based on the average error all k-ω models perform similar in terms of predicting the drag. The drag prediction of the k-ω models is, on average, similar to the drag prediction of the k-ε models. However, there was a larger spread among the k-ε models. Based on the drag predictions the k-ω models seems to better predict the flow for the rounded than for the square cab.

Investigating the pressures around the centerline of the cab in figure 3.11 most k-ω models predict similar pressure distributions. The only notable differences between the k-ω models are obtained at the top of the rounded cab. For the rounded cab with small trailer gap (figure 3.11b) the DSL = 1.2 $a_1 = 1$ model fails to predict the separation. For the rounded cab with large trailer gap (figure 3.11d) the DSL = 1.2 $a_1 = 1$ and the $a_1 = 1$ k-ω models predicts separation above the cab, similar to the SA IDDES model. However the k-ω and the DSL = 1.2 k-ω model predicts no separation above the cab. Interestingly these models predicts a pressure

Table 3.6: Drag coefficient of the simplified truck for the $\overline{v^2}$-f, Reynolds Stress and Spalart-Allmaras models normalized to wind tunnel data, as well as the average error.

Turbulence model	Small gap		Large gap		Average error [%]
	Square	Rounded	Square	Rounded	
LES [22]	1.003	1.030	1.064	0.878	5.5
SA IDDES	0.989	0.935	0.992	1.015	2.5
$\overline{v^2} - f$	0.777	0.897	0.695	1.038	16.7
RSM	0.801	1.038	0.716	1.032	13.8
SA	0.875	0.982	0.851	0.958	8.4

very similar to the LES results. This might indicate that the radius of the cab is very close to the limit at which separation occurs, resulting in similar turbulence models predicting vastly different separation.

As noted above the k-ω models more accurately predicts the drag of the rounded models than the drag of the square models. However, based on the pressure at the cab centerline of both square cabs (figure 3.11a and 3.11c) no major deviations from the LES and SA IDDES data is noted. However, the drag coefficient is underpredicted by between 15% and 25% for these cases. In figure 3.12 the total pressures fields obtained from the k-ω models are compared to the total pressure fields from SA IDDES for the square truck with large trailer gap (since the IDDES fields are believed to be accurate for this geometry). In the figure the total pressure is shown in the planes $y = 0.0\,\text{m}$ and $z = 1.5\,\text{m}$. The k-ω and the $a_1 = 1$ k-ω models predicts a larger separated region above and behind the cab than the two remaining k-ω models. Similarly the k-ω and the $a_1 = 1$ k-ω models also predicts slightly larger separation at the sides compared to the remaining k-ω models. Comparing all k-ω models to the SA IDDES (figure 3.12i and 3.12j) the IDDES models results in the smallest separation, both above and at the sides of the cab. The separation bubbles at the sides of the cab collapses into the cab-trailer gap, increasing the pressure on the front face of the trailer and altering the base wake. However, these differences in the flow field mainly affects the pressure on the trailer and the outer parts of the cab, explaining why no major deviations were noted for the pressure along the centerline of the cab.

3.2.5 v2-f, Reynolds Stress and Spalart-Allmaras models

In addition to the unsteady IDDES models and the steady two-equation models presented above three alternative models were evaluated. These were the $\overline{v^2}$-f and Reynolds stress models, where solving additional equations are supposed to increase the accuracy, as well as the Spalart-Allmaras model, where the turbulence is represented by a single equation. In table 3.6 the normalized drag and the average error of these models are presented and compared to LES and SA IDDES. The average errors of the $\overline{v^2}$-f and RSM models are slightly larger than the errors of the k-ω models and approximately the same as those of the worst k-ε models. However the Spalart-Allmaras model results in the lowest average error among all RANS models. Similar to the k-ω models, these models more accurately predicts the drag for the rounded than for the square cab.

Comparing the pressures around the centerline of the cab (figure 3.13) the most significant difference is, once again, whether the flow is separated at the top of the cab or not. For the square cabs (figure 3.13a and 3.13c) the best agreement to LES and SA IDDES data is obtained for the Spalart-Allmaras model. For the rounded cab with large trailer gap (figure 3.13d) the RSM model shows good agreement to SA IDDES over large areas of the cab.

3.3 Conclusions

From the investigations above it was found that the two unsteady IDDES models provided the best correlation to experimental data, both in terms of C_D and ΔC_D. Furthermore the different near-wall models of the IDDES models performed similarly, with the Spalart-Allmaras model performing slightly better than the SST k-ω model. Additionally the SA IDDES model was slightly faster. However, both models will be investigated for the detailed truck.

Evaluating the k-ε models it was found that the standard k-ε and DSL = 1.2 k-ε models showed the best

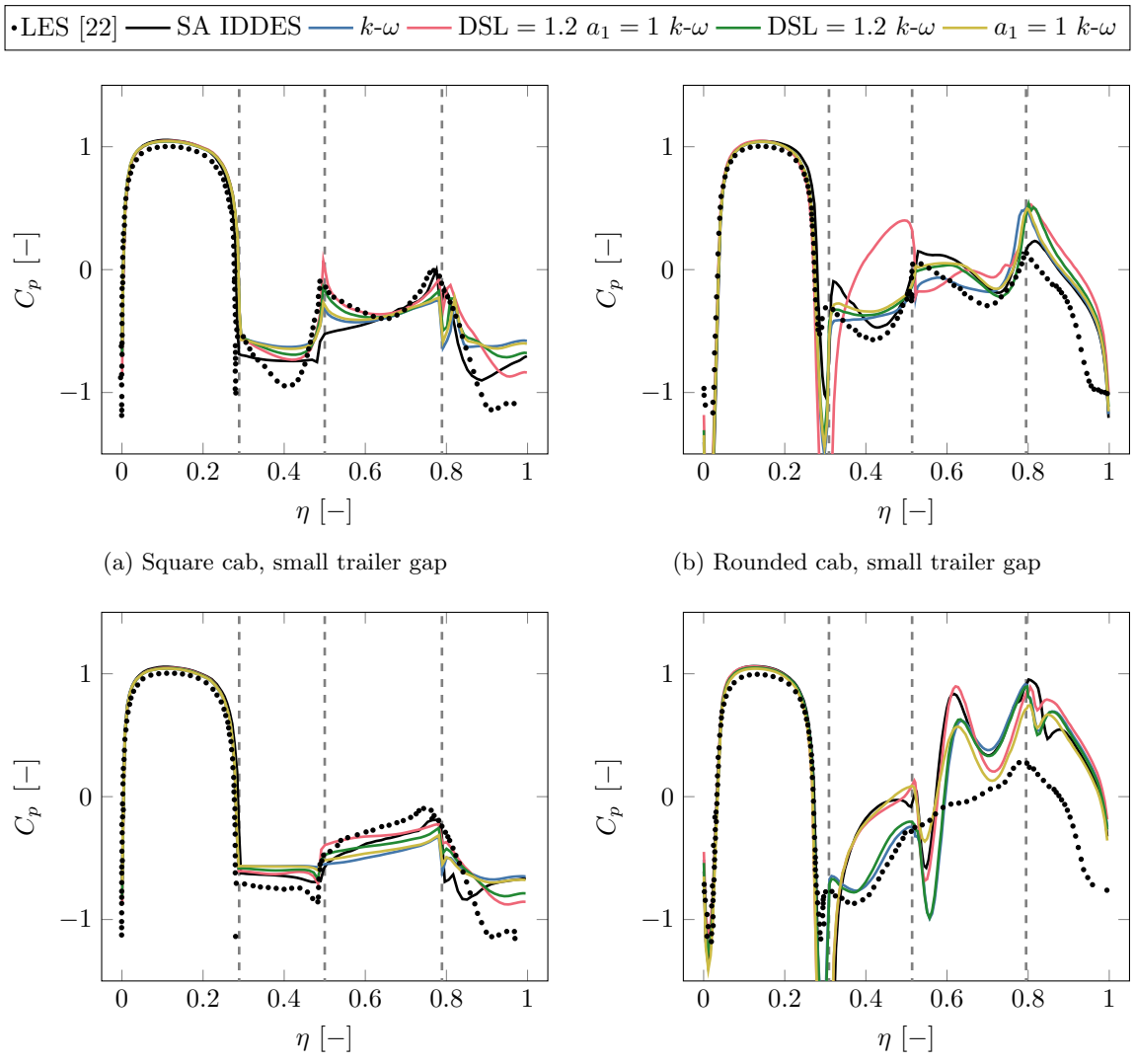

(a) Square cab, small trailer gap

(b) Rounded cab, small trailer gap

(c) Square cab, large trailer gap

(d) Rounded cab, large trailer gap

Figure 3.11: Pressure coefficient around the cab of the simplified truck for different k-ω models compared to LES and SA IDDES. η is defined as the normalized coordinate stretching clockwise around the centerline of the cab with the origin being the lower leading edge.

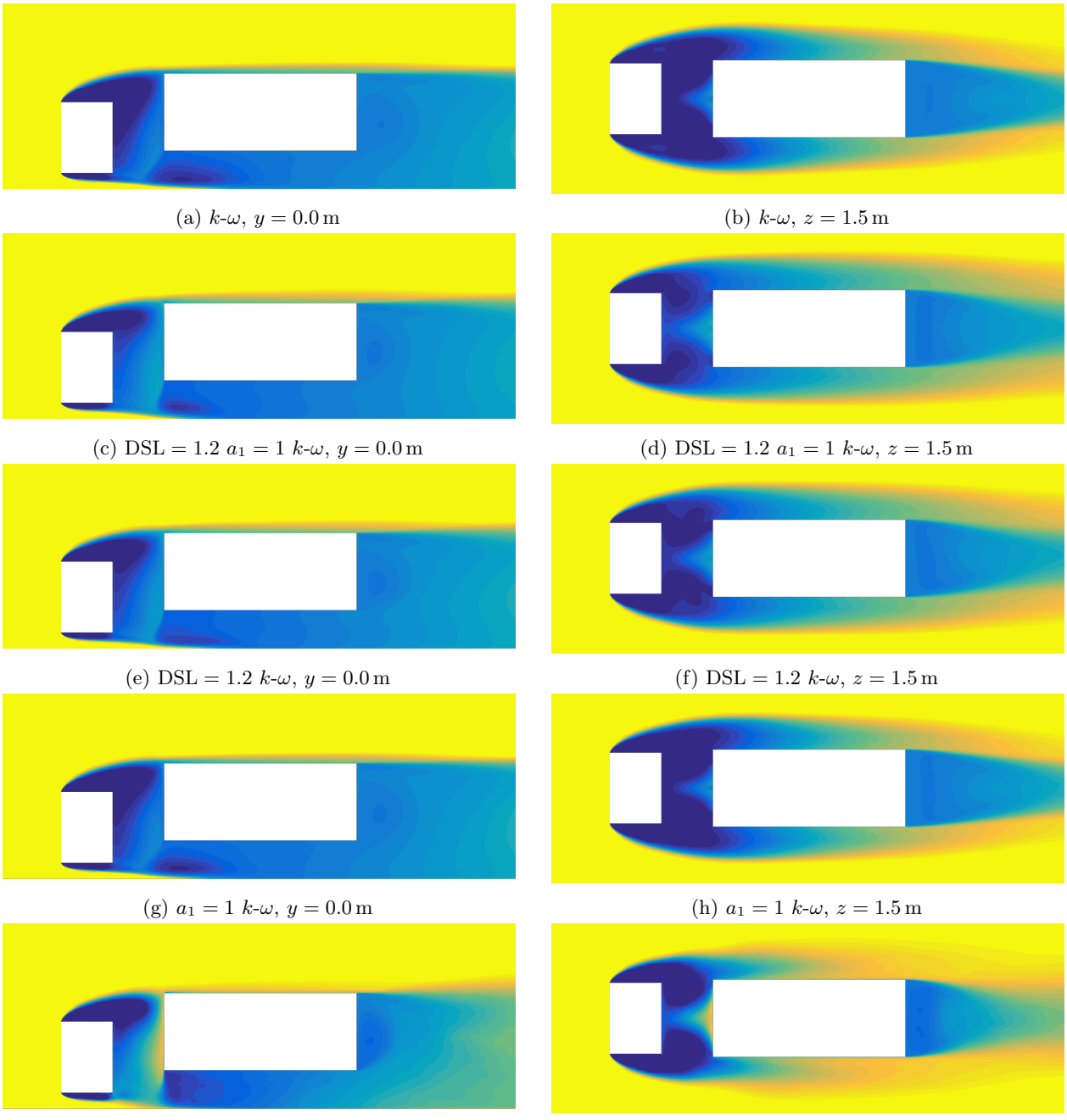

(a) k-ω, $y = 0.0\,\mathrm{m}$

(b) k-ω, $z = 1.5\,\mathrm{m}$

(c) DSL = 1.2 $a_1 = 1$ k-ω, $y = 0.0\,\mathrm{m}$

(d) DSL = 1.2 $a_1 = 1$ k-ω, $z = 1.5\,\mathrm{m}$

(e) DSL = 1.2 k-ω, $y = 0.0\,\mathrm{m}$

(f) DSL = 1.2 k-ω, $z = 1.5\,\mathrm{m}$

(g) $a_1 = 1$ k-ω, $y = 0.0\,\mathrm{m}$

(h) $a_1 = 1$ k-ω, $z = 1.5\,\mathrm{m}$

(i) SA IDDES, $y = 0.0\,\mathrm{m}$

(j) SA IDDES, $z = 1.5\,\mathrm{m}$

Figure 3.12: Total pressure coefficient in the planes $y = 0.0\,\mathrm{m}$ and $z = 1.5\,\mathrm{m}$ for different k-ω models and SA IDDES.

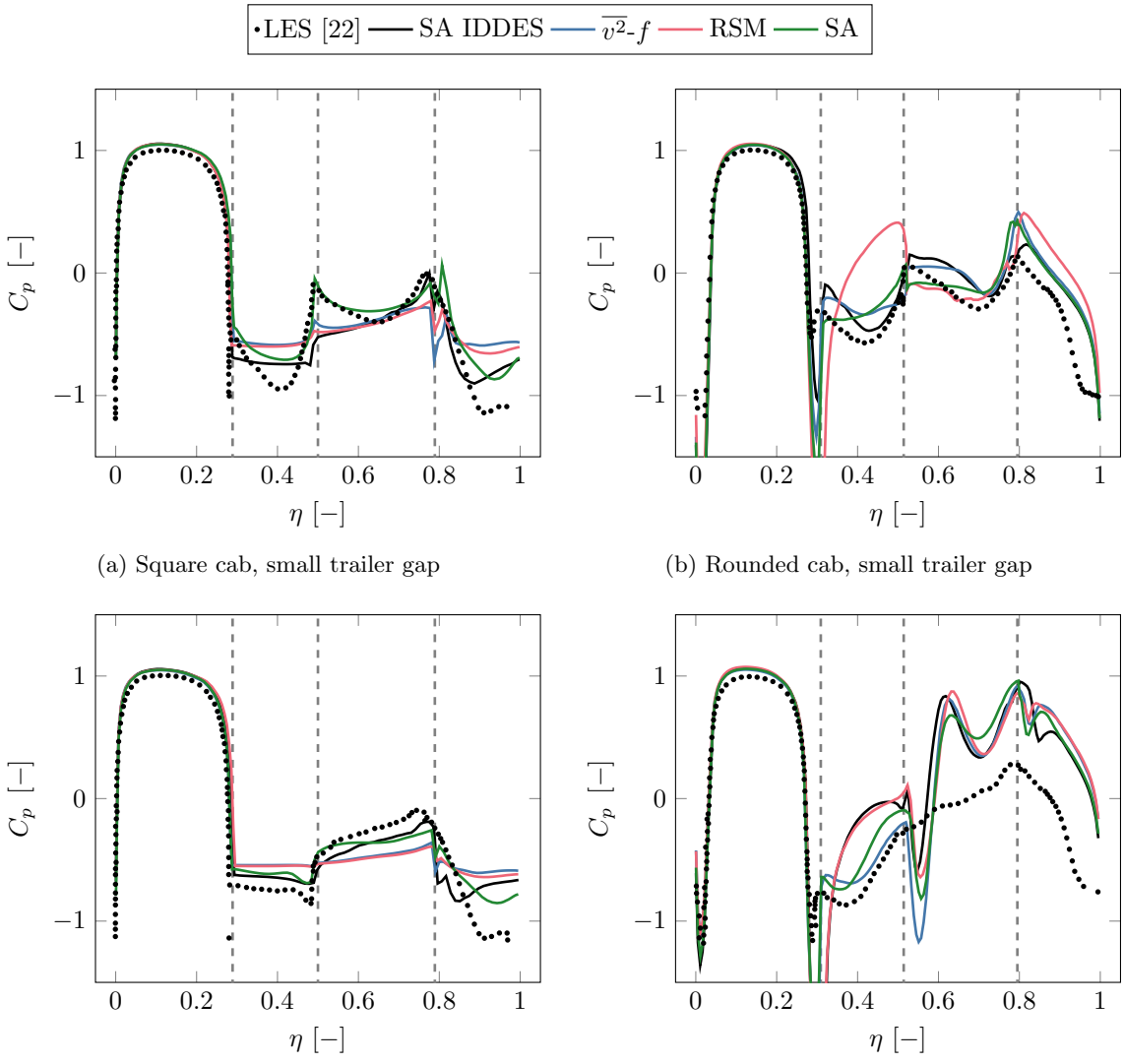

(a) Square cab, small trailer gap

(b) Rounded cab, small trailer gap

(c) Square cab, large trailer gap

(d) Rounded cab, large trailer gap

Figure 3.13: Pressure coefficient around the cab of the simplified truck for the $\overline{v^2}$-f, Reynolds Stress and Spalart-Allmaras models compared to LES and SA IDDES. η is defined as the normalized coordinate stretching clockwise around the centerline of the cab with the origin being the lower leading edge.

correlation to both the experimental C_D and ΔC_D. However, it was found that the standard k-ε model correlated worse than the DSL = 1.2 k-ε model to LES and IDDES in terms of pressure. Therefore only the DSL = 1.2 k-ε model will be tested for the detailed truck.

In terms of the k-ω models the drag prediction was, in general, worse than for the k-ε models. However the k-ω models better predicted the drag of the rounded cab. For the detailed truck it is believed that one of the most complex flow features to predict is the flow over the rounded cab front edges. Hence at least one k-ω model should be included in that study. The DSL = 1.2 k-ω model obtained the smallest average drag error and will therefore be included in the detailed study. Additionally the DSL = 1.2 $a_1 = 1$ k-ω model will be included since it is recommended in the StarCCM+ best practices and is therefore considered as an interesting baseline for k-ω models.

Finally three alternatives to the two-equations eddy viscosity models where evaluated. Among these no improvement in correlation compared to the k-ε and k-ω models were obtained for either the $\overline{v^2} - f$ or the RSM model. Furthermore, the additional equations introduced by these models increased the solver time with approximately 20% and 90% for the $\overline{v^2} - f$ and RSM models, respectively. Therefore these models will not be further investigated. The Spalart-Allmaras model proved to result in the best correlation in terms of both C_D and ΔC_D among the RANS models. Therefore the Spalart-Allmaras model will be included for the investigations of the detailed truck.

4 Turbulence modelling - detailed truck

Based upon the study using the simplified truck, six turbulence models were chosen to be evaluated using a detailed truck geometry. This chapter will firstly present the methodology used, followed by the results being presented and analyzed.

4.1 Method

Since both the investigations of the simplified and the detailed truck used the Volvo standardized CFD process, the methodology used in the studies are similar. This section will therefore focus on the differences between the two studies.

4.1.1 Geometry

For the analyses of an actual truck CAD geometry a specific individual, FH-1823 will be used. One of the main reasons for choosing this geometry is because it has been tested in the National Research Council (NRC) 9 m wind tunnel. The model will first be evaluated in a baseline setup. Later, simulations will be performed with an upgrade package installed in order to evaluate the prediction of configuration deltas. Since it is desired to evaluate the model at different yaw angles a full length trailer cannot be used, since the wind tunnel is too narrow. Therefore a shorter trailer (9.1 m) is used in the wind tunnel tests and simulations. The FH-1823 and the shorter trailer is shown in figure 4.1.

4.1.2 Wind tunnel tests

Wind tunnel tests were performed in the NRC 9 m wind tunnel in Ottawa, Canada. The wind tunnel has a test section of 9.1 m × 9.1 m × 25 m, a 6.1 m diameter turntable and measures forces and moments using a six-component balance. [23] The truck is mounted by attaching the rear wheels of the tractor to the balance, with the front and trailer wheels being supported by air bearings. Hence all the wheels are stationary. The mounting solution can be seen in figure 4.1. The air bearings are placed on 40 mm tall platforms. These are shown in red in figure 4.2 and are shaped such that the truck can be yawed $\pm 10°$. Figure 4.2 also illustrates how the yaw angle is defined where, seen from above, a positive yaw angle corresponds to a clockwise rotation of the turntable. The setup allows for measuring drag and side force, as well as yaw moment.

In order to be able to correlate the simulations to the uncorrected wind tunnel data the simulations were performed with a model of the NRC tunnel, illustrated in figure 4.3. The figure also illustrates the different parts of the wind tunnel. The model consisted of the converging nozzle, test section and diffuser. In order to minimize unwanted influence from the inlet and outlet boundary conditions extensions were added upstream the converging nozzle and downstream the diffuser. The test section of the wind tunnel model was constructed from measurements provided by NRC. However, NRC does not provide drawings of the converging nozzle or diffuser. The contraction ratio and diffuser angle have been published [24], and were therefore also known. The remaining measurements were approximated from photos. The solid blockage from the truck in the tunnel is approximately 13%.

The NRC tunnel has a boundary layer control system consisting of two suction zones. However, this system was not used during the tests. The boundary layer has been measured for different positions in the empty wind tunnel. These measurements have shown good agreement to flat plate boundary layer theory. [25] As an attempt to improve the accuracy of the simulations an empty tunnel was simulated and the boundary layer was compared to experimental data. With the flat plate boundary layer theory as a starting point the boundary layer height was tuned to match experiments. This was done by moving the transition from slip to no-slip wall at the floor in front of the test section.

The velocity at the tunnel inlet was set to 15 km/h, corresponding to a velocity of 90 km/h in the test section of the empty tunnel. The pressure at the outlet was set to 0 Pa. Since the large blockage introduces non-negliable pressure losses a non-zero reference pressure was used when calculating the pressure and total pressure coefficients. This reference pressure, P_{ref}, was obtained by monitoring the stagnation pressure, P_0, in front of

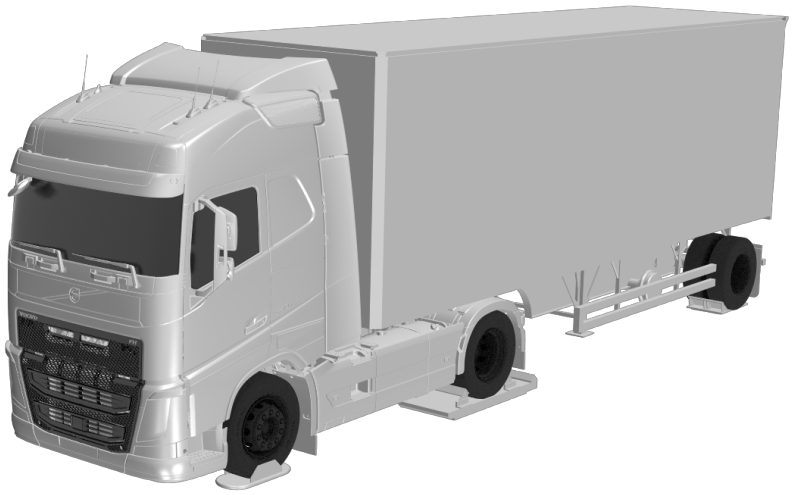

Figure 4.1: FH-1823 with the shorter trailer and wind tunnel mounting.

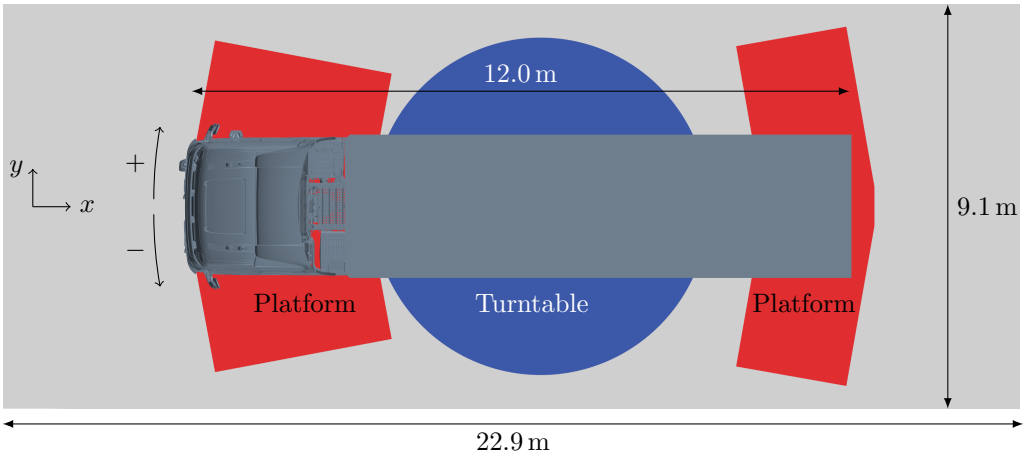

Figure 4.2: Placement of the truck in the test section with the turntable and the platforms for the air bearings.

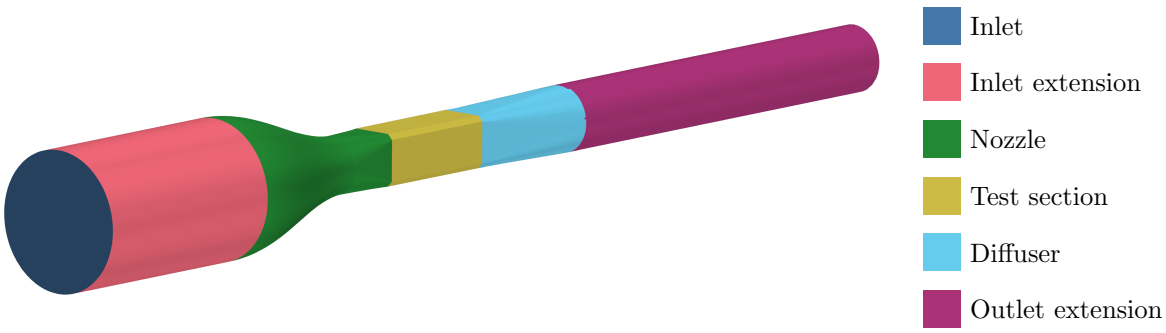

Figure 4.3: Geometry of the NRC wind tunnel used in the simulations with the names of the different parts. Note that the outlet is not visible.

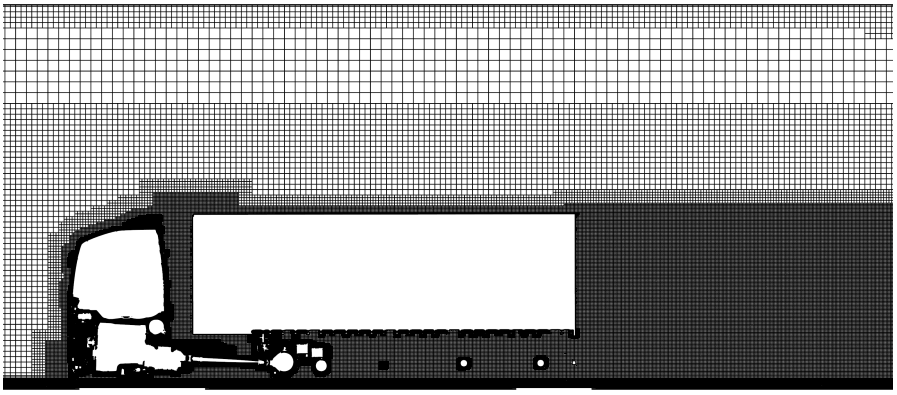

(a) $y = 0.0\,\mathrm{m}$

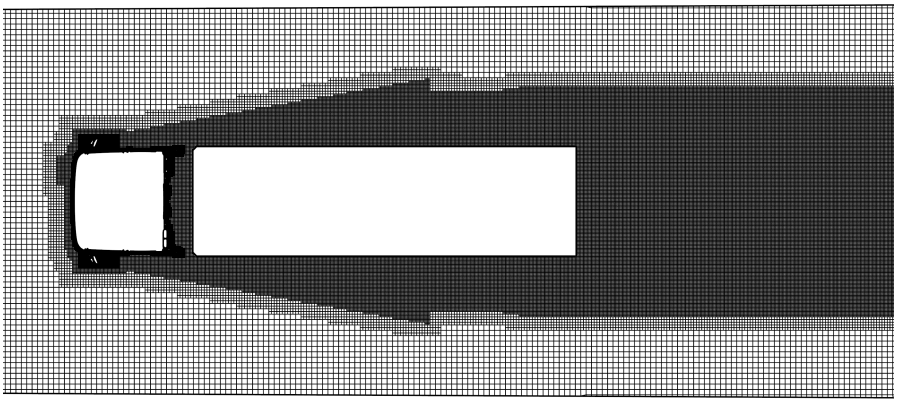

(b) $z = 2.0\,\mathrm{m}$

Figure 4.4: Mesh used for simulations of the detailed truck in the NRC wind tunnel.

the truck. Using Bernoulli's principle the reference pressure was calculated as

$$P_{\mathrm{ref}} = P_0 - \frac{\rho v_\infty^2}{2}. \tag{4.1}$$

4.1.3 Mesh

Similarly to the simplified truck, the detailed truck was meshed using a version of the standardized CFD process at Volvo. This resulted in a mesh of approximately 170 million cells, with a low y^+ approach on the tractor and a high y^+ on the trailer. Refinement boxes were placed where large gradients were anticipated, such as around the mirrors and the roof deflector. Furthermore, wake refinements with a spread of $\pm 10°$, starting at the front of the tractor and extending 8 m behind the trailer, were created. Since the simulations were performed using the wind tunnel model some care was taken to ensure that important aspects of the physics of the tunnel was resolved in the simulations. These included adequate resolution of boundary layers at the walls, in particularly the floor. Additionally the positioning of the truck was adjusted according to documentation from the test. In figure 4.4 the mesh is shown in the planes $y = 0.0\,\mathrm{m}$ and $z = 2.0\,\mathrm{m}$.

4.1.4 Turbulence models

The turbulence models used were based on the results from the study of the simplified truck, see section 3. The models investigated for the detailed truck is presented in table 4.1. Similarly to the simulations of the simplified truck the RANS simulations were run for 10000 iterations. However, due to the high computational cost, the unsteady simulations were only run for 5 s and averaged for 3 s. The unsteady simulations were initialized with a standard k-ε RANS method run for 1000 iterations.

Table 4.1: Turbulence models evaluated for the detailed truck.

Turbulence model	Implementation	Denotation
k-ε	Standard with Durbin scale limiter of 1.2	DSL = 1.2 k-ε
SST k-ω	Durbin scale limiter of 1.2 and $a_1 = 1$	DSL = 1.2 $a_1 = 1$ k-ω
	Durbin scale limiter of 1.2	DSL = 1.2 k-ω
Spalart-Allmaras	Standard	SA
IDDES	SST k-ω in near-wall region	SST IDDES
	Spalart-Allmaras in near-wall region	SA IDDES

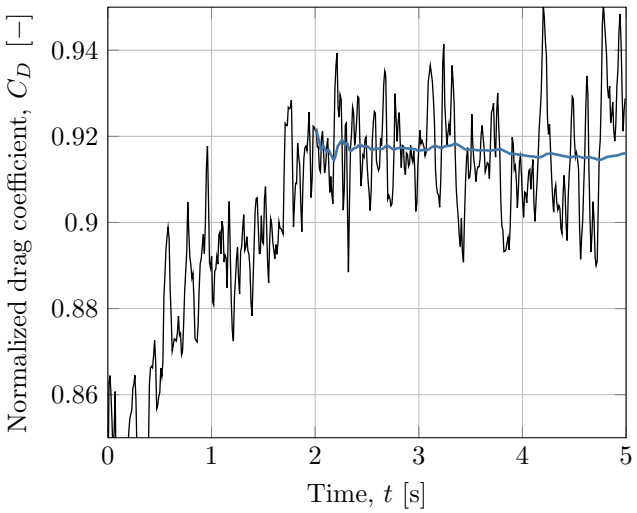

Figure 4.5: Instantaneous and running average of the drag coefficient normalized to the value measured in the wind tunnel.

4.1.5 Post-processing

Since the truck introduces a large blockage the measurements of the dynamic pressure, used to calculate the non-dimensional quantities such as the force coefficients, might be affected. Unfortunately the exact measurement setup has not been shared by NRC. Therefore the velocity used to calculate the non-dimensional quantities of the simulations was taken as the surface average of the streamwise velocity in the beginning of the test section. According to engineers at the NRC this approach should produce similar results as the method used in the actual wind tunnel.

The results presented in this section have, unless specifically mentioned, been averaged. For the steady state RANS simulations the last 1000 iterations were used to average both the fields and the force coefficients. In order to determine the averaging span required for the unsteady simulations the time dependency of the drag was investigated. Figure 4.5 shows the normalized value of the instantaneous drag coefficient, as well as the running average starting at $t = 2\,\text{s}$, as a function of time for an IDDES simulation. In the figure it can be seen that the drag initially increases from the value predicted by the steady RANS method, used to initialize the IDDES. After approximately two seconds the drag starts oscillating around one value. Figure 4.5 also shows the result of this averaging in terms of the running average. When examining the converge of the running average it was found that a simulated time of five seconds was sufficient to obtain a fluctuation of the running average smaller than 0.5% during the last second. The 3 s averaging span corresponded to an averaging period of 6.1 flow passages over the truck and 3.3 flow passages through the test section.

The fields obtained from the simulations will be illustrated using the planes $y = 0.0\,\text{m}$ and $z = 2.0\,\text{m}$. The y-plane is placed along the centerline of the truck and the z-plane is located at the height of the rear-view mirrors. The planes are illustrated in figure 4.6.

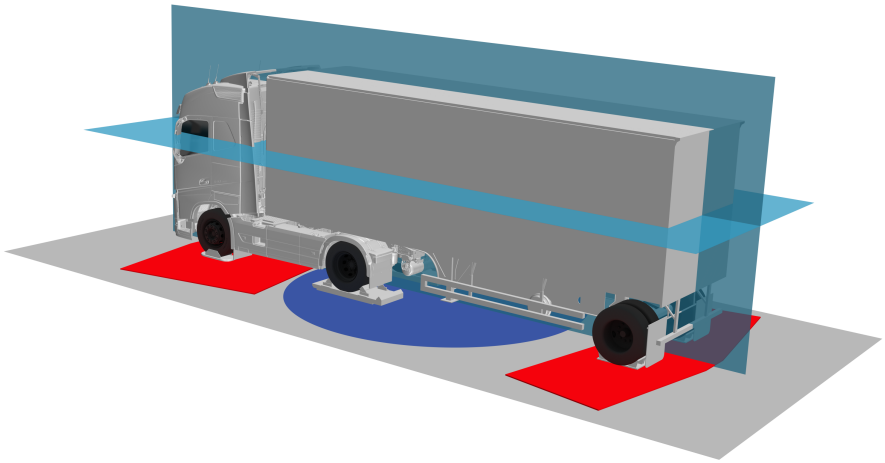

Figure 4.6: The planes $y = 0.0\,\text{m}$ and $z = 2.0\,\text{m}$ used to illustrate the flow fields.

Local drag

The drag of a vehicle can be investigated by adding the pressure and shear forces at the vehicles surface. Due to these forces a reaction force will be exerted from the vehicle to the air, corresponding to the drag. This response can be visualized using the local drag and illustrates the losses in the flow field. The local drag can be divided into three terms, representing the total pressure losses, the longitudinal kinetic energy losses and the vortical resistance, and is given by [12]

$$C_D A = \int_S \left[(1 - C_{p,tot}) - \left(1 - \frac{v_x}{v_\infty}\right)^2 + \left(\frac{v_y^2 + v_z^2}{v_\infty^2}\right) \right] dS. \tag{4.2}$$

Turbulent kinetic energy

The turbulent kinetic energy, k, will be used to investigate and explain the flow structures predicted by the different turbulence models. Using the steady state k-ε and k-ω models the turbulent kinetic energy is obtained as part of the solution. However the Spalart-Allmaras model does not solve for the turbulent kinetic energy, hence it will be approximated using equation (2.14) presented in section 2.2.1.

For the IDDES models the turbulent kinetic energy can be divided into a resolved, k_{res}, and a modelled, k_{mod}, part. The resolved part can be calculated using the velocity fluctuations as

$$k_{\text{res}} = \frac{\overline{v_x'^2 + v_y'^2 + v_z'^2}}{2}. \tag{4.3}$$

The modelled part of the turbulent kinetic energy is calculated similarly to as for the RANS method. For the SST IDDES k_{mod} is solved for by the k-ω model and for the SA IDDES the approximation discussed above is used. When comparing the turbulent kinetic energy predicted by the RANS and the IDDES models the total turbulent kinetic energy, $k_{\text{res}} + k_{\text{mod}}$, will be presented for the IDDES models.

4.1.6 DES performance

Before performing multiple DES simulations it is desired to evaluate the performance of the simulations. This can be done by examining quantities such as the IDDES blending function, modelled compared to resolved turbulent kinetic energy as well as the Courant-Freidrichs-Lewy (CFL) number. The IDDES blending function, $\tilde{f}_d$ in equation (2.21), illustrates where the solver uses RANS mode ($\tilde{f}_d = 1$) and LES mode ($\tilde{f}_d = 0$) and is shown in figure 4.7. It can be seen that the solver operates in LES mode in most of the domain except close to the walls of the truck and tunnel. Furthermore it can be seen that the RANS region is smaller at the cab than at the trailer, which is to be expected because of the different y^+ approaches.

In figure 4.8 the resolved and modelled turbulent kinetic energy is illustrated in the planes $y = 0.0\,\text{m}$ and $z = 2.0\,\text{m}$. A guideline is that the resolved turbulent kinetic energy should account for at least 80% of the total

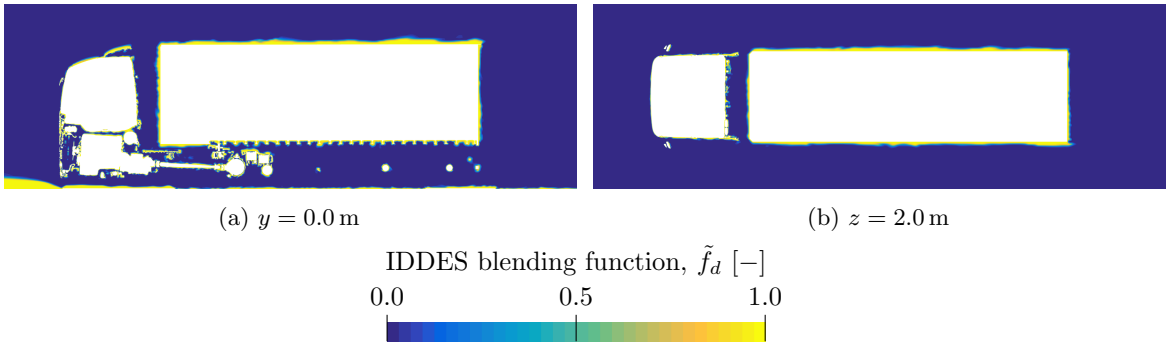

Figure 4.7: IDDES blending function for the SST IDDES at zero yaw.

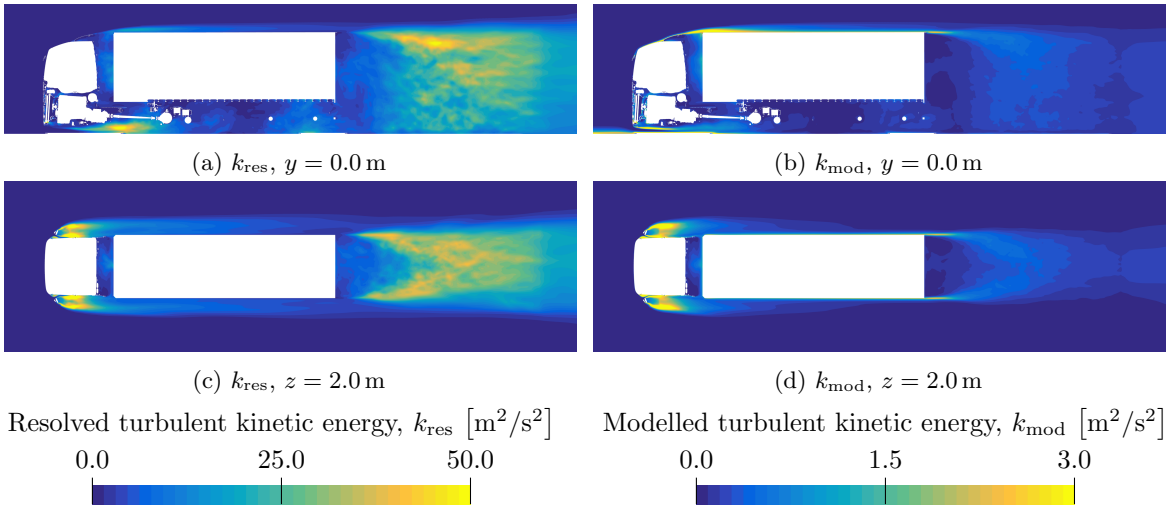

Figure 4.8: Resolved and modelled turbulent kinetic energy for the SST IDDES at zero yaw. Note the difference in scales.

turbulent kinetic energy. [12] Observing the difference in scales between the resolved and the modelled fields it can be seen that this is fulfilled. Furthermore it can be seen that the thinner shear layers are the regions were the most turbulence is modelled. This is seen at the trailer base, rear-view mirrors, roof deflector as well as the entry to the underbody.

The CFL number describes how information is propagated over the mesh in terms of how many cells the flow passes during a time step. It is recommended that the CFL number is less than unity in the domain. [26] In figure 4.9 the CFL number is illustrated in two planes. For most parts of the domain the CFL number fulfills the criteria. However, around the cab radius and mirrors the combination of a fine mesh and large velocities caused by the acceleration around the radius results in larger CFL numbers, around 3, which could impact the separation. The CFL number could be reduced by either reducing the time step or increasing the mesh size in the region. Both of these options are problematic. Since one of the purposes of this chapter is to investigate the difference between RANS and IDDES it is desired to keep as many aspects as possible the same, which includes the mesh. Since it is believed that the RANS methods benefit from the fine mesh around the radius and mirrors the mesh will not be altered. Hence the remaining option is to change the time step. However this significantly increases the computational cost of the unsteady methods, reducing the industrial relevance of the method compared to RANS. Therefore neither the mesh or the time step will be altered. However it should be kept in mind that the CFL number might be too large.

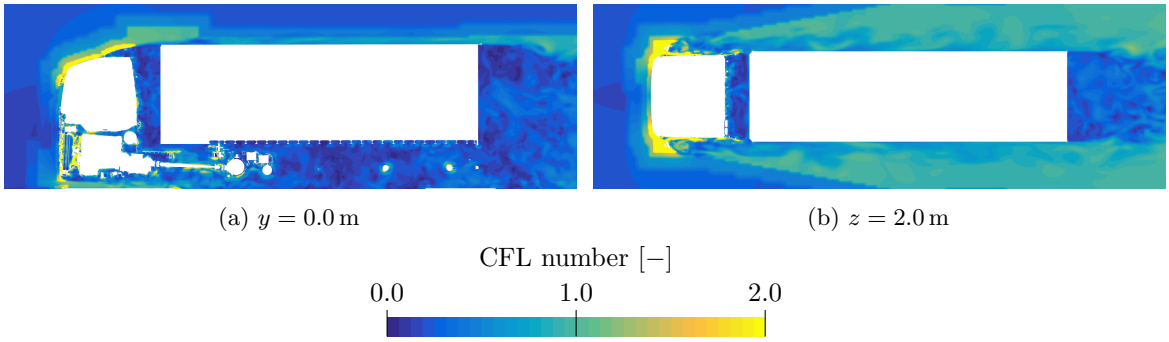

(a) $y = 0.0\,\mathrm{m}$ (b) $z = 2.0\,\mathrm{m}$

Figure 4.9: CFL number for the SST IDDES at zero yaw. Note that this field was not time averaged. Instead the instantaneous field at $t = 5.0\,\mathrm{s}$ is shown.

Table 4.2: Drag coefficient of the detailed truck for different turbulence models. The values at each yaw angle are normalized to wind tunnel data.

Turbulence model	Yaw angle [°]					Average error [%]
	0.0	−2.5	−5.0	−7.5	−10.0	
DSL = 1.2 k-ε	0.869	0.914	0.973	0.992	0.995	6.4
DSL = 1.2 $a_1 = 1$ k-ω	0.882	0.917	0.974	0.994	0.997	5.9
DSL = 1.2 k-ω	0.935	0.923	0.977	1.001	1.016	6.0
SA	1.002	0.980	1.014	1.037	1.035	1.6
SST IDDES	0.923	0.972	1.015	1.018	1.017	3.5
SA IDDES	0.929	0.980	1.019	1.026	1.020	3.3

4.2 Results

Based upon the results of the study with the simplified truck six different turbulence models were evaluated for the detailed truck in the NRC wind tunnel. A yaw sweep from 0.0° to −10.0° with a step of 2.5° was conducted for every model. In the section below the results from this study will be presented. Firstly, an overview of the prediction of drag and side force will be given, followed by a presentation of the computational cost and numerical stability of the models. Finally, a more detailed analysis of the flow fields will be performed. This analysis will focus on the 0.0° and −5.0° cases. Because of confidentiality the absolute values of drag are not presented. Instead, the drag values predicted by the different models have been normalized using the value measured in the wind tunnel for each yaw angle.

4.2.1 Overview of drag prediction

In table 4.2 and figure 4.10 the drag coefficients predicted by the different models are presented for all yaw angles. Furthermore, table 4.2 also presents the average error of each model, defined similarly as for the simplified truck according to equation (3.1). In general the models underpredict the drag at the small yaw angles, 0.0° and −2.5°. For the larger yaw angles the correlation improves with the predicted values being closer to experimental data. Comparing the different models it can be seen that the k-ε and the DSL = 1.2 $a_1 = 1$ k-ω models performs similarly for all yaw angles. Furthermore, the DSL = 1.2 k-ω model predicts slightly larger values of C_D, especially at zero yaw. All three of the k-ε and k-ω models have an average error of approximately 6%. The Spalart-Allmaras model has the smallest average error (1.6%) and is the only model which accurately predicts the drag at small yaw angles. Both IDDES models perform similarly, with the Spalart-Allmaras near-wall model predicting the drag slightly better at small yaw angles but the SST k-ω model performing better at the large angles. Compared to the k-ε and k-ω RANS models the IDDES models results in approximately half the average error.

Using an upgrade package, tested in the same wind tunnel campaign as the baseline, simulations were performed in order to compare the prediction of ΔC_D. In table 4.3 and figure 4.11 the predicted differences are presented for the different turbulence models at 0.0° and −5.0° yaw. Note that the values are not normalized and are

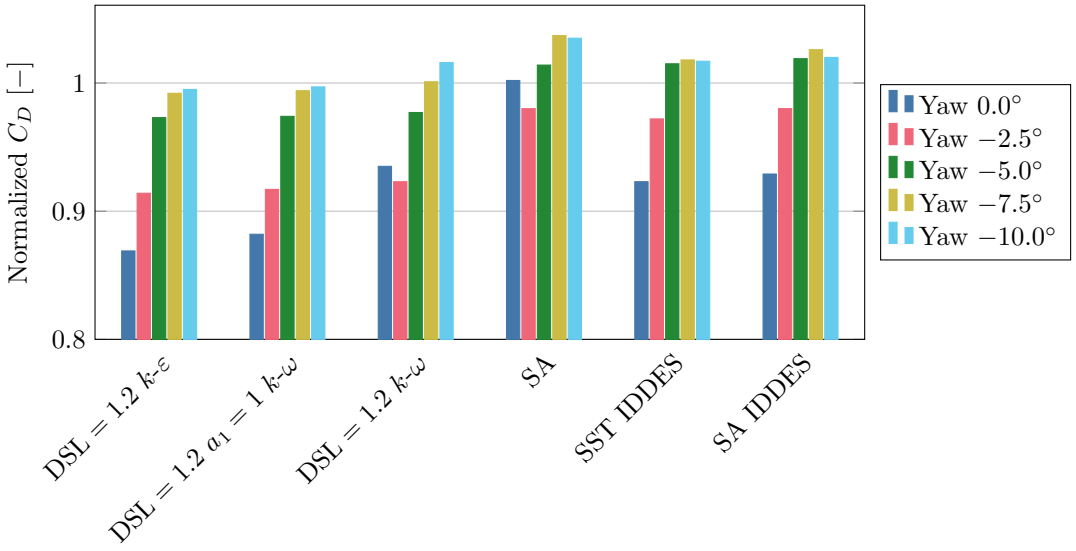

Figure 4.10: Drag coefficient of the detailed truck for different turbulence models and yaw angles. The drag coefficients are normalized to wind tunnel data for each yaw angle.

Table 4.3: Configuration difference of the drag coefficient for different turbulence models compared to wind tunnel data. These values are not normalized and are presented as drag counts.

Turbulence model	Yaw angle [°]		Overprediction
	0.0	−5.0	
Exp.	−16	−19	
DSL = 1.2 k-ε	−20	−40	1.68
DSL = 1.2 a_1 = 1 k-ω	−27	−30	1.64
DSL = 1.2 k-ω	−53	−28	2.40
SA	−19	−26	1.27
SST IDDES	−18	−42	1.64
SA IDDES	−14	−38	1.44

being presented in terms of drag counts. Table 4.3 also presents the overprediction factor, defined as the average percentual error of the predictions, compared to the difference measured in the wind tunnel. The lowest overprediction is obtained for the Spalart-Allmaras model, which accurately predicts the difference at both yaw angles. The SA IDDES model resulted in the second to lowest overprediction, with a factor of 1.44. Furthermore, similar performance was obtained from the SST IDDES, DSL = 1.2 k-ε and DSL = 1.2 $a_1 = 1$ k-ω models. However, it should be noted that comparing the overprediction factors can be misleading. As an example both IDDES models predicts the ΔC_D at zero yaw with an error of two drag counts. Since this ΔC_D is overpredicted by the SST k-ω model and underpredicted by the SA IDDES model the overprediction factor differs despite the error being the same. Finally, the worst prediction of ΔC_D is seen for the DSL = 1.2 k-ω model which vastly overpredicts the difference at zero yaw. However, the prediction at −5.0° is similar to the other models. As a general note it can be seen that the models better predicts the drag difference at zero yaw than at −5.0° yaw.

4.2.2 Side force prediction

In addition to measuring the drag force the setup in NRC also allows for measuring the side force. The side force is defined as positive in the y-direction (see figure 4.2) and is therefore typically negative for negative yaw angles. Since the side force varies significantly with the yaw angle the results will be presented in terms of percentual error compared to the experimental value. This is shown in figure 4.12. Note that the error at zero yaw is not presented. Since the truck is nearly symmetrical the measured side force at zero yaw is

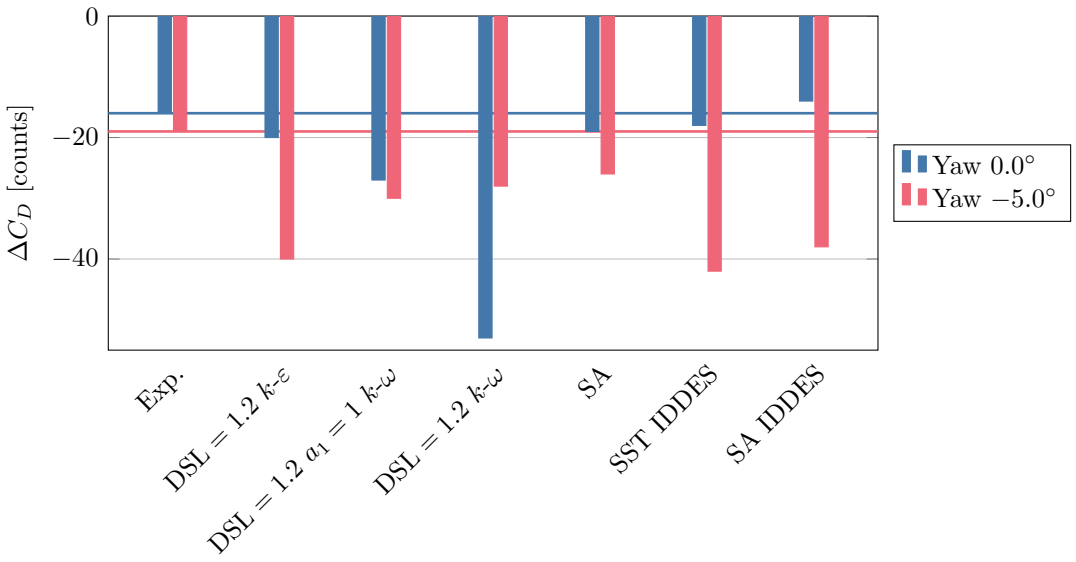

Figure 4.11: Prediction of drag configuration difference, ΔC_D, at 0.0° and −5.0° yaw.

small. Hence deviations between the CFD and wind tunnel data that normally would be considered negligible can result in large errors. Investigating the results significant differences can be noted between the RANS and the IDDES models. The magnitude of the side force is consistently underestimated by the RANS models and, apart from one yaw angle, overestimated by the IDDES models. Furthermore, unlike the drag, all four RANS models predicts similar results. However, similarly to the drag, the error decreases for larger yaw angles. Comparing the drag and side force it can be noted that the improvements in drag prediction observed for the Spalart-Allmaras model is not reflected in the prediction of the side force. Indicating that, instead of accurately predicting the flow field, the superior drag prediction of the Spalart-Allmaras model might be explained by error cancellation.

Compared to RANS, the IDDES results in better predictions of the side force for all yaw angles except −10.0°, where all models perform similarly. Comparing the two near-wall models slightly smaller errors are obtained for the SA IDDES, especially for zero yaw.

4.2.3 Computational cost and numerical stability

Although the models ability to accurately predict the drag coefficient can be considered the most important aspect, properties such as computational cost and numerical stability must be considered. The costs are obviously dependent on the number of iterations the simulations are run. However, since all RANS models were run for the same number of iterations it is believed that a fair comparison can be done between these. Similarly both IDDES models were run for the same number of time steps, making them comparable. However, the comparison between RANS and IDDES is less straight forward and should be seen as a rough approximation of the increased cost of IDDES.

In table 4.4 the computational cost averaged over all yaw angles is shown for each model. Additionally the cost normalized to the DSL = 1.2 k-ε model is shown. The computational costs are almost identical for the k-ε and k-ω models. The Spalart-Allmaras model shows an improvement in the solver time. However the improvement is approximately half of what could be expected in an ideal case, were five equations are solved instead of six. For the IDDES models there is a 9% improvement in cost when using the Spalart-Allmaras near-wall model, comparable to the improvement from k-ε or k-ω to Spalart-Allmaras for the RANS models. Comparing the IDDES and RANS models the cost increases approximately five times, corresponding to five times more iterations (5 s simulated time, 1 ms time step, 10 inner iterations compared to 10000 iterations) being performed.

The stability of the solutions using RANS models were assessed by investigating the oscillations of C_D during the last 1000 iterations, which is the same interval as C_D was averaged over. In table 4.5 the oscillations are presented for the different RANS models, averaged over all yaw angles. The oscillations are defined as the

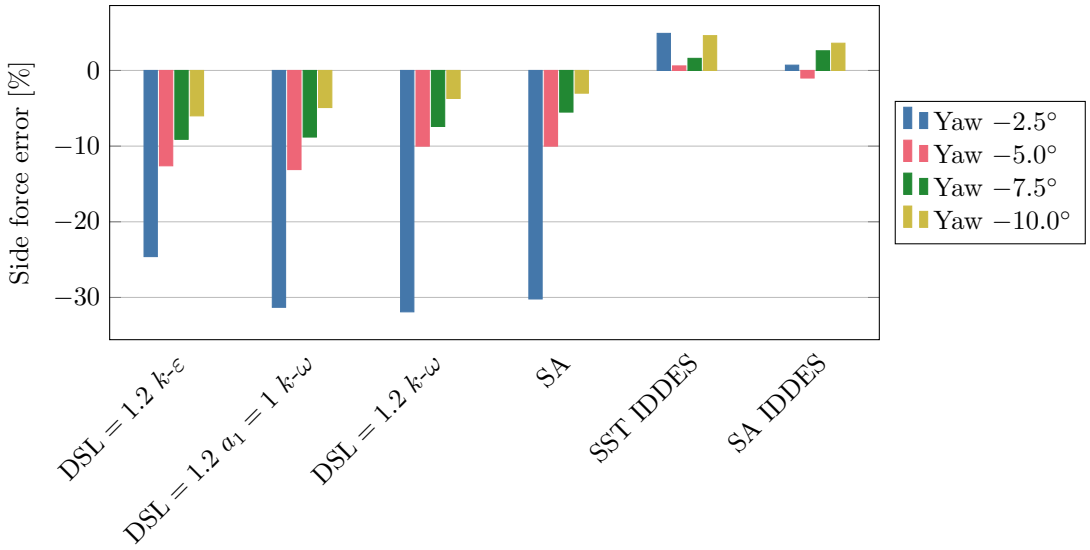

Figure 4.12: Side force error of the turbulence models compared to experimental data.

Table 4.4: Computational cost averaged over all yaw angles for the different turbulence models.

Turbulence model	Average cost [CPUh]	Normalized cost [−]
DSL = 1.2 k-ε	4638	1.00
DSL = 1.2 $a_1 = 1$ k-ω	4605	0.99
DSL = 1.2 k-ω	4613	0.99
SA	4306	0.93
SST IDDES	23308	5.03
SA IDDES	21192	4.57

Table 4.5: Oscillations of C_D during the final 1000 iterations for the RANS models averaged over all yaw angles.

Turbulence model	Average oscillation [counts]
DSL = 1.2 k-ε	0.3
DSL = 1.2 $a_1 = 1$ k-ω	2.1
DSL = 1.2 k-ω	23.1
SA	14.4

difference between the maximum and minimum value of C_D in the interval. The k-ε model results in the smallest oscillations and is the only model resulting in convergence within one drag count over 1000 iterations. Moreover, a large difference is obtained for the k-ω models with different a_1. A coefficient $a_1 = 1$ results in a tenth of the oscillations of $a_1 = 0.31$. Finally the Spalart-Allmaras model also results in large oscillations, although they are smaller than for the DSL = 1.2 k-ω model.

4.2.4 0.0° yaw

In order to better understand the drag prediction of the different models a more thorough analysis was performed, starting with the results obtained at zero yaw. In figure 4.13 the accumulation of ΔC_D along the truck compared to the DSL = 1.2 k-ε model is shown. Comparing the k-ε and k-ω models the k-ω models predicts more drag along the cab. Both k-ω models predicts more drag at the cab front and a lower pressure in the tractor-trailer gap than the k-ε model. These differences are larger for $a_1 = 0.31$ than for $a_1 = 1$. Furthermore both k-ω models predict a smaller drag penalty over the tractor-trailer gap than the k-ε model. Along the chassis and trailer the drag prediction is similar for all three k-ε and k-ω models, with a small difference being observed at the trailer wheels. Instead the larger drag predicted by the $a_1 = 0.31$ k-ω model, compared to the other k-ω and the k-ε model, is explained by the difference in base pressure on the trailer.

Investigating the performance of the Spalart-Allmaras model a 3% difference compared to the k-ε model is obtained at the front of the tractor, suggesting a larger stagnation region. Further downstream a small difference in the tractor-trailer gap pressure is noted, with the overall loss being similar to the k-ε model. The accumulation of drag along the trailer is similar to the other models. Similarly to the k-ω models a slightly smaller loss at the trailer wheels is predicted, compared to the k-ε model. Finally, it can be seen that the large drag predicted by the Spalart-Allmaras model is almost entirely explained by a low base pressure.

Comparing the IDDES models to the k-ε model slightly more drag is predicted at the front of the tractor, with the accumulated drag being slightly lower for the Spalart-Allmaras than for the SST k-ω near-wall model. In the trailer gap both the IDDES models predicts a lower pressure than the k-ε model and an overall smaller loss across the gap. Interestingly the accumulated ΔC_D profiles for the SST IDDES and DSL = 1.2 k-ω, which k-ω models are the same, are very similar at the tractor-trailer gap. Further downstream the IDDES models behave similar to the other models with the effect from the tractor rear wheel and mount being slightly different. The IDDES models both predict larger drag from the trailer wheels than the other models, with a sharp increase being observed right downstream the trailer wheel, which is caused by the mudflaps. Finally a small difference compared to k-ε is observed at the trailer base for both IDDES models.

Concluding that the most significant differences affecting the drag was observed at the trailer base this region is further investigated. In order to emphasize the influence of the base pressure on the drag coefficient the area of the trailer base and the total frontal area is compared. With the trailer base area being approximately 70% of the frontal area an increase of the pressure coefficient, C_p, of 0.1 at the base corresponds to a 0.07 (or 70 drag counts) increase of C_D, all other things being equal. Therefore, accurately predicting the base pressure is essential to accurately predicting the drag coefficient.

In figure 4.14 the pressure at the trailer base, mudflaps and wheels is shown for all turbulence models. Based on the investigation of accumulated ΔC_D in figure 4.13 it is expected that the average pressure over the base should be similar for the DSL = 1.2 k-ε, DSL = 1.2 $a_1 = 1$ k-ω and both IDDES models, with lower pressures being observed for the DSL = 1.2 k-ω and the Spalart-Allmaras models. Examining the base pressures in figure 4.14 this is confirmed. However it is noted that the pressure distribution on the base differs between the models. The k-ε and the DSL = 1.2 $a_1 = 1$ k-ω model both predicts similar pressure distributions, with the pressure being almost constant over the trailer base. The IDDES instead predicts a larger variation in the pressure,

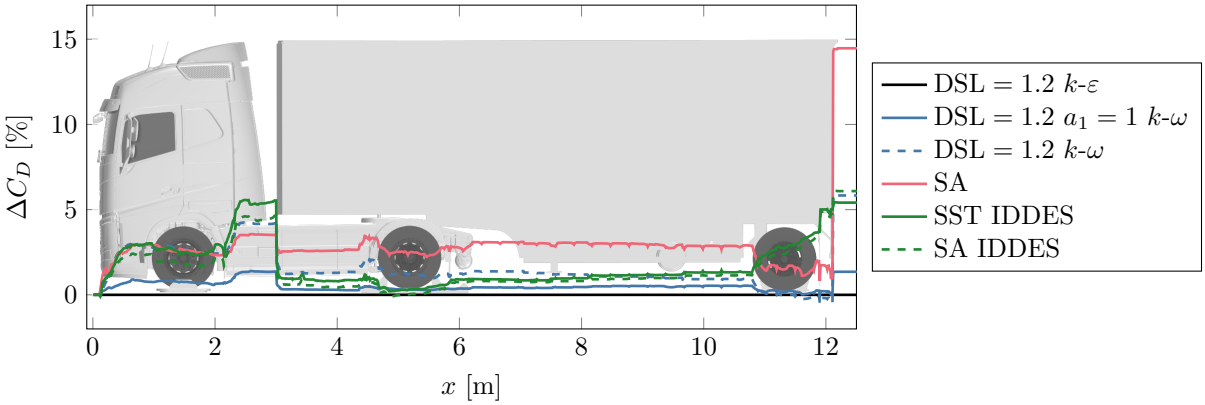

Figure 4.13: Accumulated ΔC_D of the different turbulence models at zero yaw. The baseline is the DSL = 1.2 k-ε model.

with a gradient mainly in the vertical direction. As observed for the ΔC_D the IDDES models captures the mudflaps differently to the RANS models.

The DSL = 1.2 k-ω and Spalart-Allmaras models both predict significantly lower base pressures than the other models, with the Spalart-Allmaras model predicting the lowest. For the Spalart-Allmaras model it can also be noted that, as opposed to the other RANS models, the base pressure is not symmetric around the centerline. This could be explained by the relatively large oscillations of the Spalart-Allmaras model observed in table 4.5.

In order to better understand the differences in trailer pressure the flow structures in the wake are examined. Figure 4.15 shows the velocity in the z-direction and the pressure coefficient, both combined with streamlines, along the centerline of the wake. The k-ε (figure 4.15a and 4.15b) and the DSL = 1.2 $a_1 = 1$ k-ω (figure 4.15c and 4.15d) models both predict similar velocity and pressure fields. However a difference is noted around the trailer wheels, where the k-ε model is predicting a positive velocity in the x-direction between the wheels and the k-ω model predicts a negative velocity. Examining the DSL = 1.2 k-ω model (figure 4.15e and 4.15f) a significantly larger z-velocity and corresponding lower pressure is noted at the trailer base. The Spalart-Allmaras model (figure 4.15g and 4.15h) predicts an even larger z-velocity and a lower pressure. Furthermore it is noted that both k-ω models and the Spalart-Allmaras model predict similar velocity fields at the trailer wheels. Investigating the unsteady IDDES models (figure 4.15i to 4.15l) significant differences to the RANS models are noted at the trailer base. When examining the base pressure (figure 4.14) it was noted that the RANS models predicted a more homogeneous pressure over the rear trailer surface, whereas the IDDES models predicted a gradient, most clearly in the z-direction. This is explained by the IDDES models predicting a strong low-pressure-core vortex at the lower part of the trailer base being created by the underbody flow. Both IDDES models resulted in more flow between the trailer wheels, altering the wake properties. This underbody flow also explains why the IDDES models predicted more drag from the trailer wheels than the RANS models.

When comparing the underbody flow of the different models a significant difference between the RANS and IDDES models was observed for how the outwash coming of the tractor wheels interacted with the trailer wheels and wake. In general the wheel wakes of the RANS models extended further outwards, isolating the trailer wheels and underbody from the high-velocity air of the freestream. This allowed a large recirculation region behind the trailer with negative x-velocity between the trailer wheels. The IDDES models predicted less outwash and wheel wakes that collapsed upstream the trailer wheels. This allowed high energy air entering under the trailer resulting in more drag from the trailer wheels as well as an altered trailer wake.

To further understand the differences in the wakes the local drag (figure 4.16) and the turbulent kinetic energy (figure 4.17) is investigated. Just as for the base pressure the k-ε and DSL = 1.2 $a_1 = 1$ k-ω models predicts very similar results. Comparing the local drag at the centerline one notable exception is though the slightly larger magnitude of local drag predicted at the ground by the k-ω model, indicating a larger velocity magnitude of the recirculating flow. Furthermore a minor difference can be seen at the trailer mudflaps, where the k-ε model seems to capture the wheel and mudflap drag slightly more than the k-ω model does. These observations

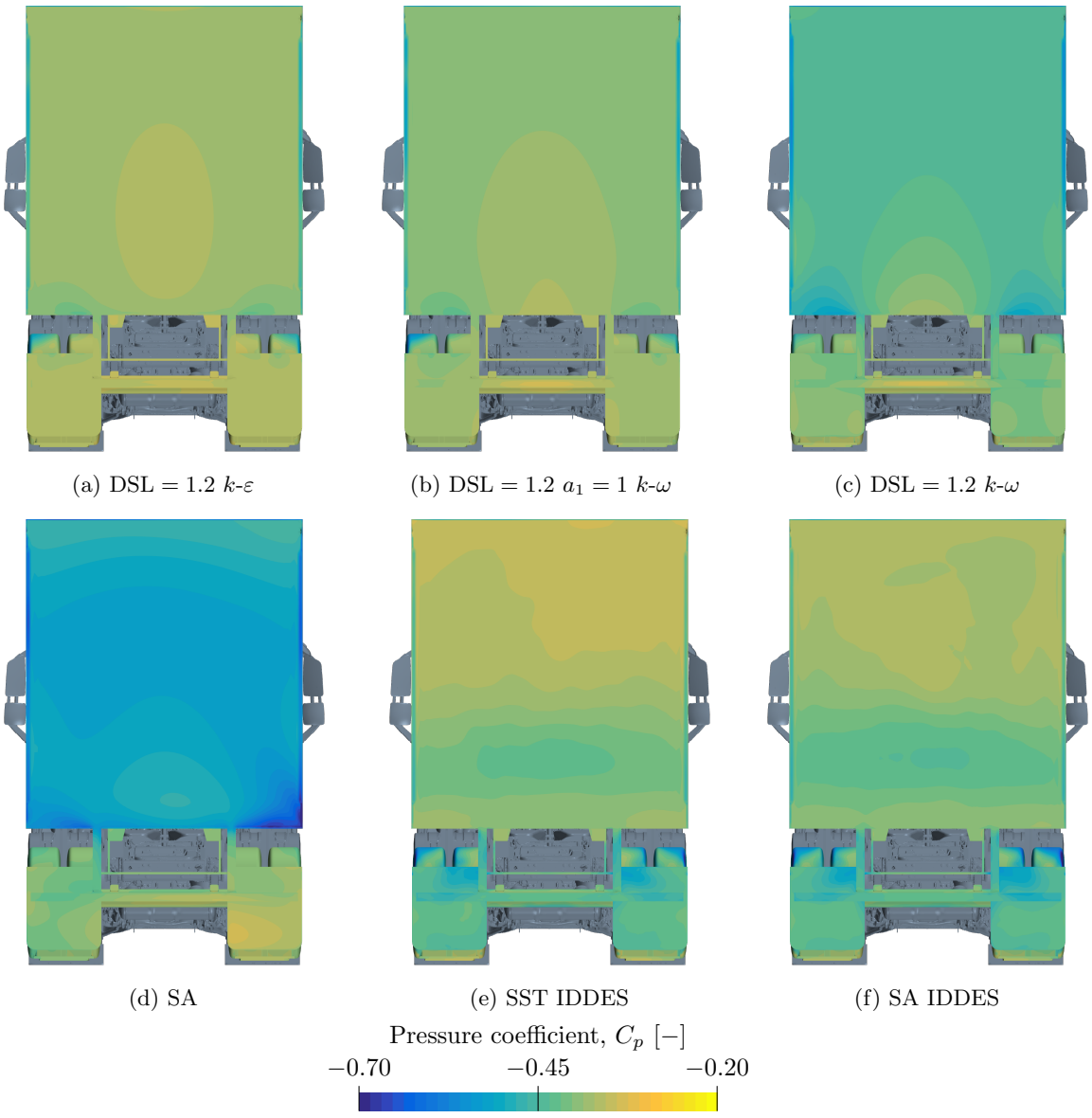

(a) DSL = 1.2 k-ε (b) DSL = 1.2 $a_1 = 1$ k-ω (c) DSL = 1.2 k-ω

(d) SA (e) SST IDDES (f) SA IDDES

Figure 4.14: Pressure coefficient at the base of the trailer for zero yaw.

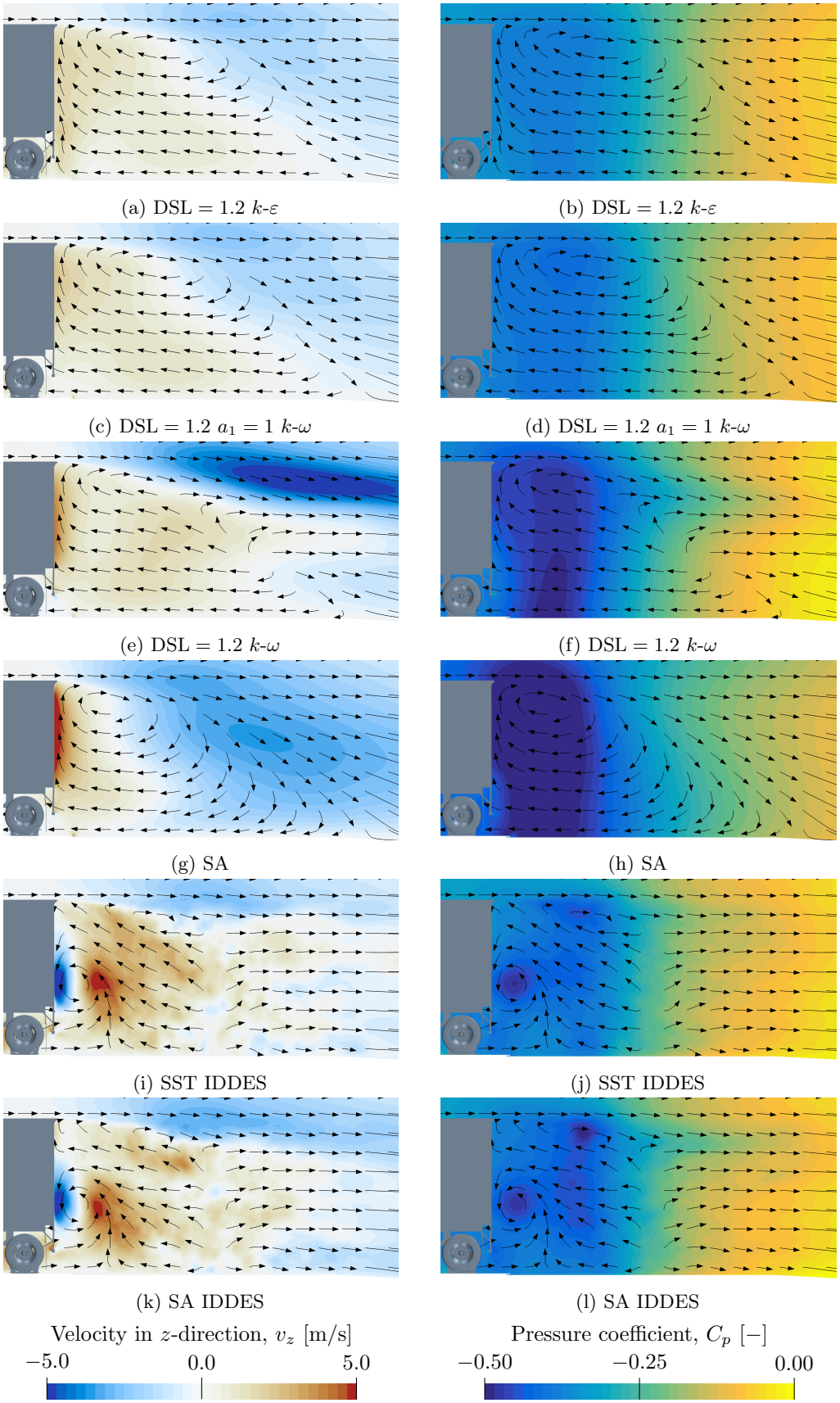

(a) DSL = 1.2 k-ε (b) DSL = 1.2 k-ε

(c) DSL = 1.2 $a_1 = 1$ k-ω (d) DSL = 1.2 $a_1 = 1$ k-ω

(e) DSL = 1.2 k-ω (f) DSL = 1.2 k-ω

(g) SA (h) SA

(i) SST IDDES (j) SST IDDES

(k) SA IDDES (l) SA IDDES

Figure 4.15: Velocity in the z-direction and pressure coefficient, both with streamlines, along the centerline of the wake at zero yaw.

are consistent with the observations in figure 4.15, were a difference in the flow direction between the trailer wheels was observed.

Comparing the local drag of the DSL = 1.2 k-ω (figure 4.16e and 4.16f) and Spalart-Allmaras (figure 4.16g and 4.16h) models, which predicted the lowest base pressures, with the k-ε and DSL = 1.2 $a_1 = 1$ k-ω model it can be seen that the lower base pressures seem to corresponds to shorter, more compact wakes. For the DSL = 1.2 k-ω model there is also a significant difference in the recirculation close to the ground, compared to the remaining k-ω model. The larger drag predicted by both the DSL = 1.2 k-ω and the Spalart-Allmaras model is partly explained by the larger shear layers, obtained both above and at the sides of the trailer, especially for the Spalart-Allmaras model. Analyzing the turbulent kinetic energy for both models (figure 4.17c and 4.17d) it can be seen that the shorter wakes corresponds to more turbulent kinetic energy being predicted by the models. More turbulent kinetic energy increases the turbulent mixing, hence reducing the size of the recirculation region behind the trailer. For the DSL=1.2 k-ω model slightly more turbulent kinetic energy is predicted in the wake than for the k-ε and the DSL = 1.2 $a_1 = 1$ k-ω models. Furthermore there is an asymmetry in the turbulent kinetic energy field, where more energy is predicted at the left side. This asymmetry can also be seen in the local drag, where the larger amount of turbulent kinetic energy on the left sides results in slightly larger losses in the shear layer at the left side of the trailer. The Spalart-Allmaras model predicts the most turbulent kinetic energy, which is reflected in the wake being the smallest, with the largest losses in the shear layers. Notable for the Spalart-Allmaras model is that a larger local drag is predicted along the sides of the trailer, right upstream the base, than for the other RANS models. This is explained by the Spalart-Allmaras model predicting slightly different flow in the a-pillar and rear-view mirror region. Further downstream this affects the flow around the tractor-trailer gap which leads to a larger separated region all along the trailer for the Spalart-Allmaras model.

For the IDDES models (figure 4.16i-4.16l) the local drag is similar for the two different near-wall models. Similarly to the DSL = 1.2 k-ω and Spalart-Allmaras models the IDDES models predicts smaller wakes, which is explained by the prediction of more turbulent kinetic energy (figure 4.17e and 4.17f). Although predicting wakes of similar sizes as the DSL = 1.2 $a_1 = 1$ k-ω and the Spalart-Allmaras models the IDDES models predicts smaller losses in the shear layers. This is to be expected since the accumulated drag showed that the main difference between the IDDES and RANS was found along the truck rather than at the trailer base. Furthermore the difference in underbody flow between the IDDES and RANS models can once again be seen. Examining the local drag the losses due to the vortex coming of the underbody can be seen.

4.2.5 -5.0° yaw

In order to better understand why all turbulence models resulted in better correlation to the wind tunnel for larger yaw angles the flow fields of the $-5.0°$ cases will be analyzed. In figure 4.18 the accumulated ΔC_D is shown for the different turbulence models, with the baseline being the k-ε model. Similarly to zero yaw the k-ε and the $a_1 = 1$ k-ω model predicts very similar results, with the same differences being observed for both yaw angles. The $a_1 = 1$ k-ω model predicts slightly less than 1% more drag than the k-ε model at the tractor front as well as a lower pressure in the tractor-trailer gap for both yaw angles. The k-ω model with $a_1 = 0.31$ predicts a larger drag than the k-ε model at the front of the tractor and a lower pressure, with an overall smaller loss, in the tractor-trailer gap, similarly to at zero yaw. Although for $-5.0°$ yaw the difference to the k-ε model is slightly smaller. The difference between the $a_1 = 0.31$ k-ω and the k-ε model obtained at the tractor-trailer gap of approximately 1% remains constant along the trailer. However, a larger base pressure results in the overall drag being very similar to the k-ε model, and therefore also to the other k-ω model. At zero yaw the Spalart-Allmaras model showed a similar behavior to the $a_1 = 0.31$ k-ω model along the cab. At $-5.0°$ yaw the Spalart-Allmaras model is instead similar to the $a_1 = 1$ k-ω model along the cab. Further downstream the Spalart-Allmaras model accumulates slightly more drag along the trailer than the k-ε model. Similarly to zero yaw, a significantly lower base pressure is predicted for the Spalart-Allmaras model than for the other models. Investigating the IDDES models similarities to the zero yaw case are once again noted. Both IDDES models predicts a larger drag at the front of the tractor than the k-ε model. Furthermore, a lower pressure is obtained in the tractor-trailer gap. Both IDDES models results in the tractor rear wheels being captured differently than for the RANS models, comparable to the effect noted for the trailer wheels at zero yaw. Downstream the tractor rear wheels, along the trailer, no major differences compared to the k-ε model are obtained. As for zero yaw a slightly larger drag increase from the trailer mudflaps is obtained for the IDDES models than for the RANS models. Comparing the different near-wall models of the IDDES models the Spalart-Allmaras predicts lower drag at the tractor front. This difference remains along the truck until

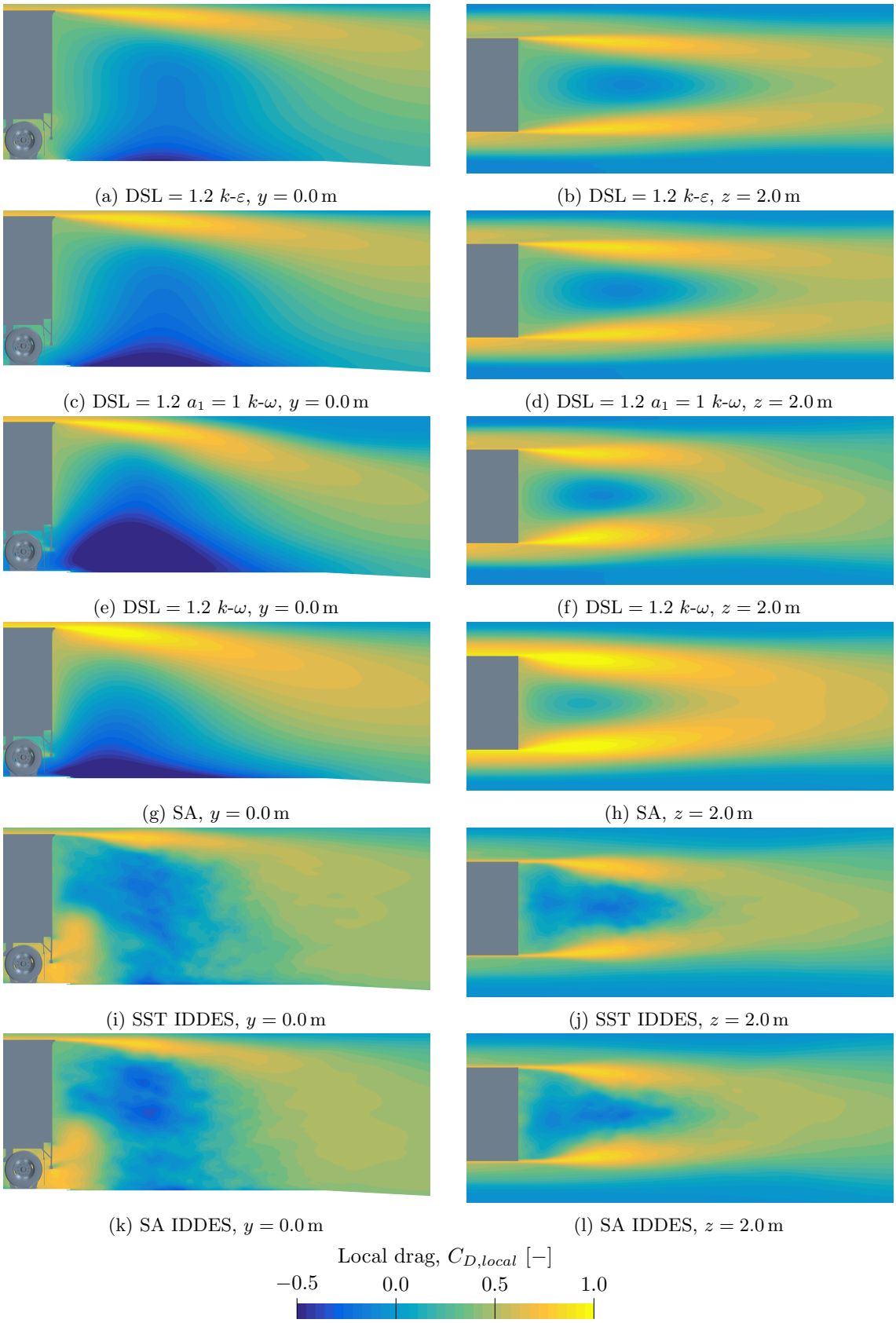

(a) DSL = 1.2 k-ε, $y = 0.0\,\mathrm{m}$

(b) DSL = 1.2 k-ε, $z = 2.0\,\mathrm{m}$

(c) DSL = 1.2 $a_1 = 1$ k-ω, $y = 0.0\,\mathrm{m}$

(d) DSL = 1.2 $a_1 = 1$ k-ω, $z = 2.0\,\mathrm{m}$

(e) DSL = 1.2 k-ω, $y = 0.0\,\mathrm{m}$

(f) DSL = 1.2 k-ω, $z = 2.0\,\mathrm{m}$

(g) SA, $y = 0.0\,\mathrm{m}$

(h) SA, $z = 2.0\,\mathrm{m}$

(i) SST IDDES, $y = 0.0\,\mathrm{m}$

(j) SST IDDES, $z = 2.0\,\mathrm{m}$

(k) SA IDDES, $y = 0.0\,\mathrm{m}$

(l) SA IDDES, $z = 2.0\,\mathrm{m}$

Figure 4.16: Local drag in the wake for zero yaw.

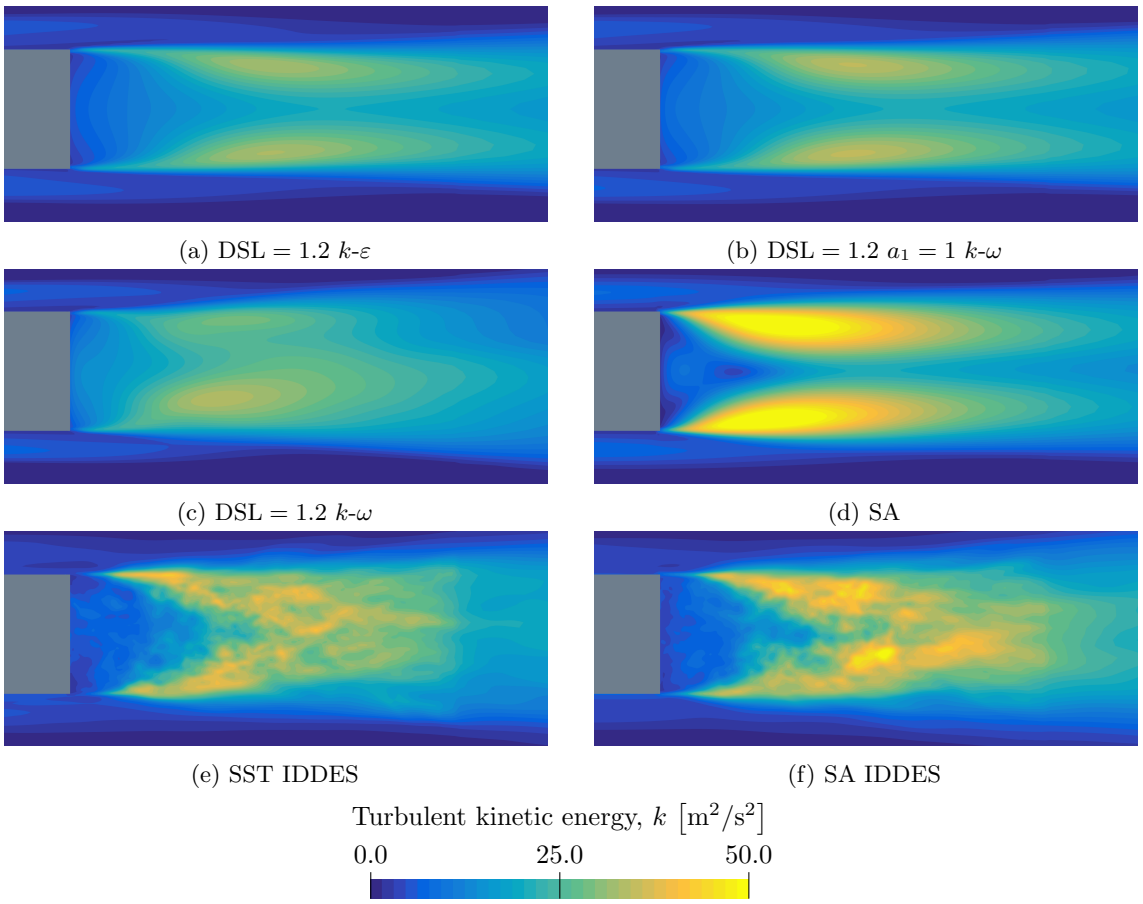

(a) DSL = 1.2 k-ε

(b) DSL = 1.2 $a_1 = 1$ k-ω

(c) DSL = 1.2 k-ω

(d) SA

(e) SST IDDES

(f) SA IDDES

Figure 4.17: Turbulent kinetic energy in the wake for zero yaw illustrated in the plane $z = 2.0\,\mathrm{m}$.

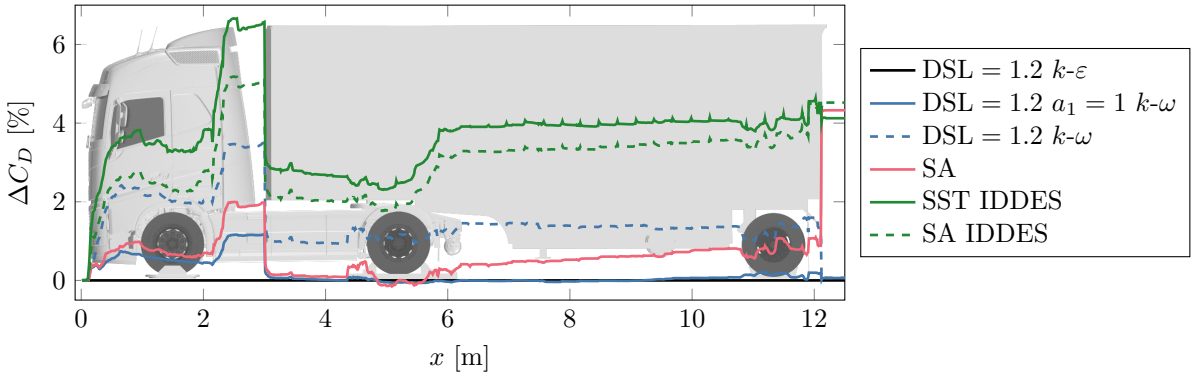

Figure 4.18: Accumulated ΔC_D of the different turbulence models at $-5.0°$ yaw. The baseline is the DSL = 1.2 k-ε model.

downstream the trailer wheels, where a difference is obtained at the mudflaps, resulting in approximately the same drag coefficient for both near-wall models.

Comparing the base pressures at the trailer (figure 4.19) it can be seen that the differences between the models are smaller than at zero yaw (figure 4.14). As expected from the accumulated ΔC_D the k-ε and the DSL = 1.2 $a_1 = 1$ k-ω models predict similar base pressure. Although the k-ε model seem to predict a different underbody flow, with a significantly larger pressure being observed at the right mudflap and at the trailer wheel axis. The difference in base pressure when comparing the DSL = 1.2 k-ω model to both the k-ε and the remaining k-ω model can be explained by the region of lower pressure, seen towards the bottom left corner of the trailer base, being smaller for the DSL = 1.2 k-ω model. The Spalart-Allmaras model predicts lower pressures at the bottom and left part of the trailer compared to the other RANS models, indicating a different flow under the trailer. However, the pressures at the tires and mudflaps are similar to the DSL = 1.2 k-ω. Studying the results from the IDDES models a less homogeneous pressure field is obtained at the trailer base, especially for the SST IDDES. High-pressure regions are predicted at the top corners, in particularly at the windward (right) side. At the bottom half of the trailer a low-pressure region is obtained, resulting in approximately the same average base pressure as the RANS models and hence similar drag. Except for the k-ε model the pressures at the wheels and mudflaps are similar for the RANS and IDDES models, unlike the pressures predicted at zero yaw.

Similarly to for zero yaw a better understanding of the base pressure can be obtained by examining the flow structures in the wake. In figure 4.20 the velocity component in the z-direction is showed together with streamlines along the centerline of the truck. Note that because of the non-zero yaw angle this is no longer a symmetry plane. However it is still chosen to present the flow field in this view since some important flow features are highlighted. Compared to zero yaw it is noted that all models predicts a positive x-velocity between the trailer wheels, resulting in a vortex at the lower part of the trailer base for all cases. This could be part of the explanation of why all models perform better, and more similar, at yaw angles of $-5.0°$ or larger. At small yaw angles it was found that the difference in the outwash coming of the front of the tractor and the tractor wheel wakes significantly affected the flow under the trailer and in the wake. At larger yaw angles more of these flow features will be forced in under the trailer at the windward side. Examining all yaw angles it was found that an angle of $-5.0°$ or larger was enough for all models predicting the wakes collapsing upstream the trailer wheels. This resulted in high-velocity air below the trailer and between the trailer wheels, making the trailer wakes more similar and reducing the difference in drag prediction.

Comparing the different models the k-ε and both k-ω models all predict similar fields. For the DSL = 1.2 k-ω model a slightly higher base pressure was noted compared to the k-ε and remaining k-ω models, with the difference being a smaller low-pressure region close to the bottom of the base. Comparing the region of negative z-velocity between the k-ε and k-ω models (figure 4.20a-4.20c) it is noted that it is smaller for the DSL = 1.2 k-ω, implying a higher pressure at the surface. Similarly to zero yaw the lowest base pressure was obtained for the Spalart-Allmaras model, although the difference to the other models were significantly smaller at $-5.0°$ yaw. Examining the z-velocity (figure 4.20d) it is observed that this is, just as for zero yaw, explained by large velocities in the recirculation next to the surface. Comparing the different near-wall models of the IDDES (figure 4.20e and 4.20f) a large difference is initially noted, where the SA IDDES predicts higher z-velocities in the recirculation region. After further investigations it was found that both models predicted a similar region,

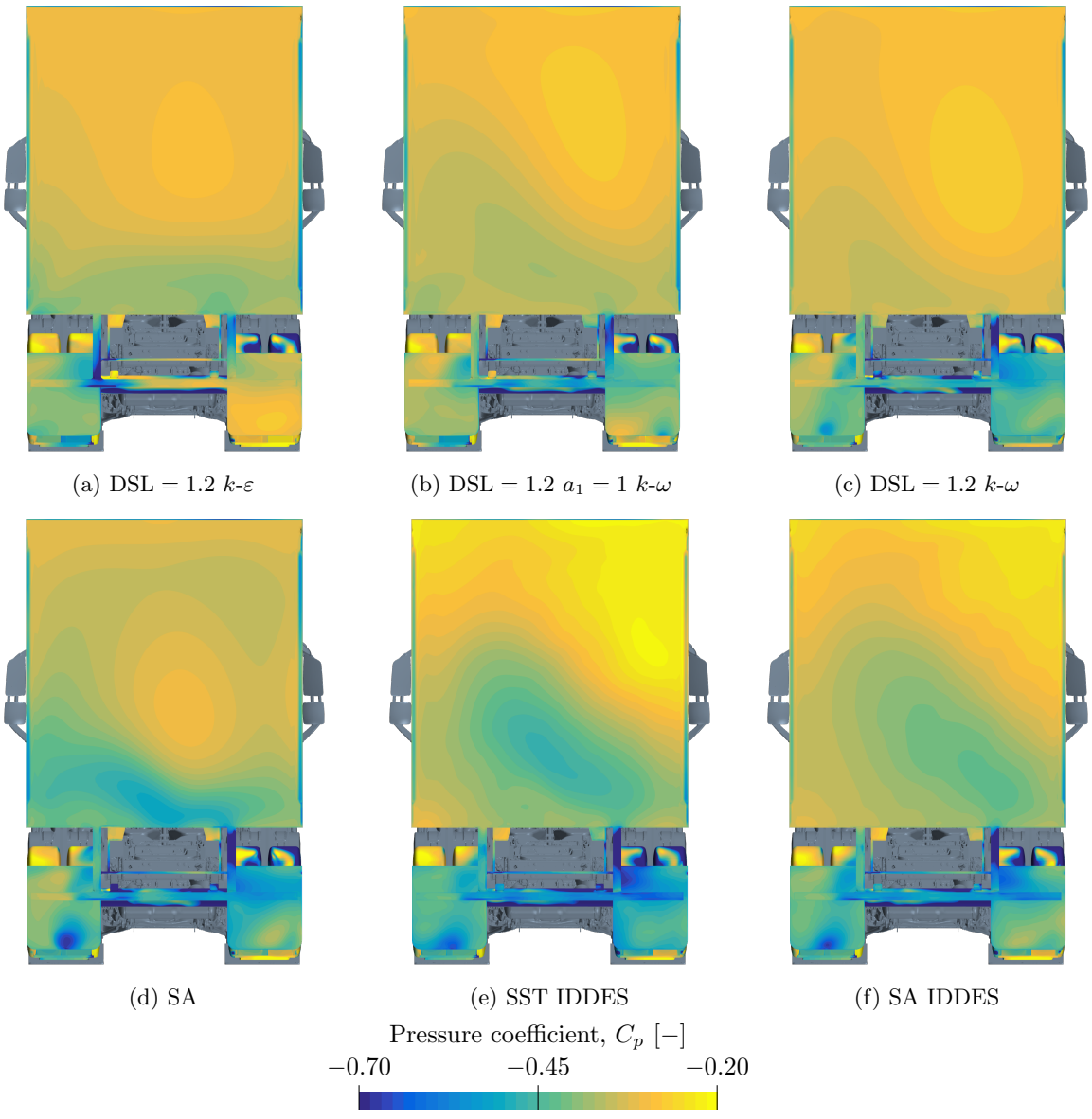

(a) DSL = 1.2 k-ε (b) DSL = 1.2 $a_1 = 1$ k-ω (c) DSL = 1.2 k-ω

(d) SA (e) SST IDDES (f) SA IDDES

Figure 4.19: Pressure coefficient at the base of the trailer for −5.0° yaw.

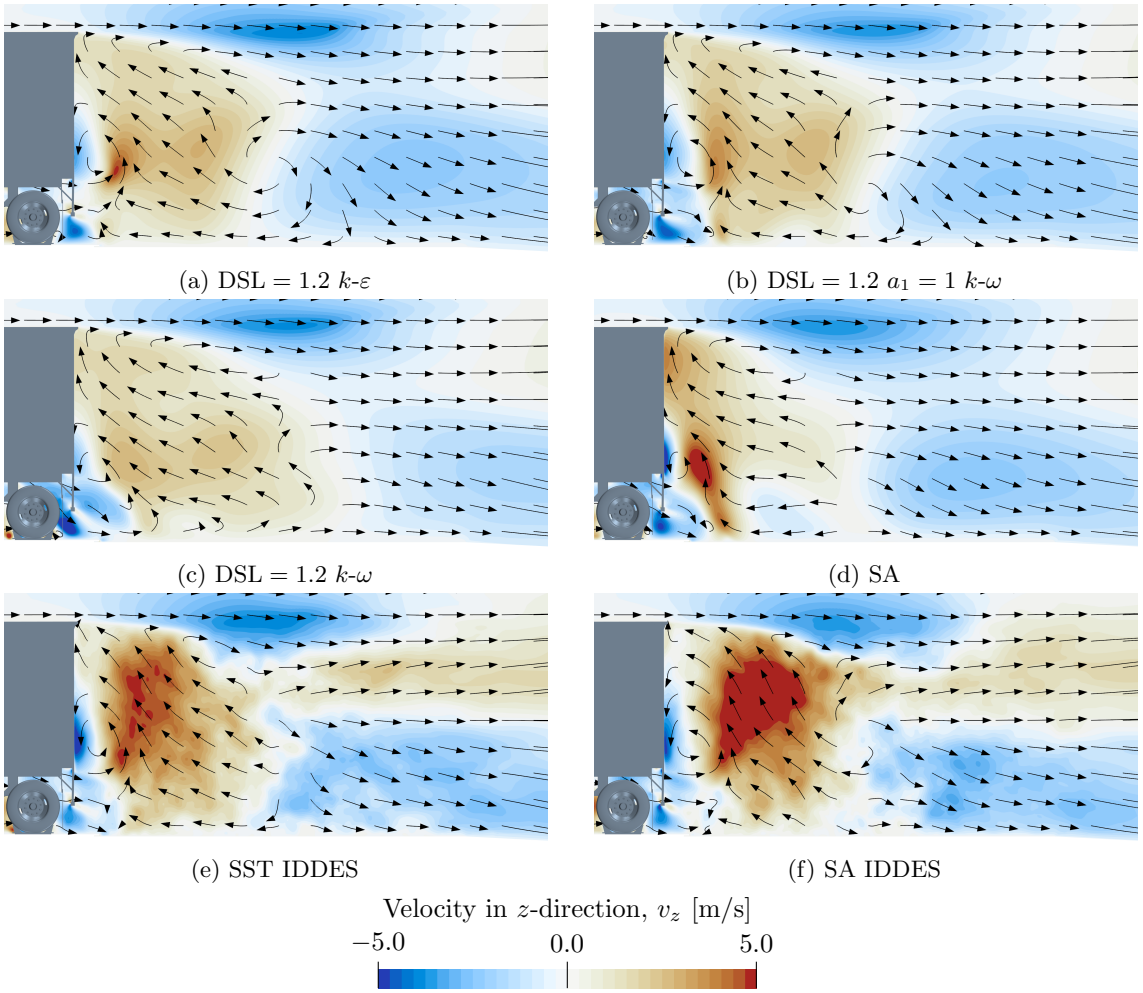

Figure 4.20: Velocity in the z-direction and streamlines along the centerline of the wake at $-5.0°$ yaw.

although with a slight offset in y-location, which exposes one of the drawbacks of using a symmetry plane of the truck for a case with a non-zero yaw angle. When examining the base pressures it was found that the IDDES models predicted a higher pressure towards the top and a lower pressure towards the bottom of the trailer base. Examining the velocity it can be seen that the high-pressure region is partly explained by a z-velocity close to zero. The lower pressure towards the bottom is explained by the velocity magnitude in the underbody vortex being larger.

Figure 4.21 shows the local drag and the turbulent kinetic energy in the wake of the trailer at $z = 2.0\,\text{m}$. Comparing the local drag to the results at zero yaw all models predicts more similar wakes at $-5.0°$ yaw. Similarly to zero yaw the k-ε and k-ω models predicts longer recirculation regions, however the difference to Spalart-Allmaras and IDDES are smaller at $-5.0°$ yaw. Examining the turbulent kinetic energy the shorter wakes are once again explained by more turbulent kinetic energy being predicted, resulting in more turbulent mixing. Continuing the comparison to zero yaw the shear layers are predicted more similarly at $-5.0°$. Studying the flow further upstream one explanation to this could be that the added yaw isolates the complex flow features around the cab from the trailer wake. When examining the local drag at zero yaw it was found that some models resulted in wakes from the rear-view mirrors that remained along the trailer, reaching the trailer base and altering the base shear layers. For $-5.0°$ yaw it can be seen that the flow along the sides of the trailer, directly upstream the trailer base, is similar for all models. This can be explained by the mirror wakes, or similar flow features originating from the cab, either reattaching to the trailer side or vanishing as a part of a much larger wake on the wind and leeward side, respectively.

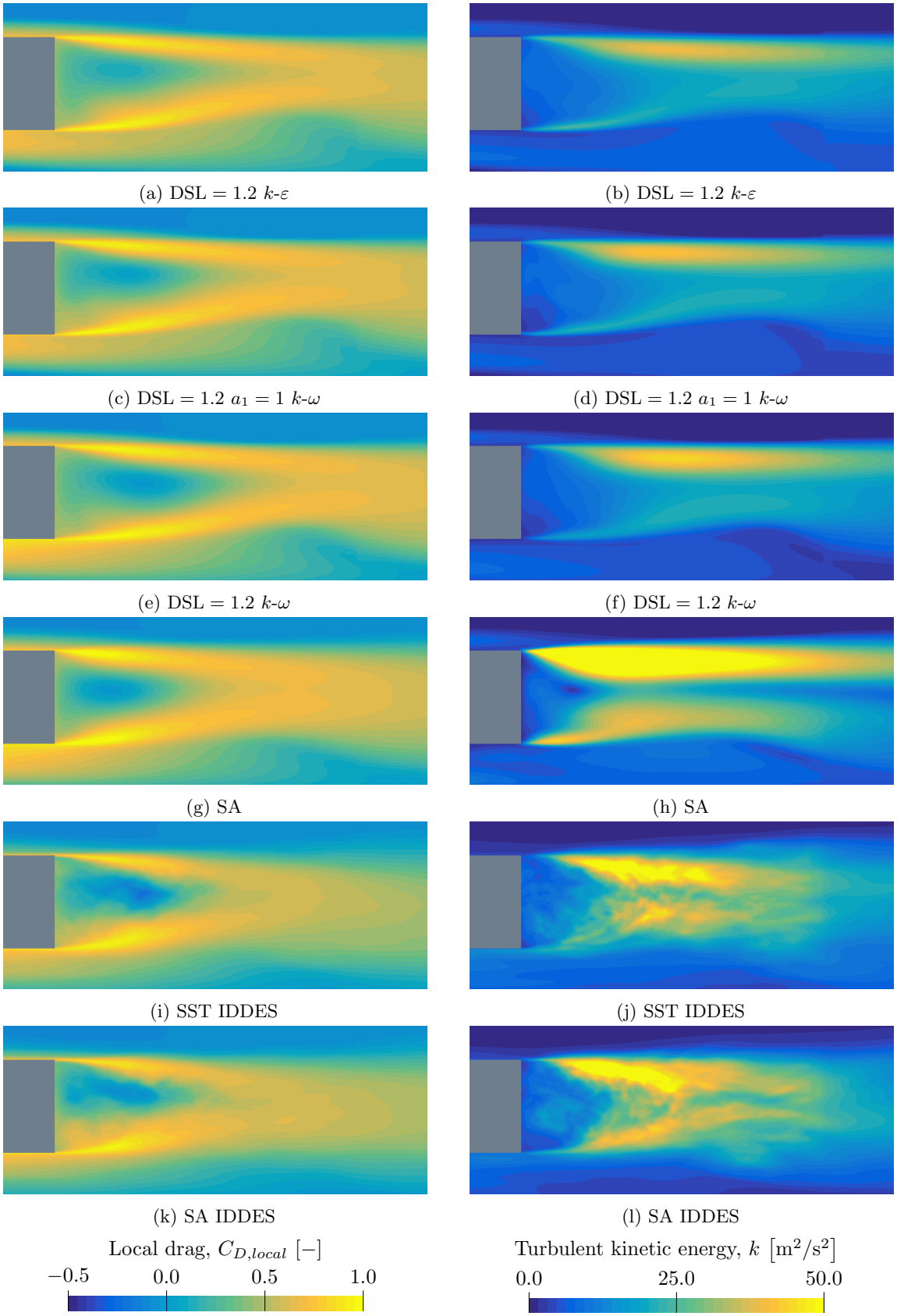

(a) DSL = 1.2 k-ε (b) DSL = 1.2 k-ε

(c) DSL = 1.2 $a_1 = 1$ k-ω (d) DSL = 1.2 $a_1 = 1$ k-ω

(e) DSL = 1.2 k-ω (f) DSL = 1.2 k-ω

(g) SA (h) SA

(i) SST IDDES (j) SST IDDES

(k) SA IDDES (l) SA IDDES

Figure 4.21: Local drag and turbulent kinetic energy in the wake for $-5.0°$ yaw shown in the plane $z = 2.0\,\mathrm{m}$.

4.3 Conclusions

In this section the performance of four RANS and two IDDES models was evaluated and compared to wind tunnel measurements, with the main focus being the drag prediction. It was found that the correlation was heavily dependent on the yaw angle, with the larger yaw angles resulting in smaller errors. Comparing the RANS models similar results were obtained for the k-ε and both k-ω models. Among these the DSL = 1.2 k-ε and the DSL = 1.2 $a_1 = 1$ k-ω models performed very similar, whereas the DSL = 1.2 k-ω performed slightly better for small yaw angles. Additionally the Spalart-Allmaras model resulted in the smallest overall error, both among the RANS and the IDDES models. However, examining quantities, such as the side force, and the flow fields it is believed that the performance of the Spalart-Allmaras model is explained to be error cancellation rather than an actual more realistic prediction of the flow. Comparing the IDDES models to the RANS models it was found that the prediction error of C_D is approximately half compared to the k-ε and k-ω models. No significant difference was found between the different IDDES near-wall models.

Furthermore, it was found that the differences between the models could mainly be explained by the difference in trailer wake structures. It was found that the turbulence models significantly altered large flow features, such as wake length and recirculation pattern. For zero yaw large differences in the underbody flow was found, especially between the RANS and the IDDES models, which contributed to the wake differences. For $-5.0°$ yaw the underbody differences were smaller, explaining part of the smaller spread in predicted drag between the models.

As for recommendations on which turbulence model to use in the standardized CFD process for steady-state simulations this study shows that the two best models are the DSL = 1.2 k-ε or the DSL = 1.2 $a_1 = 1$ k-ω models. A similar accuracy can also be obtained from the DSL = 1.2 k-ω, however the larger oscillations in C_D makes the remaining k-ω model a better alternative. Although very similar performance was obtained for the DSL = 1.2 k-ε and DSL = 1.2 k-ω models it is believed that the k-ω model might be the better model for implementing in the standardized CFD process. This is motivated by observations, both in this thesis and other projects at Volvo, that the DSL = 1.2 k-ε sometimes locks into bistable states of the solution. This problem was not experienced using the DSL = 1.2 k-ω model.

In terms of a recommended IDDES model no major difference between the two near-wall models could be found. There is a small improvement in computational cost if using the Spalart-Allmaras model. On the other hand using the k-ω model might prove beneficial since a near-wall model similar to the recommended RANS model might simplify other aspects, shared by both the RANS and IDDES simulations. As an example a near-wall model similar to the RANS model might result in mesh changes affecting both the RANS and IDDES methods similarly.

5 Wind tunnel modelling

As an attempt to improve the accuracy of the simulations the modelling of the wind tunnel environment will be investigated. These investigations include both the geometrical accuracy of the wind tunnel CAD model as well as the boundary conditions used in the simulations. Different methods have been used to simulate wind tunnel flows. One method is to include the full wind tunnel circuit, as investigated by Nayani et al. [27]. It was however concluded that this method presents additional challenges, for example modelling the fan and heat exchangers. Additionally, this method requires detailed knowledge about the wind tunnel geometry, not available to customers of the NRC. Many investigations have instead been performed were the return-leg of the wind tunnel is excluded, using a number of different approaches. Martini et al. [28] investigated external aerodynamics and cooling flow in the NRC wind tunnel by modelling the wind tunnel with converging nozzle, test section and diffuser. Ross et al. [29] modelled the NRC wind tunnel as a constant cross section based on the test section. This method provides the benefit that boundary conditions, such as turbulent intensity, applied at the inlet can be directly related to values measured in the test section. However, Söderblom et al. [30] found that the high blockage of a truck results in the fluid region displaced in front of the truck interacting with the flow through the converging nozzle, altering the flow field, motivating the inclusion of the converging nozzle. Finally, Garry et al. [24] found that the diffuser of a wind tunnel can affect the measured drag greatly. Based on the study it was recommended that the distance between the vehicle base and the wind tunnel diffuser should preferably be larger than $4A^{1/2}$, where A is the base area, and never smaller than $2A^{1/2}$. For the trailer used in this thesis the base area is approximately $7.4\,\mathrm{m}^2$, resulting in the recommendations 10.9 m and 5.4 m, respectively. In the wind tunnel test the distance between the trailer base and the diffuser was 7.5 m. Based on these results it was concluded that the best strategy for this thesis is to include both the converging nozzle and the diffuser.

5.1 Converging nozzle

As discussed in section 4.1.2 the NRC does not supply customers with the geometrical measurements of the wind tunnel, except for the test section. However, some of the main design parameters, the contraction ratio (6.0) and diffuser cone angle (3.0°) have been published. [24] Provided that a similar approach to the one above, where the wind tunnel is modelled from the start of the converging nozzle to the end of the diffuser (with extensions in both ends) is used, the only major geometrical unknown is the converging nozzle. In an article describing the different systems of the wind tunnel a cross section of the converging nozzle, test section and diffuser is presented along with the simulated velocity distribution along the centerline 1 m above the wind tunnel floor. [31] This cross section was used to construct a more accurate contraction. However, since the wind tunnel transitions from circular to rectangular along the converging nozzle, some uncertainties remain. The cross sections of the old and new converging nozzles are shown in figure 5.1.

In order to compare the new wind tunnel geometry to published data simulations were performed using an empty wind tunnel. These simulations were performed using the steady state DSL = 1.2 k-ε model and a mesh strategy similar to the one used when having a truck in the tunnel. The resulting mesh consisted of approximately 6.5 million cells. Based on the data found in the literature two comparisons can be performed.

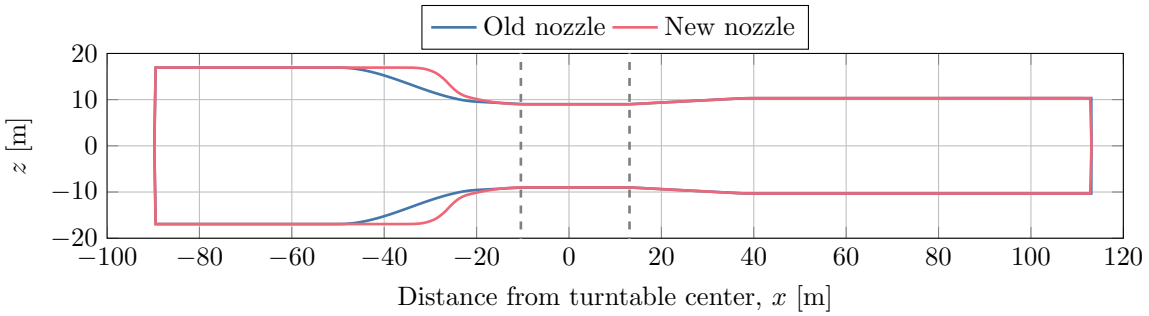

Figure 5.1: Cross section of the wind tunnel model at $y = 0.0\,\mathrm{m}$. The dashed lines marks the start and end of the test section.

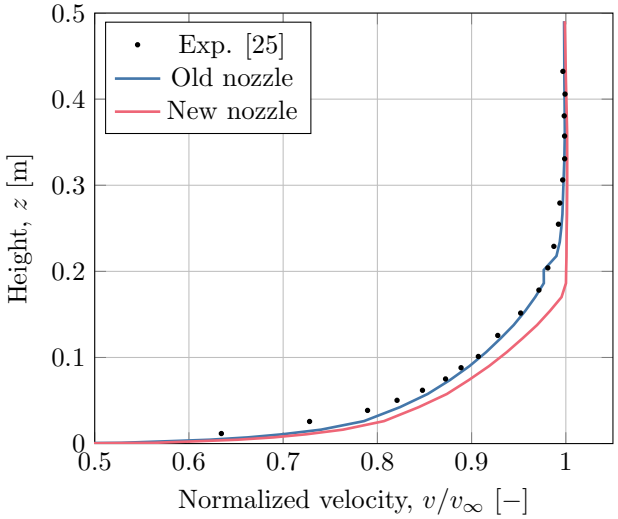

Figure 5.2: Boundary layer at the leading edge of the turntable for the empty NRC wind tunnel, comparison between simulations and experimental data by [25].

Firstly the boundary layer at the turntable leading edge is investigated and compared to experimental data by Larose and Tanguay [25]. Secondly the velocity 1 m above the ground is compared to CFD simulations by Nguyen et al. [31].

The wind tunnel is modelled using a no-slip conditions at the walls in the test section and a slip condition at the walls of the diffuser and extensions. The walls of the converging nozzle combines both types of walls, with the transition point being moved to achieve the desired boundary layer. This transition point was initially set using flat plate boundary layer theory and later fine-tuned using simulations. In figure 5.2 the resulting boundary layer profiles at the leading edge of the turntable is shown and compared to experimental data. Both nozzles results in similar boundary layers, however the old nozzle better correlates to the experimental data. In addition to the boundary layer profile Larose and Tanguay [25] state that the displacement thickness, δ^*, defined as

$$\delta^* = \frac{1}{v_\infty} \int_0^\delta (v_\infty - v)\, dz, \tag{5.1}$$

is 25 mm at the leading edge of the turntable. The displacement thickness were 25.4 mm and 20.4 mm for the old and new nozzle, respectively.

Investigating the velocity profile 1 m above the ground (figure 5.3) the new nozzle provides the best correlation to the NRC data. However, both nozzles results in nearly identical velocity distributions from the beginning of the test section and further downstream. Comparing the velocities in the end of the test section the NRC results suggest that the actual test section is shorter than in the model used for this thesis. Furthermore the actual diffuser angle seem to be smaller than 3.0° (which was obtained from [24]) since the simulation by Nguyen et al. [31] (labeled NRC) shows a slower velocity decrease than the simulations performed in this thesis.

In addition to investigating the different nozzles using the empty wind tunnel simulations were performed using the detailed truck. The results of these simulations shows no significant difference in terms of the predicted drag coefficient, as shown in table 5.1. For a yaw sweep using the DSL = 1.2 k-ε model the largest difference noted between the nozzles are 0.3%. Combining the results from the boundary layer and velocity profile comparisons the new nozzle will be used for the coming simulations. The major reason behind this is that some of the investigations included non-uniform velocity profiles at the inlet. Hence it is believed that it was more important to accurately replicate the velocity distribution than the boundary layer.

5.2 Velocity distribution

When evaluating the results from the investigation of turbulence models one major concern was the poor prediction of drag at small yaw angles. Furthermore investigations not presented in this thesis noted that the

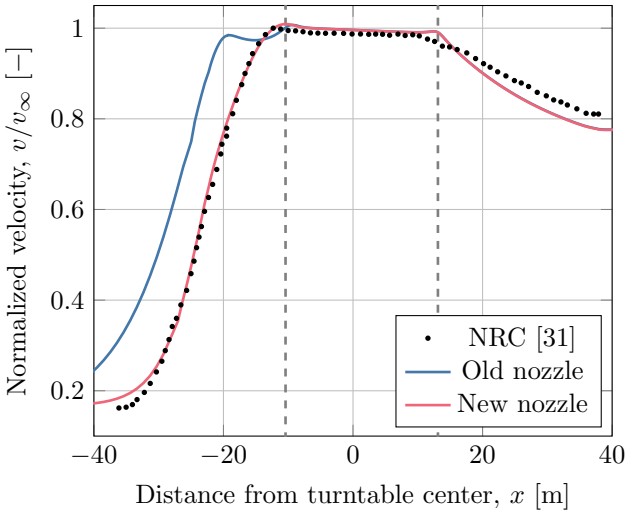

Figure 5.3: Velocity profile along the centerline of the tunnel 1 m above the test section floor. The data labeled NRC was recreated from [31].

Table 5.1: Normalized C_D for the old and new converging nozzle simulated with the DSL = 1.2 k-ε model for different yaw angles.

Yaw angle [°]	Old nozzle	New nozzle	Δ [%]
0.0	0.869	0.868	0.0
−2.5	0.914	0.912	−0.2
−5.0	0.973	0.970	−0.3
−7.5	0.992	0.989	−0.3
−10.0	0.995	0.996	0.1

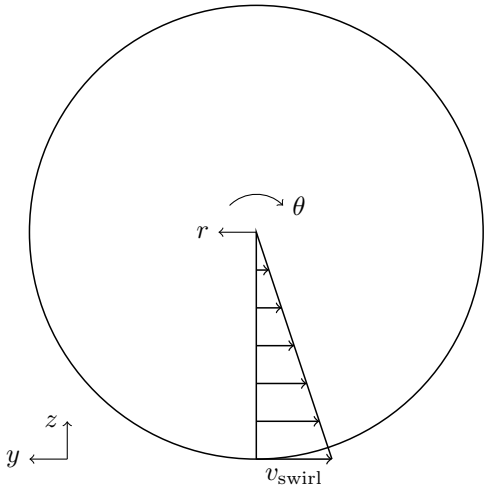

Figure 5.4: Swirling velocity component added to the inlet velocity viewed from upstream the inlet.

yaw curves measured in the wind tunnel tended to be asymmetric, with a slightly larger yaw being measured for positive than for negative angles. After concluding that the asymmetry was not replicated in CFD it was decided to investigate how a non-uniform velocity distribution was connected to the drag accuracy. One source of possible non-uniformity could be a remaining swirl component from the fan rotation.

Figure 5.4 illustrates the swirling component that was added to the velocity field at the inlet, resulting in the velocity vector

$$\mathbf{v} = \left(\frac{v_\infty}{\eta}, v_{\text{swirl}} \frac{R}{r} \sin\theta, -v_{\text{swirl}} \frac{R}{r} \cos\theta \right), \tag{5.2}$$

where R is the radius of the inlet, v_∞ is the desired velocity in the test section and η is the contraction ratio. The cylindrical coordinates r and θ are specified according to figure 5.4. It was desired to obtain a yaw angularity of approximately 1° in the test section. Therefore a number of iterations using an empty tunnel was performed in order to find a suitable value of v_{swirl}, which resulted in the desired yaw angle of the flow after the converging nozzle. With a test section velocity $v_\infty = 25\,\text{m/s}$ it was found that $v_{\text{swirl}} = 0.5\,\text{m/s}$ resulted in a one degree yaw angle approximately two to three meters above the ground, which would correspond to approximately the height of the windscreen of a truck. The yaw angle, φ, was defined as $\varphi = \arctan(v_y/v_\infty)$. In figure 5.5 the resulting yaw angle of the flow is shown in the plane at the beginning of the test section with and without the added swirl component. It can be seen that even without the swirling component there exist local yaw angles in the flow, which is to be expected because of the converging nozzle and the transition from a circular to a rectangular profile. However, studying the flow direction it can be seen that the flow is symmetric, both around the vertical and the horizontal midplane. For the case with the swirl component added it can be seen that a distinct swirl remains after the converging nozzle. This results in a negative yaw angle in the bottom half of the test section and a positive angle in the top half. For the chosen v_{swirl} local yaw angles above three degrees are obtained. In addition to the yaw angle the streamwise velocity was also investigated. However, no significant impact from the swirl was observed on the streamwise velocity.

Table 5.2 shows the effect of the added swirl on the drag coefficient for different yaw angles using the DSL = 1.2 k-ε model. Additionally, in order to investigate any unsteady effects, two yaw angles were simulated using the SST IDDES model. Firstly it can be noted that the swirl adds drag, regardless of the yaw angles. Secondly, there is no significant difference between the k-ε and IDDES models, with both models predicting similar increases in drag from the swirl. Furthermore it can be seen that the increase in drag is dependent on the yaw angles, with the smallest addition being obtained for zero yaw and the largest for $-2.5°$ yaw. The dependence on yaw angle is further investigated by examining the accumulated ΔC_D with and without swirl, which is shown in figure 5.6. As a first observation it can be seen that similar effects are obtained for all yaw angles except zero. This could be explained by the fact that the addition of swirl is similar to a small change in yaw angle. For the swirl added in this investigation the effect is similar to a slight decrease of the already negative yaw angle, hence increasing the magnitude of the angle. Investigating the yaw curve for this truck it was found that the curve is rather flat close to zero, implying that a small change of the yaw angle close to zero should

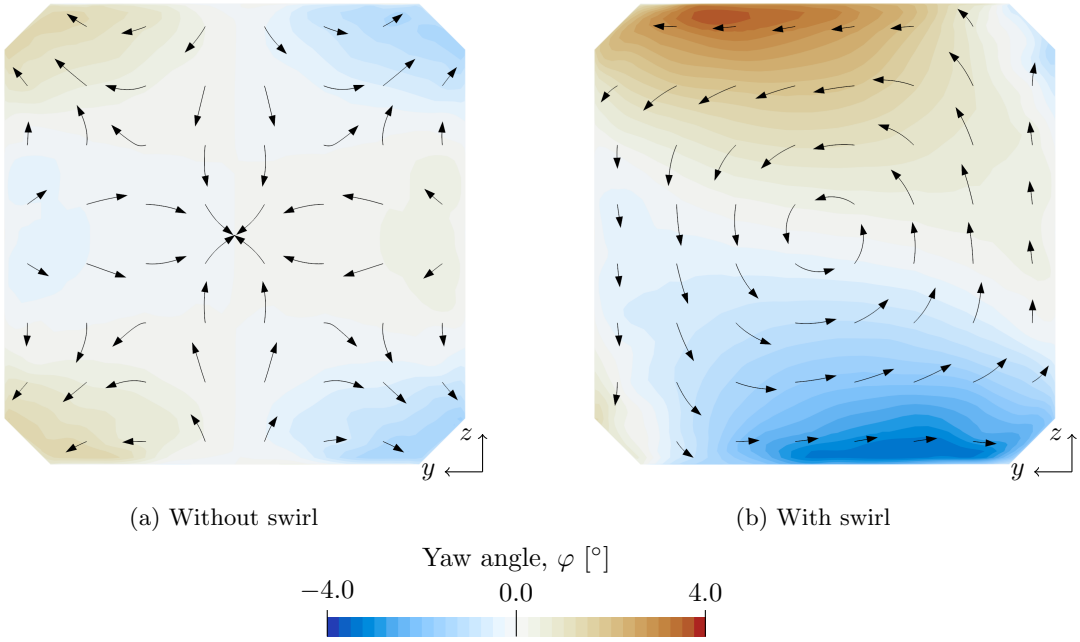

(a) Without swirl

(b) With swirl

Figure 5.5: Yaw angle and flow direction at the beginning of the test section with and without swirl at the inlet.

Table 5.2: Normalized C_D with and without swirl for the k-ε and SST IDDES (only two yaw angles) models at different yaw angles.

Yaw angle [°]	DSL = 1.2 k-ε			SST IDDES		
	No swirl	Swirl	Δ [%]	No swirl	Swirl	Δ [%]
0.0	0.868	0.896	2.8	0.921	0.952	3.2
−2.5	0.912	1.009	9.7			
−5.0	0.970	1.047	7.7	1.006	1.082	7.7
−7.5	0.989	1.049	6.0			
−10.0	0.996	1.041	4.5			

result in a small change in drag. Apart from zero yaw similar effects of the swirl is seen along the cab, with the first significant difference being obtained at the tractor wheels. There the −5.0° and −7.5° yaw angles shows a larger increase in drag with swirl. Along the trailer some difference can be seen, with the drag difference of the −5.0° yaw case increasing more rapidly than the other models. Similarly to at the tractor rear wheels, large differences are obtained at the trailer wheels. For 0.0°, −7.5° and −10.0° yaw little or no difference is seen at the trailer wheels. For −5.0° and, most significantly, −2.5° yaw a large increase is seen at the trailer wheels and mudflaps. Finally the swirl alters the wake flow, lowering the base pressure and increasing the drag at all yaw angles.

As an example of the effects seen at the wheels the difference in total pressure coefficient, $\Delta C_{P,tot}$, with and without swirl is shown 150 mm above the ground in figure 5.7 for yaw angles −2.5° and −5.0°. In figure 5.7a it can be seen that the large difference in accumulated ΔC_D can be explained by the effectively larger yaw angle, causing more of the front wheel wake to collapse on the trailer wheels at the right side of the truck. This causes both a larger pressure on the forward facing surface of the tires, as well as a different tire wake, which influences the overall trailer wake. Figure 5.7b compares the cases with and without swirl at −5.0° yaw. Here some difference is noted at the trailer wheels, but more significantly, a large difference is seen at the tractor rear wheels. Similarly to the −2.5° case the effectively larger yaw angle alters the front wheel wake, however, at this angle, the front wheel outwash hits the tractor rear wheels in a larger extent.

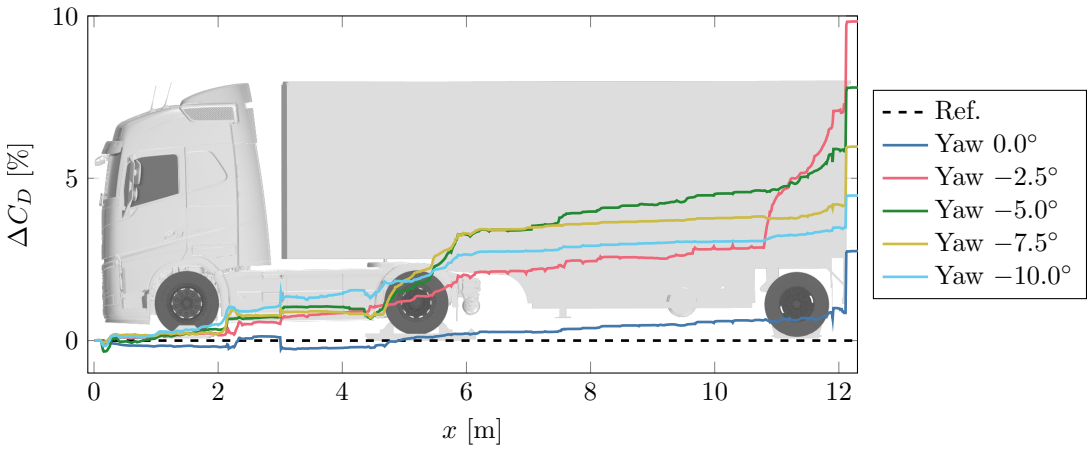

Figure 5.6: Accumulated ΔC_D at different yaw angles with and without swirl for the k-ε model. A positive value indicates higher drag for the configuration with swirl. Note that the ΔC_D is calculated using the normalized value.

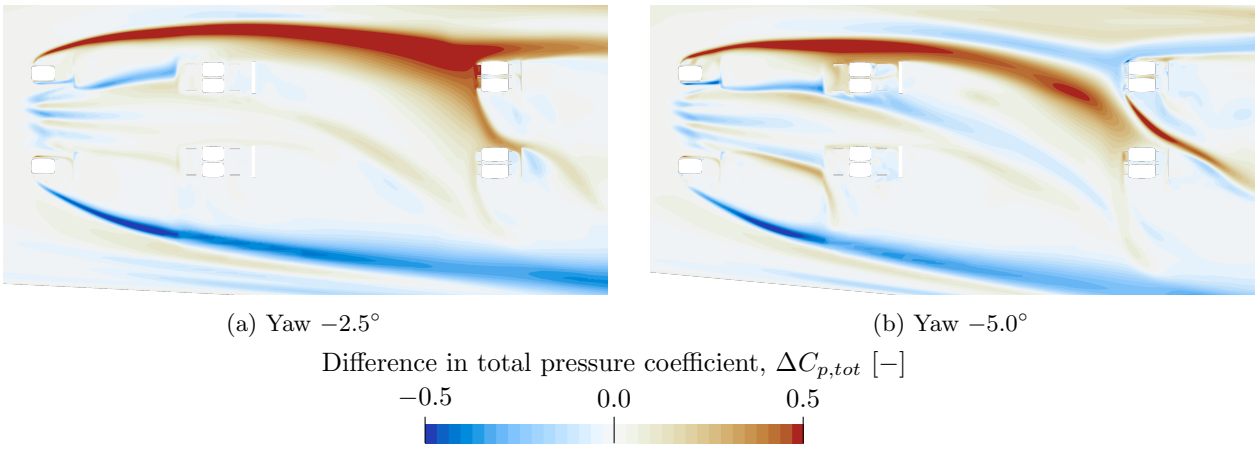

(a) Yaw −2.5°

(b) Yaw −5.0°

Figure 5.7: Difference in total pressure coefficient 150 mm above the ground with and without swirl for −2.5° and −5.0° yaw.

5.3 Turbulent boundary conditions

In order to improve the correlation between CFD and the wind tunnel the boundary conditions of the turbulence model are investigated. These conditions can be specified in a number of ways, for example by directly prescribing quantities such as k and ε (or ω) on the boundary. However, in this thesis these were specified in terms of the turbulent intensity, I, and the turbulent viscosity ratio, μ_t/μ. The turbulent intensity is defined as [32]

$$I = \frac{v'}{\bar{v}}, \quad v' = \sqrt{\frac{1}{3}\left(v_x'^2 + v_y'^2 + v_z'^2\right)} = \sqrt{\frac{2}{3}k}, \quad \bar{v} = \sqrt{\bar{v}_x^2 + \bar{v}_y^2 + \bar{v}_z^2}. \tag{5.3}$$

Using the turbulent intensity and viscosity ratio the turbulent quantities are then, for k-ε and k-ω models, calculated as [13]

$$k = \frac{3}{2}\left(Iv\right)^2, \quad \varepsilon = \frac{\rho C_\mu k^2}{\left(\mu_t/\mu\right)\mu}, \quad \omega = \frac{\rho k}{\left(\mu_t/\mu\right)\mu}. \tag{5.4}$$

Previous research has showed that the turbulence in a wind tunnel can affect the measured drag coefficients. McAuliffe and D'Auteuil [33] developed and commissioned a system to reproduce turbulent conditions measured on road at 30% scale in the NRC 9 m wind tunnel. Measurements on a 30% scale model truck showed approximately 2% decrease in drag when using the turbulence system, compared to the wind tunnel standard configuration. NRC has communicated that the turbulent intensity in the test section is approximately 1%. However, no data regarding the viscosity ratio (or other turbulent quantity which could be used to calculate the viscosity ratio) has been found. Ross et al. [29] also investigated the correlation between CFD and measurements in the NRC 9 m wind tunnel, using a turbulent intensity of 1% and a viscosity ratio of 200. These values were claimed to be representative for a typical and relatively clean wind tunnel. It should be noted that these conditions were specified at the inlet. However, Ross et al. used a wind tunnel without a converging nozzle and diffuser, instead extending the test section in both directions. Therefore it is believed that the values in the test section were similar. Based on the data from NRC and values used by Ross et al. the target values for the turbulent intensity and viscosity ration in the test section are set to 1% and 200, respectively.

The target values for the turbulent quantities were known for the test section but should be specified at the inlet. Since the converging nozzle was included in the wind tunnel geometry a number of simulations in the empty wind tunnel were performed in order to find how the turbulent quantities were changed by the nozzle. These were evaluated by comparing the values specified at the inlet to the surface averaged values at the beginning of the test section. It was found that change of the turbulent viscosity over the nozzle was small. Hence the turbulent intensity at the inlet was altered while keeping the viscosity ratio constant. Figure 5.8 shows the turbulent intensity and viscosity ratio in the test section as a function of the turbulent intensity at the inlet for a constant inlet viscosity ratio of 200. The turbulent intensity in the test section, I_{TS}, varies almost linearly with the intensity at the inlet, I_{in}. Furthermore, it can be seen that the turbulent viscosity ratio in the test section, $(\mu_t/\mu)_{\mathrm{TS}}$, decreases with increased turbulent viscosity, although the values are close to the turbulent viscosity ratio specified at the inlet (200). Based on these results it was decided to use the values $I_{\mathrm{in}} = 6.0\%$ and $(\mu_t/\mu)_{\mathrm{in}} = 200$ for the further investigations.

Table 5.3 presents the normalized drag coefficients at yaw angles $0.0°$ and $-5.0°$ for $I_{\mathrm{in}} = 0.2\%$ and $I_{\mathrm{in}} = 6.0\%$. This is done for both the DSL = 1.2 k-ε and the SST IDDES model. For both turbulence models the results are almost identical for the different turbulence levels, with only a tiny difference being observed for the IDDES model, which might be explained by the solution not being averaged over a sufficient amount of time. When investigating the accumulated ΔC_D it was found that the k-ε model predicted almost identical drag along the truck, with the ΔC_D consistently being less than 0.5 drag counts. For the IDDES model larger ΔC_D was observed, reaching 4 drag counts. However, these might be a result of the averaging time not being sufficient.

5.4 Conclusions

In order to better replicate the conditions in the wind tunnel three different aspects were investigated. Firstly the geometry of the wind tunnel converging nozzle was modified. It was observed that the nozzle geometry had an effect on both the boundary layer and the velocity distribution. However the effect on the drag of the truck was negligible. Furthermore, based upon communications with engineers at NRC, a non-uniform

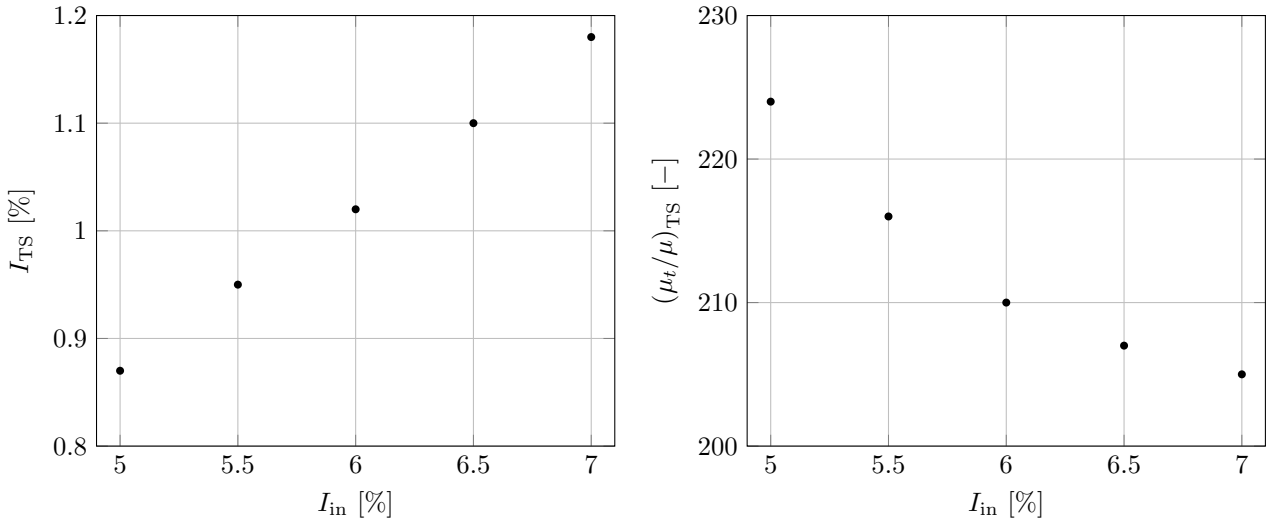

(a) Turbulent intensity in test section

(b) Turbulent viscosity ratio in test section

Figure 5.8: Turbulent intensity and viscosity ratio in the test section as a function of the turbulent intensity at the inlet for constant $(\mu_t/\mu)_{\mathrm{in}} = 200$.

Table 5.3: Normalized C_D for $I_{\mathrm{in}} = 0.2\%$ and 6.0% predicted by the DSL = 1.2 k-ε and the SST IDDES models at yaw angles 0.0° and −5.0°.

Yaw angle [°]	DSL = 1.2 k-ε			SST IDDES		
	$I_{\mathrm{in}} = 0.2\%$	$I_{\mathrm{in}} = 6.0\%$	Δ [%]	$I_{\mathrm{in}} = 0.2\%$	$I_{\mathrm{in}} = 6.0\%$	Δ [%]
0.0	0.868	0.868	0.0	0.921	0.922	0.1
−5.0	0.970	0.970	0.0	1.006	1.004	−0.2

velocity distribution was investigated. From the information provided a coarse approximation of the velocity distribution was constructed. From the resulting drag values and flow fields it was found that the chosen velocity distribution resulted in an effect similar to altering the yaw angle. Finally the boundary conditions of the turbulent quantities were investigated. However, in terms of drag, the differences observed were negligible.

In conclusion it is still believed that a large part of the problems with correlating the CFD to the wind tunnel, especially at small yaw angles, can be explained by the modelling of the tunnel. Furthermore it is believed that the largest problem is the velocity distribution entering the test section. In order to continue the investigation more experimental data is needed. As a starting point future wind tunnel campaigns should include pressure measurements at the surface of the truck in critical areas such as the tractor-trailer gap and at the trailer base for this specific test setup. Furthermore it would be beneficial if measurements of dynamic pressure (corresponding to velocity) could be conducted in the beginning of the test section. This could be performed by the NRC using an empty wind tunnel, were the data is provided to customers of the tunnel. Alternatively, this could be performed by Volvo with a truck mounted in the test section. Among these options the later might be preferred since the large blockage of the truck likely influences the field in the beginning of the test section. If these measurements were performed on a sufficiently fine grid (using for example a traversing unit) this field might be used as the inlet boundary conditions using a modelling approach were the converging nozzle is not included and replaced with a straight extension of the test section. These measurements likely needs to be performed at multiple yaw angles since the difference in blockage would alter the velocity field. In addition to obtaining more knowledge about the uniformity of the flow further investigations would also benefit greatly from knowing exactly how the velocity is measured.

6 Conclusions

This thesis investigated different approaches for improving the accuracy and robustness of CFD simulations for commercial vehicles. Firstly the influence of turbulence modelling was investigated. 13 turbulence models were evaluated using a simplified truck model and compared to both wind tunnel and LES data. From these models four RANS and two IDDES models were compared to wind tunnel measurements by simulating a fully detailed truck in the wind tunnel environment. It was found that the accuracy of the drag prediction was heavily dependent on the yaw angle, where large yaw angles resulted in better correlation. Furthermore, weighting all yaw angles equally, the three k-ε and k-ω models all resulted in an average drag prediction error of approximately 6%, whereas both IDDES models predicted the drag with an average error of 3.5%. The Spalart-Allmaras model resulted in an average error of 1.6% and was the only model that accurately predicted the drag at zero yaw. Examining the side force prediction and comparing the flow fields it is believed that the superior drag prediction of the Spalart-Allmaras model was due to error cancellation.

Combining the force prediction and the numerical stability of the models it is recommended to use either the DSL = 1.2 k-ε or the DSL = 1.2 $a_1 = 1$ k-ω method in the CFD process for RANS simulations. It is believed that choosing the DSL = 1.2 $a_1 = 1$ k-ω method might improve problems with bistable states, sometimes experienced when using the DSL = 1.2 k-ε model. For the IDDES method no significant differences between the models were obtained. However, in the case were a k-ω model is used for the RANS method it might prove beneficial to also use a k-ω model in the near-wall region of the IDDES method.

Secondly the potentials of improving the modelling of the wind tunnel environment were investigated. Using data from experiments and numerical simulations of an empty wind tunnel the influence from a new converging nozzle, which was believed to be a better replication of the actual geometry, was investigated. However, when comparing the drag prediction on the detailed truck for the different nozzles no significant difference was found. Later, as an attempt to explain the difference in correlation between small and large yaw angles, the effects of a non-uniform velocity distribution at the wind tunnel inlet was investigated. Based upon conversations with wind tunnel engineers, a swirling component was added to the flow. It was found that the swirl affected the flow similarly to an equivalent change in yaw angle. Furthermore no indications were found that suggested that a swirling component could explain the difference in correlation between yaw angles. Finally the effects of the turbulence level in the test section was investigated. These changes had no significant impact on the drag prediction.

A mesh study was performed investigating potential improvements of the current mesh strategy with the aim of approaching mesh independence. By examining how much critical quantities such as the streamwise velocity and the pressure changed per computational cell a number of regions were identified for which different refinements were investigated. It was found that the most critical regions to refine were the shear layers in both the trailer base wake and the tractor-trailer gap.

6.1 Future work

It is recommended that upcoming wind tunnel tests using the FH-1823 include measurements of local flow field quantities in addition to the global forces. As a first step grids of pressure spades could be mounted at areas such as the trailer base and the tractor-trailer gap. These measurements could greatly help improving the understanding of the results in this thesis. Furthermore it is also recommended that the next wind tunnel campaign investigates how the velocity is measured in the wind tunnel and how the measurement is affected by the blockage, especially at large yaw angles. Replicating this measurement in CFD could potentially improve the correlation.

Additionally there is great potential for improving the DES method. There are a number of parameters that could be examined more thoroughly in order to mature the method and make it more affordable for use in the development process at Volvo. These include different meshes specific for DES, the length of the time step, the number of inner iterations and the process used to initialize the simulations, among others.

Finally, assuming that the convergence problems can be solved, a mesh study should be performed in the wind tunnel environment. The general trends from the simulations actually performed in the wind tunnel

environment showed a different response to mesh refinements than the open road simulations, especially at the underbody. A thorough mesh study in the wind tunnel could benefit the general correlation study greatly.

References

[1] *Road transport: Reducing CO2 emissions from vehicles*. European Commission. 2018. URL: https://ec.europa.eu/clima/policies/transport/vehicles_sv (visited on 30/10/2018).

[2] *Reducing CO2 emissions from heavy-duty vehicles*. European Commission. 2018. URL: https://ec.europa.eu/clima/policies/transport/vehicles/heavy_en#tab-0-0 (visited on 30/10/2018).

[3] W. H. Hucho. *Aerodynamics of Road Vehicles*. 4th ed. Society of Automotive Engineers, 1998. ISBN: 0-7680-0029-7.

[4] J. Katz. *Race Car Aerodynamics: Designing for Speed*. 2nd ed. Bentley Publishers, 2006.

[5] L. Davidsson. *Fluid mechanics, turbulent flow and turbulence modeling*. Chalmers University of Technology, 2018.

[6] H. K. Versteeg and W. Malalasekera. *An introduction to computational fluid dynamics - The finite volume method*. Longman Scientific & Technical, 1995.

[7] A. A. Matyushenko and A. V. Garbaruk. Adjustment of the k-ω SST turbulence model for prediction of airfoil characteristics near stall. *Journal of Physics: Conference Series* **769**.1 (2016). ISSN: 17426596. DOI: 10.1088/1742-6596/769/1/012082.

[8] F. J. Ross and S. Herrman. Vehicle Aerodynamics. 2016.

[9] *V2-f models*. CFD Online. 2014. URL: https://www.cfd-online.com/Wiki/V2-f_models (visited on 16/10/2018).

[10] L. Davidsson. *An Introduction to Turbulence Models*. Chalmers University of Technology, 2018.

[11] *Spalart-Allmaras model*. CFD Online. 2015. URL: https://www.cfd-online.com/Wiki/Spalart-Allmaras_model (visited on 01/03/2019).

[12] L. Sterken, S. Sebben and L. Löfdahl. Numerical Implementation of Detached-Eddy Simulation on a Passenger Vehicle and Some Experimental Correlation. *Journal of Fluids Engineering* **138**.9 (2016), 091105. ISSN: 0098-2202. DOI: 10.1115/1.4033296. URL: http://fluidsengineering.asmedigitalcollection.asme.org/article.aspx?doi=10.1115/1.4033296.

[13] *Star-CCM+ Documentation*. 13th ed. Siemens.

[14] P. A. Durbin. On the k-3 stagnation point anomaly. *International Journal of Heat and Fluid Flow* **17**.1 (1996), 89–90. ISSN: 0142727X. DOI: 10.1016/0142-727X(95)00073-Y.

[15] F. M. White. *Fluid Mechanics*. 7th ed. McGraw-Hill Education, 2011.

[16] A. Lozano-Duran and J. Jimenez. *Effect of the computational domain on direct simulations of turbulent channels up to Re_τ=4200*. 2014. URL: https://torroja.dmt.upm.es/ftp/channels/data/statistics/Re4200/profiles/Re4200.prof (visited on 14/11/2018).

[17] E. Ljungskog. "Investigations of Flow Conditions in an Automotive Wind Tunnel". Licentiate. Chalmers University of Technology, 2017.

[18] *Ahmed body*. CFD Online. 2015. URL: https://www.cfd-online.com/Wiki/Ahmed_body (visited on 29/04/2019).

[19] *DrivAer Model*. Technical University of Munich. 2019. URL: http://www.aer.mw.tum.de/en/research-groups/automotive/drivaer/ (visited on 29/04/2019).

[20] N. Ashton et al. Assessment of RANS and DES methods for realistic automotive models. *Computers and Fluids* **128** (2016), 1–15. ISSN: 00457930. DOI: 10.1016/j.compfluid.2016.01.008. URL: http://dx.doi.org/10.1016/j.compfluid.2016.01.008.

[21] J. Allan. Aerodynamic drag and pressure measurements on a simplified tractor-trailer model. *Journal of Wind Engineering and Industrial Aerodynamics* **9**.1-2 (Nov. 1981), 125–136. ISSN: 01676105. DOI: 10.1016/0167-6105(81)90083-0.

[22] J. Östh and S. Krajnović. The flow around a simplified tractor-trailer model studied by large eddy simulation. *Journal of Wind Engineering and Industrial Aerodynamics* **102** (Mar. 2012), 36–47. ISSN: 01676105. DOI: 10.1016/j.jweia.2011.12.007.

[23] *9 m wind tunnel*. National Research Council Canada. 2018. URL: https://www.nrc-cnrc.gc.ca/eng/solutions/facilities/wind_tunnel/nine_metre.html (visited on 31/10/2018).

[24] K. Garry et al. The Effect of Aerodynamic Drag of the Longitudinal Position of a Road Vehicle Model in a Wind tunnel Test Section. *SAE 1994 Transactions: Journal of Passenger Cars* **V103-6**.940414 (1994), 478–489. ISSN: 8756663X. DOI: 10.1002/ecjb.10032. URL: http://papers.sae.org/940414/.

[25] G Larose et al. The new boundary layer control system for NRC's 9 mx 9 m wind tunnel (2001).

[26] F Menter. *Best Practise: Scale-Resolving Simulations in ANSYS CFD*. Tech. rep. ANSYS, 2012.

[27] S. Nayani et al. Numerical Simulation of a Complete Low-Speed Wind Tunnel Circuit (2016), 1–17. DOI: 10.2514/6.2016-2117.

[28] H. Martini, P. Gullberg and L. Löfdahl. Comparative Studies between CFD and Wind Tunnel Measurements of Cooling Performance and External Aerodynamics for a Heavy Truck. *SAE International Journal of Commercial Vehicles* **7**.2 (2014), 2014–01–2443. ISSN: 1946-3928. DOI: 10.4271/2014-01-2443. URL: http://papers.sae.org/2014-01-2443/.

[29] F. Ross et al. Class 8 Truck Investigation Comparing Wind Tunnel Test to Simulated Open Road Performance Using CFD (2018), 1–8. ISSN: 01487191. DOI: 10.4271/2018-01-5010.

[30] D. Söderblom, P. Elofsson and A. Hyvärinen. Numerical Investigation of Blockage Effects on Heavy Trucks in Full Scale Test Conditions (2016). ISSN: 01487191. DOI: 10.4271/2016-01-1607. URL: http://papers.sae.org/2016-01-1607/.

[31] S. Bisson et al. Recent Improvements to the NRC 9 m × 9 m Wind Tunnel. *Canadian Aeronautics and Space Journal* **51**.3 (2011), 95–105. ISSN: 1712-7998. DOI: 10.5589/q05-009.

[32] *Turbulence intensity*. CFD Online. 2018. URL: https://www.cfd-online.com/Wiki/Turbulence_intensity (visited on 18/03/2019).

[33] B. R. McAuliffe and A. D'Auteuil. A System for Simulating Road-Representative Atmospheric Turbulence for Ground Vehicles in a Large Wind Tunnel. *SAE International Journal of Passenger Cars - Mechanical Systems* **9**.2 (2016), 2016–01–1624. ISSN: 1946-4002. DOI: 10.4271/2016-01-1624. URL: http://papers.sae.org/2016-01-1624/.

[34] *How to optimize mesh refinement based on pressure field*. Siemens. 2017. URL: https://thesteveportal.plm.automation.siemens.com/articles/en_US/FAQ/How-to-optimize-mesh-refinement-based-on-pressure-field (visited on 12/04/2019).

[35] *Should I use the coupled or the segregated solver for my simulation?* Siemens. 2017. URL: https://thesteveportal.plm.automation.siemens.com/articles/en_US/FAQ/Should-I-use-the-coupled-or-the-segregated-solver-for-my-simulation-temp (visited on 03/05/2019).

A Mesh study

The solution of a finite volume problem can be affected significantly by the computational mesh used to solve the equations. In order to avoid this source of error a mesh is usually successively refined until the difference in results between meshes are negligible. [6] As an attempt to investigate whether the compromise between mesh resolution and computational cost can be improved a mesh study will be conducted.

A.1 Method

A mesh study can be conducted in a number of different ways. Assuming that a baseline mesh already exists, one method is to change the size of the complete mesh by changing the parameter determining the size of the standard cell, in Star-CCM+ denoted base size. However, since all cells are refined the same amount, this method is inefficient. Another method, which will be used in this study, is to introduce specific refinement regions. By investigating how the solution is affected by the positioning and level of refinement the mesh convergence can be judged.

The mesh study was initially planned to be conducted using the wind tunnel geometry. However, when refining the mesh it proved more difficult to converge the solutions. Steady state simulations were conducted where no sign of convergence was observed even after 30000 iterations. From previous experience from simulations using the wind tunnel geometry it was known that these simulations generally are harder to converge than open road simulations. Therefore it was decided to conduct the mesh study in open road conditions. However the same truck and trailer geometry was still used, with some minor modifications to the trailer positioning, required after the removal of the wind tunnel mounting. One major drawback of performing the simulations for open road conditions was that no correlation data was available. Instead it was decided that the mesh study should focus on achieving mesh convergence.

In the sections below the mesh used as the baseline will firstly be presented. Later the simulation setup will be discussed, with the focus being the differences when using an open road setup.

A.1.1 Baseline mesh

The baseline mesh uses almost identical mesh settings and refinement strategies as the mesh used in the wind tunnel, which is presented in section 4.1.3. Since the open road conditions removes the need for resolving the boundary layers at the walls of the computational domain no prism layers were built at these surfaces, reducing the cell count from approximately 170 to 160 million cells. The mesh is shown in figure A.1.

Furthermore it was noted early on in the mesh study that the high y^+ approach used on the trailer resulted in rough transitions between the prism and trimmer cells when refining the wake. Therefore the prism layers at the five external sides of the trailer was changed to a low y^+ approach. Comparing the two y^+ settings a maximum difference of approximately one drag count was observed for the accumulated C_D and the cell count increased by approximately one million cells. Hence it was decided to continue with the low y^+ mesh.

This study uses the trimmer mesher combined with prism layers next to the wall. In the trimmer mesh the standard cell is a cube with the side length being the base size. Furthermore the side lengths can only be altered by a factor of two. Hence all side lengths are related to the base size by a factor of 2^n, where n is an integer. The baseline mesh is constructed in such a way that most of the mesh around the truck, such as wake and underbody refinements are set to the base size. A cell can be refined either isotropically, where all side lengths are equal, or anisotropically, where the side lengths can be differ. Both types of refinements will be used in this study.

A.1.2 Simulation setup

The open road simulations used a domain measuring $129\,\mathrm{m} \times 40.0\,\mathrm{m} \times 25.5\,\mathrm{m}$ (length×width×height). An inlet velocity condition of 90 km/h was used together with an outlet pressure conditions. The ground was modelled as a no-slip wall with the same velocity as the inlet. The side and top walls used a symmetry boundary condition. Finally the wheel rotation was modelled by applying a rotational velocity to the walls of the wheels. In terms of turbulence modelling the DSL = 1.2 $a_1 = 1$ k-ω model was used. The model was chosen since it proved to

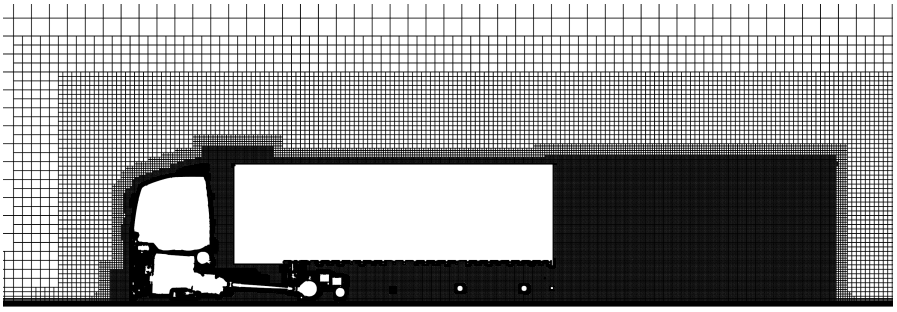

(a) $y = 0.0\,\mathrm{m}$

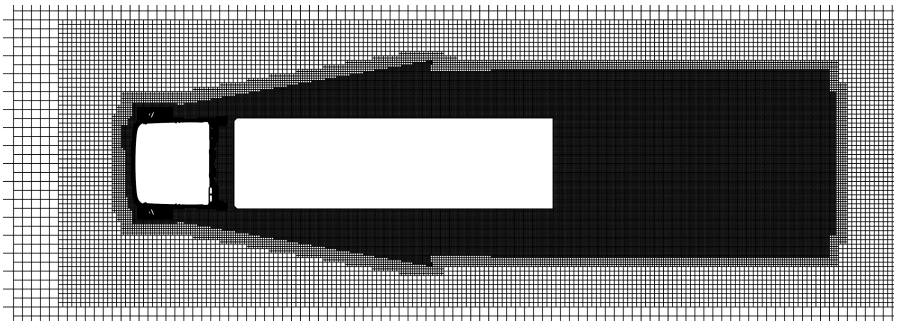

(b) $z = 2.0\,\mathrm{m}$

Figure A.1: Mesh used as baseline for the mesh study.

perform similar, or slightly better, than the k-ε model. Furthermore, compared to the remaining k-ω and the Spalart-Allmaras model the oscillations in C_D are smaller. This is believed to be important since it is desired to be able to distinguish small differences between different meshes.

A.1.3 Post-processing

A mesh should consist of finer cells in areas with large gradients. In order to quantify how different mesh refinements fulfill this criteria the results will be analyzed by studying the rate of change per cell for different quantities. Given a scalar field, Φ, the rate of change per cell, $\hat{\Phi}$, can be expressed as

$$\hat{\Phi} = |\nabla\Phi|\, l \approx |\nabla\Phi|\, V^{1/3}, \tag{A.1}$$

where l is the cell side length and V is the cell volume. [34] The approximation of l is used both because anisotropic refinements will be used and because the cell side length is not available as a field function in Star-CCM+. $\hat{\Phi}$ will have the same dimension as Φ. Using for example the pressure field, P, $\hat{P}$ can be interpreted as "Pascals per cell".

In order to determine to what extent mesh convergence has been reached a number of different quantities can be examined. Firstly the drag coefficients, C_D, can be compared. However this measurement is quite coarse, since different mesh refinements might redistribute where the drag is predicted, without a significant change on the overall drag. In order to determine the distribution of drag the accumulated C_D will be used.

A.2 Results

In this section the results of the mesh study will be presented. Firstly the baseline mesh will be analyzed and potential areas of improvement will be identified. These areas will then be refined and the effects will be discussed.

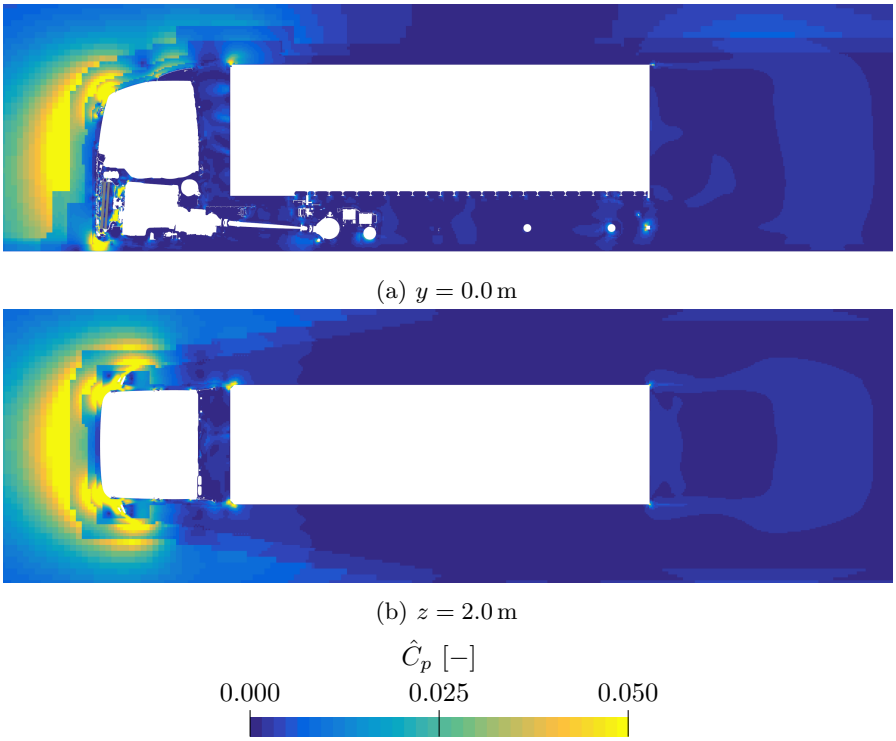

(a) $y = 0.0\,\mathrm{m}$

(b) $z = 2.0\,\mathrm{m}$

Figure A.2: Magnitude of C_p gradient per cell for baseline mesh.

A.2.1 Baseline mesh

In order to determine where to introduce the different mesh refinements the changes per cell, described in section A.1.3, were investigated for the baseline mesh. These investigations were performed for the pressure, velocity components and the turbulent kinetic energy. The areas with the largest changes was found to vary depending on which quantity was investigated. However it was generally found that the y- and z-velocity components experienced large gradients in the same areas as the x-velocity, which can be explained by the velocity gradients being coupled by the continuity equation. Furthermore it was also found that the turbulent kinetic energy and the x-velocity indicated large gradients in the same regions. Comparing the pressure and x-velocity some similarities were found, however these were less obvious than for the other quantities. Therefore the main focus will be on investigating the changes in the x-velocity and the pressure, $\hat{v}_x$ and $\hat{C}_p$. Note that the pressure is presented in terms of the pressure coefficient.

In figure A.2 $\hat{C}_P$ is shown in the planes $y = 0.0\,\mathrm{m}$ and $2.0\,\mathrm{m}$. Note that the range of the scale was chosen only to clearly show which areas had the largest changes per cell. No interpretation of the actual magnitude of the quantity will be performed. The values will only be used to compare different mesh refinements. Examining figure A.2 it can be seen that the largest changes per cell are obtained in front of the cab as well as around the a-pillars and in front of the rear-view mirrors. Further downstream the only large changes are noted around the leading edges of the trailer.

Investigating the changes in streamwise velocity, $\hat{v}_x$, in figure A.3 it can, similarly as for the pressure coefficient, be seen that large values are obtained in front of the truck. More significantly large values are obtained further downstream, where it is clear that the shear layers, both from the rear-view mirrors as well as behind the trailer, creates large gradients. Similarly a region of large changes in streamwise velocity is obtained under the tractor, where there is a transition between the high-velocity air being accelerated under the bumper spoiler and the almost stationary air in the chassis. Examining the tractor-trailer gap large values are obtained in the shear layers created by the gap between the deflectors and the trailer. These large gradient seem to remain further downstream, which is most notable on top of the trailer.

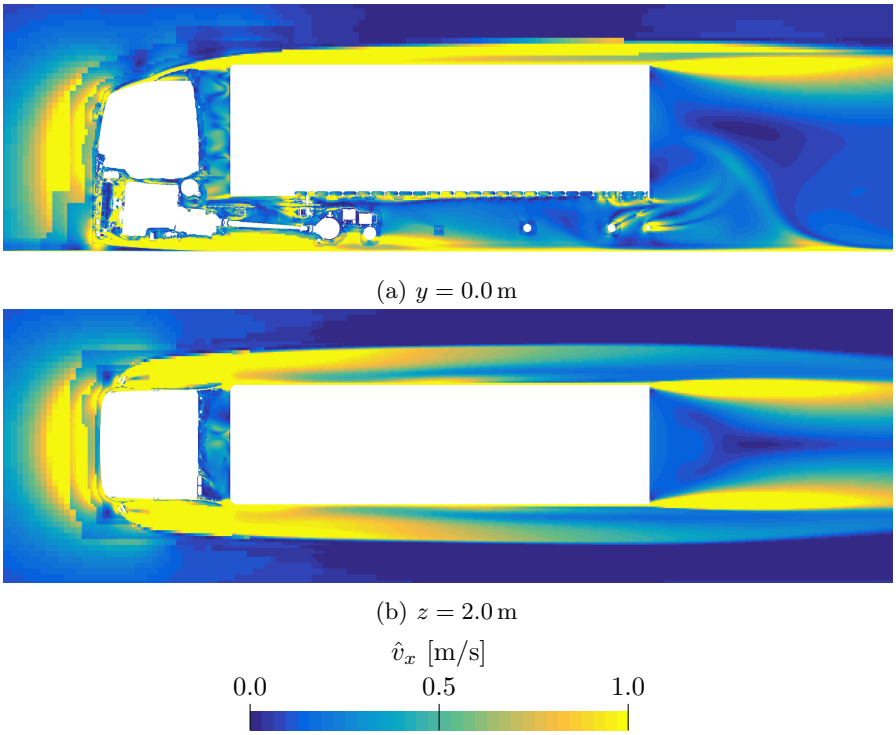

(a) $y = 0.0\,\mathrm{m}$

(b) $z = 2.0\,\mathrm{m}$

Figure A.3: Magnitude of v_x gradient per cell for baseline mesh.

A.2.2 Mesh refinements

After identifying the regions with large gradients per cell a number of different refinement regions were constructed, these are shown in figure A.4. The refinements were introduced accumulatively which allowed the impact of each refinement to be evaluated. These configurations are described in table A.1 where the sizes and directions of the refinements are shown as well as the number of cells. When the description "gradient direction" is used the anisotropic refinement was applied in the direction in which the largest component of the gradient was obtained. As an example the shear layer refinements were therefore applied in the y-direction at the sides and in the z-direction at the top of the trailer.

Cab box, cab radius and trailer shear layers

As a first attempt to improve the mesh the area around the cab was refined to reduce the gradients in the stagnation region, which is shown in figure A.4a. Using a medium isotropic refinement the cell count increased by 14 million cells. Since the next level of refinement would increase this number by approximately a factor of eight this was the only refinement level investigated. In figure A.5 the accumulation of ΔC_D compared to the baseline mesh is shown. The cab box, denoted B, decreases the drag slightly over the cab front and reduces the trailer gap losses slightly. Configurations C, D and E in figure A.5 combines the cab box with different levels of anisotropic refinements in the main gradient direction, both at the radiuses of the cab front and in the shear layers of the trailer wake. These refinements are shown in figure A.4b. Examining the accumulated ΔC_D along the tractor all configurations results in values similar to only using the cab box, indicating no major influence from the front ring. At the trailer base more significant differences can be seen where the shear layer refinements result in a larger base pressure being predicted. Similar effects are obtained for all refinement levels. Examining the ΔC_D of configuration E a less smooth curve can be seen. This is believed to be explained by the solution not being converged to the same level as the other configurations. Since all simulations were run for the same number of iterations this could be explained by the fact that the number of iterations required to converge a solution generally increases with the cell count when using a segregated solver. [35] Furthermore, the very fine refinement of configuration E resulted in a high cell aspect ratio, which can influence the numerical stability. Considering the similarities in results between the meshes, the different cell counts and the numerical stability it was decided to use the refinement of configuration D for the upcoming investigations.

(a) Cab box

(b) Cab radius (blue) and shear layer (red) rings

(c) Tractor-trailer gap ring, note that the trailer is hidden in the rear view

(d) Trailer top

(e) Underbody

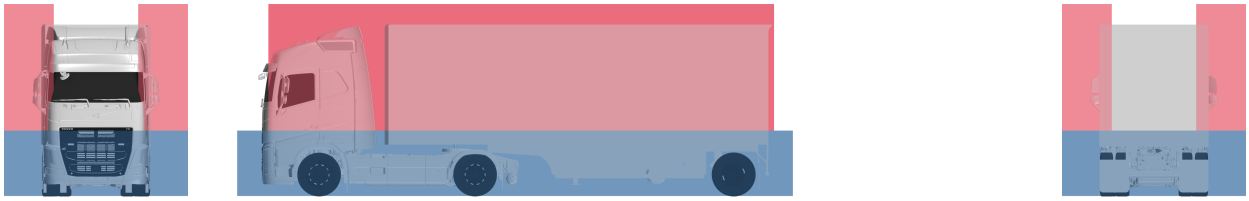

(f) Wide underbody (blue) and side (red) boxes

(g) Rear-view mirrors

Figure A.4: Regions for mesh refinements.

Table A.1: Combinations of mesh refinements investigated, the level of refinement as well as the cell count.

Denotation	Description	Refinement	Cells (millions)	
			Count	Δ
A	Baseline	-	163	0
B	A + Cab box	Medium, isotropic	177	14
C	B + Cab radius and shear layer	Medium, gradient direction	179	16
D		Fine, gradient direction	187	24
E		Very fine, gradient direction	222	60
F	D + Trailer gap	Fine, gradient direction	189	26
G		Very fine, gradient direction	201	38
H		Ultra fine, gradient direction	264	101
I	G + Trailer top	Medium, z-direction	202	39
J		Fine, z-direction	204	41
K	I + Underbody	Medium, z-direction	203	40
L		Medium, y- and z-direction	204	42
M	I + Wide underbody		210	48
N	I + Wide underbody and side boxes		217	54
O	I + Mirrors	Medium, isotropic	204	42
P		Fine, isotropic	240	78

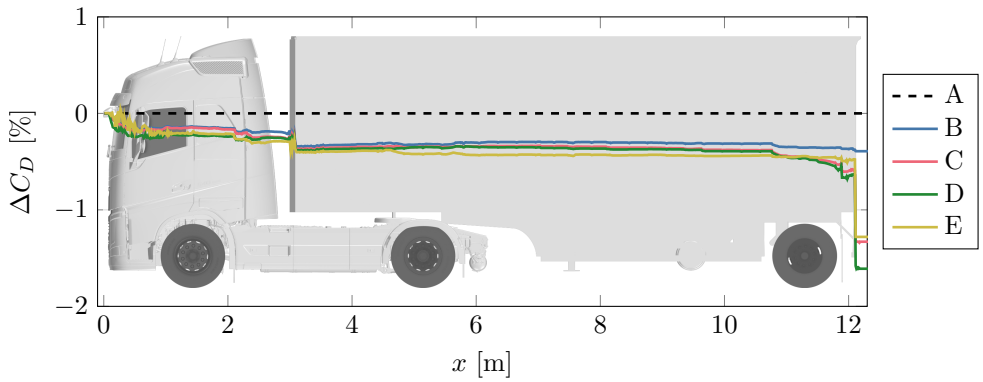

Figure A.5: Accumulated ΔC_D for cab box and refinements of cab radius and trailer wake shear layers compared to the baseline mesh A.

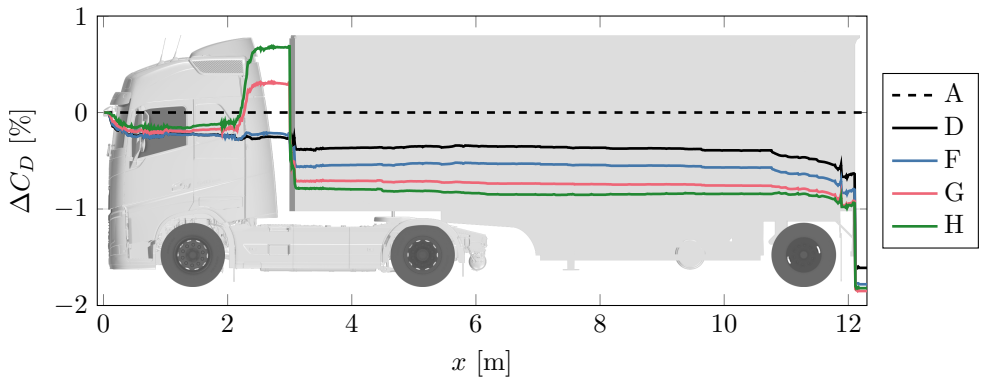

Figure A.6: Accumulated ΔC_D for refinements at trailer gap shear layers compared to the baseline A and configuration D.

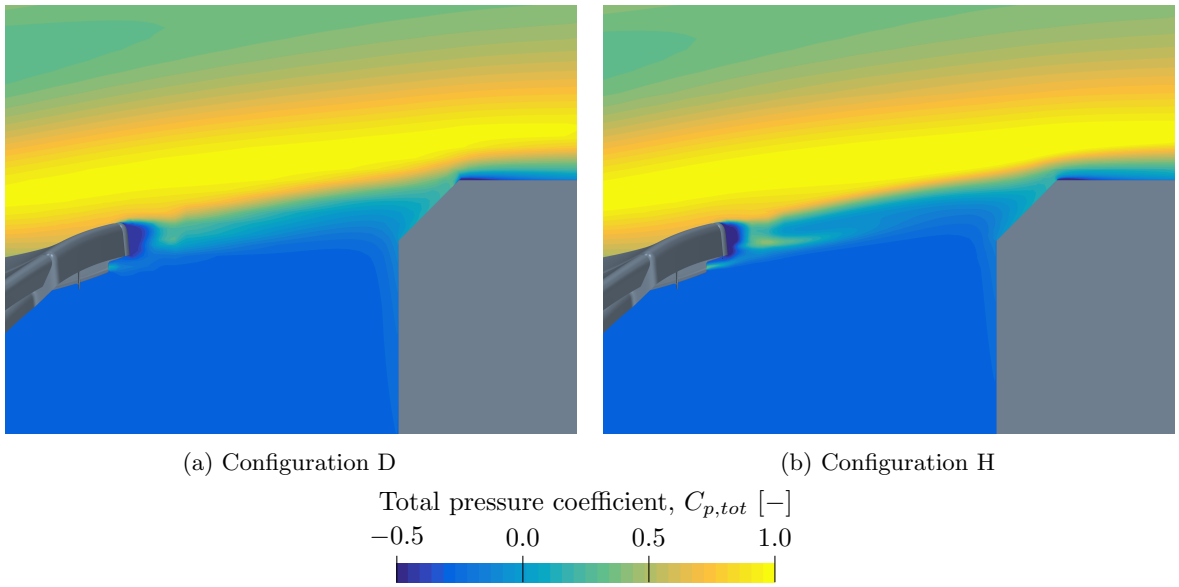

(a) Configuration D

(b) Configuration H

Figure A.7: Close-up image of the shear layer between the side deflector and trailer illustrated by the total pressure coefficient in a z-plane for two different meshes.

Trailer gap

To better resolve the large gradients in the shear layers at the side and roof deflectors refinements were added to configuration D according to figure A.4c. These used an anisotropic refinement in the main gradient direction, y on the sides and z on the top. Three different levels of refinement denoted F, G and H were investigated. In figure A.6 the accumulation of ΔC_D compared to the baseline mesh is shown. Additionally the ΔC_D for configuration D is shown. Comparing the ΔC_D it is noted that the refinement affects both the pressure in the gap as well as the overall energy loss over the gap. It is noted that the different configurations predict similar drag until the start of the roof deflector, where a finer refinement seem to correspond to more drag. In the trailer gap the predicted pressure decreases with increased level of refinement. Furthermore a finer mesh results in a larger overall energy loss over the gap. Comparing the total pressure fields of the different meshes it can be seen that the finer meshes results in a sharper interface between the high and low velocities. This is shown in figure A.7 where the total pressure of configuration D and H are compared. It can be seen that the sharper interface of the fine mesh reduces the amount of high-energy air hitting the trailer front, explaining parts of the lower losses in the trailer gap. Along the trailer no significant differences are noted between the meshes. However, at the trailer base a slight difference in base pressure results in all three levels of mesh refinements predicting the same overall drag. Considering both the results and the increase in cell counts it was decided to use the configuration G refinement in the upcoming meshes.

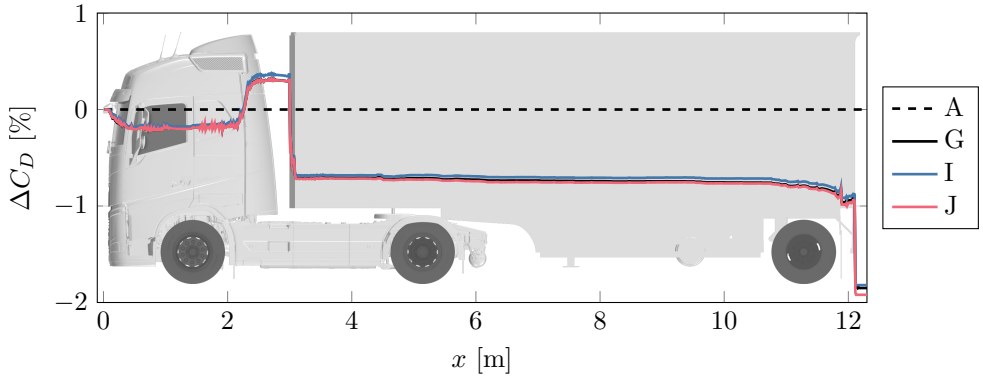

Figure A.8: Accumulated ΔC_D for trailer top refinement compared to the baseline A and configuration G.

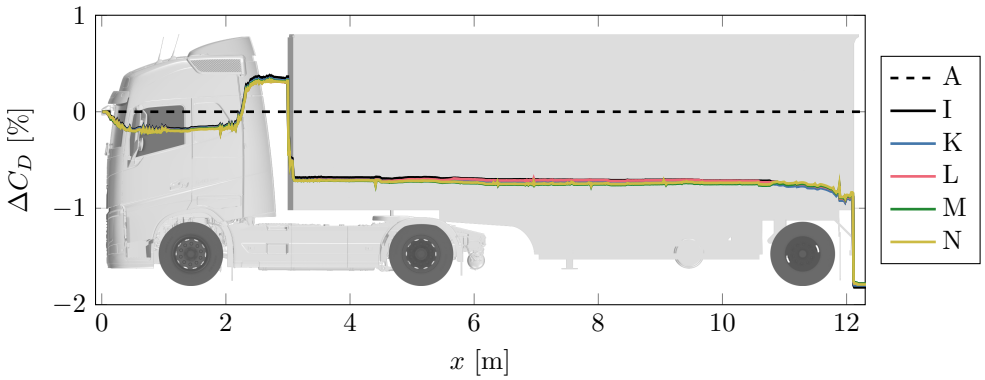

Figure A.9: Normalized accumulated ΔC_D for refinements at the underbody and the sides compared to the baseline and configuration I.

Trailer top

From the large values of $\hat{v}_x$ observed above the trailer in figure A.3 two different levels of refinement were investigated in a region according to figure A.4d. These were based upon the mesh of configuration G, used anisotropic refinements in the z-direction and denoted I and J. Although a decrease of $\hat{v}_x$ was noted no difference in the accumulated C_D was obtained. This is shown in figure A.4d where the accumulated ΔC_D of the two refinement levels are compared to configuration G. Despite no difference being observed configuration I was used for the following meshes, since it did not result in a significant number of additional cells.

Underbody and sides

There are multiple flow phenomena that could be better predicted by refining the underbody. These include the interface between the high-velocity air forced under the bumper spoiler and the low-velocity air inside the chassis, as well as the outwash from the wheels. Therefore a refinement was applied according to figure A.4e. This refinement was investigated for two different anisotropic refinement levels. First a refinement was applied only in the z-direction. Later the refinement was applied in both the y- and the z-direction. These were based on configuration I and denoted K and L. It was later found that the outwash from the wheels extended both further outwards and upwards than expected. Hence a wider underbody refinement was introduced, illustrated as the blue box in figure A.4f. Finally this larger box was combined with refinements all along the sides of the truck, designed to cover more of the outwash than from just the tires. These are illustrated as the red boxes in figure A.4f. Both meshes with the larger underbody refinement (with and without the side refinements) used an anisotropic refinement in both the y- and z-direction and are denoted M and N. In figure A.9 the accumulated ΔC_D compared to the baseline is shown for the four different configurations as well as for configuration I. No significant difference can be observed for any of the refinements. Hence the underbody and sides remained the same as in the baseline.

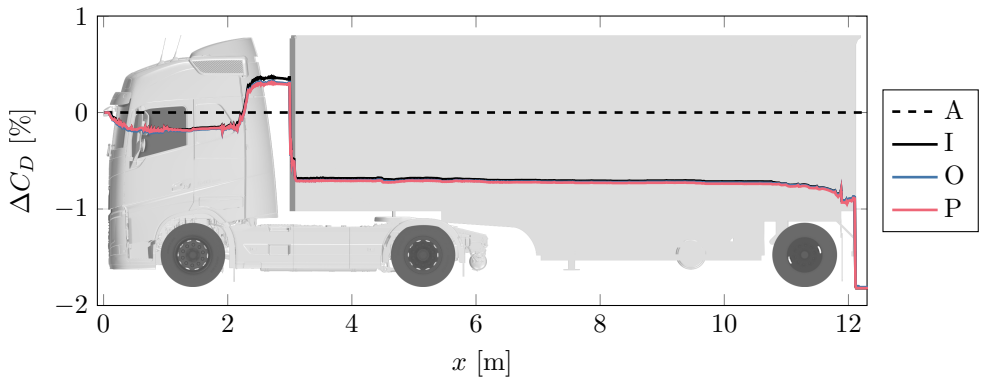

Figure A.10: Accumulated ΔC_D for refinements at the rear-view mirrors compared to the baseline A and configuration I.

Mirrors

Finally the region around the rear-view mirrors were refined according to figure A.4g. Two levels of isotropic refinements were investigated, medium and fine. It should be noted that the medium refinement does not alter the mesh directly around the mirror, since a large part of the mirror refinement box is located inside the cab box (figure A.4a), however it extends the wake refinement further downstream. Examining the accumulated ΔC_D in figure A.10 there is no significant difference between the two refinement levels. Compared to configuration I, without the extended mirror refinement, only a tiny difference can be seen in the trailer gap, where the mirror refinement leads to a slightly larger pressure being predicted. Despite no significant difference being noted after applying the mirror refinement it was decided to still use the medium refinement since the increase in cell count was small (approximately two millions) and the region is known to be critical for the overall aerodynamic performance of the truck.

A.2.3 Conclusions

Comparing the results of the baseline and the final mesh (configuration O) a 1.8% decrease of the drag was obtained. The most significant differences were caused by refinements in the shear layers of the trailer wake and the tractor-trailer gap. Furthermore it was found that the solution was less sensitive to refinements at the underbody, top and sides of the trailer as well as the mirrors. Figure A.11 shows the gradient magnitude per cell for the pressure coefficient and the x-velocity component for the final mesh. Compared to the baseline mesh (figure A.2 and A.3) a number of improvements can be noted. Firstly the cab box removed the large changes in both pressure and velocity in front of the tractor. Furthermore the changes per cell around the cab radius is reduced, which especially can be seen for the pressure. This improvement was obtained from the cab box and the front refinement ring and is believed to be important since the pressure gradient determines the separation around the cab radius. Furthermore the region of large gradients around the mirrors and trailer gap are significantly smaller. Similarly the trailer wake shear layers, both on top and at the sides of the trailer, are reduced.

Since the improved mesh resulted in a lower drag coefficient than the baseline mesh in this open road mesh study it could be believed that the new mesh would worsen the correlation when simulating using wind tunnel conditions. However, during the first parts of the mesh study, which were performed in the wind tunnel environment, similar refinements to those in this study, such as the trailer wake shear layer refinements, generally resulted in more drag. However many of those simulations proved difficult to converge, leading to the mesh study instead being performed in open road conditions. Furthermore the initial steps of the mesh study showed that different areas are sensitive to refinements in the wind tunnel than in open road. As an example the stationary ground and non-rotating wheels in the wind tunnel showed a large sensitivity to underbody refinements, altering the flow in the trailer wake, whereas in open road little mesh sensitivity was observed in these areas. Hence it might be necessary to use a significantly different mesh strategy in the wind tunnel than in open road. For the studies in this thesis some care was put into altering the mesh for the wind tunnel, mostly in terms of resolving the flow at the walls, especially the floor. However more effort might be needed to account for other wind tunnel effects such as blockage.

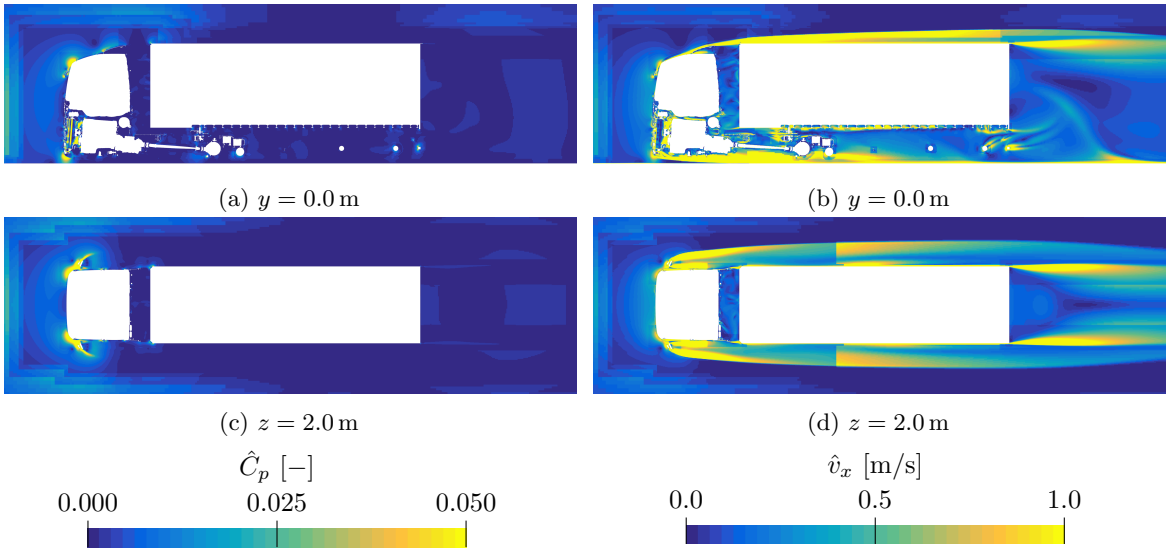

(a) $y = 0.0\,\mathrm{m}$ (b) $y = 0.0\,\mathrm{m}$

(c) $z = 2.0\,\mathrm{m}$ (d) $z = 2.0\,\mathrm{m}$

Figure A.11: Magnitude of C_p and v_x gradient per cell for final mesh.